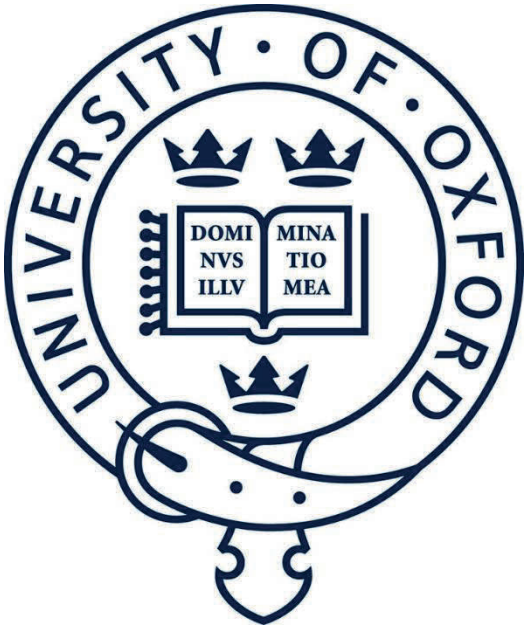
ESTABLISHMENT OF AN EX VIVO PRECISION-CUT LUNG SLICE MODEL FOR THE EVALUATION OF DRUG-RADIATION RESPONSES



Department of Oncology
University of Oxford

Maryam Alkadhimi
St. Catherine's College, University of Oxford

Thesis submitted for the degree of Doctor of Philosophy in Oncology
Michaelmas Term, 2021

Abstract

Background: We hypothesised that the ex vivo precision-cut lung slices could provide a novel model for studying the biological responses of normal tissue to ionizing radiation and additionally provide important mechanistic insights into drug-radiation combinations.

Aims: 1) To establish an ex vivo model of lung tissue slices from mice. 2) To evaluate DNA damage responses in ex vivo lung slices compared with in vivo responses in lungs. 3) To determine the impact of NU7441, a pharmacological inhibitor of DNA-PK, on the DNA damage response.

Methods: Left lungs from female C57BL/6 mice (6-12 weeks old) were dissected and perfused with 4% low gelling temperature agarose. Lungs were sliced (250 μm) and incubated ex vivo for up to seven days. Lung slices were irradiated (^{137}Cs) in the presence or absence of a DNA-PK inhibitor (NU7441). Fixed tissue sections were stained for histological markers (γH2AX and 53BP1) of DNA double-strand breaks (DSBs).

Results: We established culture conditions that maintained tissue viability for up to 7 days and structural integrity for at least 3 days. We showed that DNA damage responses to ionizing radiation were similar in ex vivo lung slices and lungs irradiated in vivo. Treatment with NU7441 was associated with an increase in long-lived DNA DSBs consistent with pharmacological inhibition of DNA repair. Unexpectedly, we found that a subset of lung epithelial cells (alveolar Type II) had low levels of γH2AX and 53BP1 staining following irradiation, which may have been associated with rapid repair of DNA DSBs.

Conclusion: The DNA damage response to ionizing radiation in lung tissue is similar in ex vivo and in vivo. The ex vivo lung slice model is a novel and highly tractable experimental system for studying the biological effects of drug-radiation combinations where the ability to carefully control experimental variables gives it clear advantages over in vivo models.

Acknowledgments

I am eternally thankful to God for all His blessings over the last four years, for assisting me and bringing the most wonderful people into my life.

Firstly, I'd like to express my most profound appreciation to my supervisor, Dr. Anderson Ryan, for all of his support throughout this project (the number of meetings we had and the number of times I came to you with questions and you answered them without complaint) as well as life lessons, of which I particularly enjoyed the method for breaking habits using a rubber band.

Secondly, I like to express my gratitude to my college, and in particular to Ashok Handa, Cressida Chappell, Richard Molyneux, and Gurman Kaur, for their guidance in dealing with tough circumstances and taking appropriate actions when necessary.

I would also like to thank Katherine Vallis and Gunnar Tobin for their support during my Master's as an Erasmus exchange student and when applying for the DPhil, and for giving me that opportunity.

I cannot express my gratitude enough to my friends who directly influenced my project: Helen Manne, for being a lovely friend throughout, and I specifically enjoyed how things kept going wrong, and for helping me write my thesis and papers (especially for the late-night meetings after work); Marcus Green, for all the project discussions, IHC method, and career advice. Yanyan Jiang for always providing me with lungs on time. Kay Shigemori for dragging me out to events and helping me prepare for presentations. I know you all had a lot to do.

I'd want to express my gratitude to departmental personnel in specific Rhodri Wilson, Mark Hill, James Thompson, John Biggerstaff, and Mick Woodcock, who assisted me in learning new techniques and were always available to assist with any technical issues that arose.

I'd also want to express my gratitude to the Andy Ryan group in particular Letitia Harris, Callum Beach, Steve Stribbling and Luiza Lourenco.

I'd like to thank the MRC for funding me throughout the four years. And I would like to thank all my evaluators and examiners, namely: Maria Hawkins, Kerry Fischer, Valantine Macaulay, Katherine Vallis, and Charlotte Dean.

I'd like to thank my Oxford friends, Sahar Tehrani, Hira Javid, Fatemeh Paarsi, Nadia Amin and Anam Iqbal for making living alone in Oxford a pleasant experience. I really enjoyed our excursions and strange discussions, particularly the one about the STAR!

I cannot begin to convey my heartfelt gratitude to my family for their unconditional love, unwavering mental and financial support and pride for this stage of my life. My father Thamir Alkadhimi for assisting me with settling here and traveling back and forth every two weeks at first, and my mother Nadya Esfahani for the lengthy conversations, especially late at night when I was anxious. My brother Hussain Alkadhimi for the IT and spiritual support as well as helping my mum out when dad was not there and for all the vegan chocolates you got me, and my sister Esra Alkadhimi for believing in me and encouraging me to apply for a DPhil at Oxford and living with me throughout the summers. Likewise, my uncle Adnan Alkadhimi for all his support, advices and lengthy talks and discussions. All of you made this challenging experience easy and enjoyable and I consider myself very fortunate to have you all in my life.

Contents

Abstract 2
Acknowledgments 3
List of Tables 8
List of Abbreviation 9
1 Introduction 10
2 Background 13
2.1 Ionising Radiation (IR) 13
2.1.1 Ionising radiation side effects 14
2.1.2 Prevention of radiation induced side effects 17
2.2 Cellular Responses to Radiation Induced DNA Damage 18
2.2.1 Non-homologous End joining 20
2.3 The Respiratory System 22
2.3.1 The Human respiratory system 23
2.3.2 The Human Lung 23
2.3.3 The Mouse Respiratory system 24
2.3.4 The Mouse Lung in Comparison to the Human Lung 25
2.3.5 Lung Stem Cells and Their functions 28
2.3.6 The Pulmonary Immune System 35
2.4 Models to Study Radiation-Induced Lung Toxicity 38
2.4.1 In Vivo Models 40
2.4.2 In vitro Cell Culture Models 43
2.4.3 3D Cell Culture 44
2.5 Ex Vivo Precision-Cut Tissue Slices 49
2.5.1 History of Ex vivo Tissue Slice Method 49
3 Research Objectives 53
4 Methodology 55
4.1 C57BL/6 Lung Dissection 55
4.2 Vibratome Slicing 55
4.3 Culture Conditions 56
4.3.1 Preparation of the incubating 6-well plates 56
4.3.2 Culturing 56
4.4 Sytox Green Assay 56
4.5 Ionising Radiation 57

4.6 Fixing, Processing and Embedding 57
4.7 In vivo Experiments 58
4.7.1 Sampling left lung, fixing and processing 58
4.8 Preparation of the slides 59
4.9 Immunohistochemistry (IHC) 59
4.10 Analysis of IHC 59
4.11 Haematoxylin and Eosin Staining 60
4.12 Double Staining Immunofluorescence (IF) 60
4.13 Detection of dual stain (IF) 61
4.14 Analysis of IF 61
4.15 Statistics 61
5 Results 64
5.1 Establishment of the Ex Vivo Precision-Cut Lung Slice (PCLS) Model 64
5.1.1 Introduction 64
5.1.2 Tissue sectioning with a vibratome (Leica VT1200S) 67
5.1.3 In vitro culture: Filter choice 67
5.1.4 In vitro culture: Media 68
5.1.5 Structural integrity and cellularity throughout the seven days of the ex vivo precision-cut mouse lung slice model 70
5.1.6 Immunofluorescence (IF) visualisation of DDR foci 70
5.1.7 Discussion 71
5.2 Evaluation of DNA Damage Response in Ex Vivo Precision-Cut Lung Slice Model Following Radiation 78
5.2.1 Introduction 78
5.2.2 Categorising γH2AX expression levels following 10 Gy irradiation 79
5.2.3 DNA Damage response in vivo and ex vivo at different doses of radiation 82
5.2.4 Discussion 88
5.3 The Impact Of NU7441 On The Radiation-Induced DNA Damage Response In The Ex Vivo Precision-Cut Lung Slice Model 91
5.3.1 Introduction 91
5.3.2 DDR Responses In Ex Vivo Lung Tissue Slices Following Treatment With NU7441 And Radiation 94
5.3.1 Cleaved Caspase 3 99
5.3.2 Radiation induced DNA damage response in SCID mice 101
5.3.3 Discussion 104

5.4 Alveolar Type II cells 107
5.4.1 Introduction 107
5.4.2 Evaluation Of AT2 Cells In The Ex Vivo Tissue Slice Model 108
5.4.3 DDR in AT2 Cells in Precision-Cut Lung Slices 110
5.4.4 Discussion 113
6 General Discussion 115
7 Reference 122
8 Appendix 138
8.1 Supplementary Data 138
8.2 Raw Statistical Data 146

Final word count: approximately 34 500

List of Figures

Figure 2.1. Major DNA Damage Types Caused by IR and Their Repair Mechanisms
Figure 2.2. Time course of side effects of thoracic radiation
Figure 2.3. Schematic cell-cycle showing HR and NHEJ repair pathways
Figure 2.4. Schematic of Steps in Non-Homologous End Joining
Figure 2.5. General over-view of the lung, indicating the major cell types
Figure 2.6. Mouse and human lung composition
Figure 2.7. AT2 cells regulation during lung repair
Figure 2.8. Showing how club cells differentiate
Figure 2.9. Schematic Timeline for Key Seps in the Development of Ex Vivo Lung Tissue Slice Models
Figure 2.10. Ex Vivo Tissue Slices as a Bridge between In Vitro and In Vivo Models
Figure 5.1. An illustration of the PCLS model.
Figure 5.3. The cellular integrity of the lung tissue slices incubated in PBS and DMEM/F12 plus 5% FBS.
Figure 5.4. H&E staining of lung tissue slices cultured for 7 days.
Figure 5.5. DNA damage response (DDR) following irradiation in different medium conditions.
Figure 5.6. Culturing PCLS in DMEM F12 plus .0.5% or 5% FBS.
Figure 5.7. Evaluation of cell death in PCLS under different culture conditions.
Figure 5.8. Evaluation of precision-cut lung slices structure and cellular integrity in culture throughout 7 days.
Figure 5.9. Dual staining protocol for DDR using immunofluorescence.
Figure 5.10. Categories of γH2AX staining following in vivo or ex vivo irradiation of lung tissue.
Figure 5.11. Evaluation of γH2AX levels in PCLS: The effect of dose and time.
Figure 5.12. Evaluation of 53BP1 levels in PCLS: The effect of dose and time
Figure 5.13. Schematic illustration of DSB repair.
Figure 5.14. Structure of the DNA-PK inhibitors LY294002 and NU7441.
Figure 5.15. γH2AX IHC staining in ex vivo PCLS ex vivo precision-cut lung slices following treatment with NU7441 and ionising radiation.
Figure 5.16. 53BP1 IHC staining in ex vivo PCLS ex vivo precision-cut lung slices following treatment with NU7441 and ionising radiation.
Figure 5.17. Cleaved Caspase 3 (CC3) staining to check for toxicity of the NU7441 on PCLS
Figure 5.18. IHC staining in irradiated (10 Gy) ex vivo lung slices from SCID mice.
Figure 5.19. SPC expression in ex vivo precision-cut lung slices treated with (10 Gy) or without (0 Gy) irradiation.
Figure 5.20. γH2AX staining by IF in SPC+ cells following irradiation (10 Gy).
Figure 5.21. γH2AX staining by IF in SPC+ cells following irradiation (10 Gy) of ex vivo lung slices from SCID mice.

List of Tables

Table 2.1. Comparison of Human and Mouse Lung Anatomy
Table 2.2. Comparison of experimental models for studying effects on lung cells/tissue
Table 3.1. Reagents List
Table 3.2. Primary Antibodies
Table 3.3. Secondary Antibodies
Table 3.4. Mice
Table 5.1. A summary of the sectioning and culture conditions investigated for mouse PCLS.
Table 5.2. Proposed categories of γH2AX staining in lung tissue

List of Abbreviation

53BP1	Tumour protein p53 binding protein 1
AT1	Alveolar Type I Cells
AT2	Alveolar Type II Cells
ATM	Ataxia-telangiectasia mutated
ATR	Ataxia- telangiectasia and Rad3-related
BER	Base excision repair
DAB	3,3´-Diaminobenzidine
DDR	DNA Damage Response
DDRi	DNA Damage Response Inhibitors
DMSO	Dimethylsulfoxide
DNA	Deoxyribonucleic acid
DNA-PK	DNA- dependent protein kinase
DNAPKcs	DNA- dependent protein kinase catalytic subunit
DNA-PKi	DNA-dependent protein kinase inhibitor
DSB	Double strand break
ECM	Extracellular matrix
Gy	Gray
H&E	Haematoxylin and Eosin staining
H2AX	H2A histone family member X
IF	Immunofluorescence
IHC	Immunohistochemistry
IR	Ionising Radiation
NER	Nucleotide excision repair
NMR	Protein complex including Mre11, Rad50, Nbs1
PBS	Phosphate-buffered saline
PCLS	Precision-cut lung slices
PTFE	Polytetrafluorethylene
SPC	Surfactant protein C
γH2AX	Gamma histone 2AX

1 Introduction

More than half of cancer patients receive radiation during the course of their treatment (R. A. Sharma et al. 2016). Radiation is an effective anti-cancer therapy, but the dose that can be delivered to tumours is limited by normal tissue toxicity (R. A. Sharma et al. 2016). Therefore, the concept of a 'therapeutic window' – treatment that produces anti-tumour responses without intolerable adverse effects – is a key concept in radiotherapy and radiobiology (R. A. Sharma et al. 2016).

Current research is focusing on improving the therapeutic window of radiation by three distinct approaches:

1. More accurate delivery of radiation to the tumour
2. Increased selectivity of radiation effects in tumours
3. Ameliorating the normal tissue effects of radiation

Preclinical studies can be used to investigate the impact of radiation on normal tissues and non-tumour cells. Although in vitro studies can be useful, in particular for mechanistic studies, there are significant limitations. For example, many tissues have only a small population of proliferating cells (e.g., the lung, blood vessels), and not all primary cells can be effectively cultured/maintained in vitro for long-term studies. In addition, the communications between different cell types and the three-dimensional characteristics of the multiple cell types found in an organ are difficult to recapitulate in vitro.

In vivo preclinical models (e.g. mouse models) have normal tissue characteristics and physiology and are therefore better models of normal tissue responses to drugs and radiation than in vitro models. Nonetheless, these models have significant limitations. For radiation, it is challenging to deliver an accurate dose to tissues due to differences in organ motion and position. Imaging can in part overcome some of these limitations, but this is often time

consuming and complex. For drug treatments, differences in drug absorption, distribution, metabolism and excretion mean that it can be difficult to accurately assess the amount of drug present in a tissue over time in a particular animal. Therefore, although studying drug-radiation effects in vivo is an attractive approach most likely to best mimic the clinical situation, the lack of accurate control of experimental variables such a tissue drug levels suggest that other methods may be useful to explore, in particular as they may reduce the number of experimental animals studied.

Ex vivo models are a potential experimental approach that bridge in vitro and in vivo models. There are several cellular ex vivo models that have been developed including multicellular spheroids and organoids. Although experiments are performed in vitro, and the cells differentiate and communicate, they do not in general have the three dimensional characteristics of an organ (Hickman et al. 2014). In the present work, we investigated ex vivo precision-cut lung tissue slices, as the cells remain in the organ context that was present in the mouse.

Cultured tissue slices have been used for brain research for decades, and this is now a well-established technique (Cho, Wood, and Bowlby 2007), which has recently been exploited to study tumour sections (Davies et al. 2015).

Normal lung tissue is affected by radiotherapy during treatment of, for example, breast, lung and esophageal cancer. Acute and late toxicity can be dose-limiting side effects of lung irradiation, although the biological mechanisms are not fully understood. In this project we aimed to investigate lung tissue slices as a novel approach for studying the biological effects of radiation in the lung. The ex vivo lung slice model has been used to examine lung biology and respiratory diseases such as asthma and chronic obstructive pulmonary disease (COPD) (G. Liu et al. 2019). Moreover, recently Akram et al. established a lung slice model to study

alveologenesis to understand bronchopulmonary dysplasia (Akram et al. 2019). However, the tissue slice model has not been utilised to study the effects of radiation on the lung. Therefore, we established a methodology for this technique in our laboratory and assessed its suitability as a surrogate for in vivo radiation and drug investigations.

2 Background

2.1 Ionising Radiation (IR)

The effectiveness of ionizing radiation in cancer treatment is due primarily to the cell death it causes as a result of DNA damage. The effects of radiation on the DNA can be direct or indirect. The direct damage can result when photons interact with DNA and cause base/nucleotide damage or strand breaks. Indirect damage occurs when photons interact with other components in the cells such as water, proteins or lipids to generate reactive oxygen species (ROS), which may interact with, and damage DNA (Santivasi and Xia 2014)(Willers, Dahm-Daphi, and Powell 2004)(Lourenco 2017).

Radiation causes different types of DNA damage: base damage (3000/Gy/cell); single strand breaks (SSBs) (1000/Gy/cell); DNA-protein and DNA-DNA cross links (150 and 20/Gy/cell); and double strand breaks (DSBs) (40/Gy/cell) which are considered the primary lesion and may result in loss of large chromosomal regions and in turn structural mutations in the DNA (Chalmers and Carruthers 2021). It is important to note that the capacity of IR to cause cell death is not limited to cancer cells, as it will also generate damage to irradiated normal tissues. Nonetheless, the impact of the DNA damage in cancer cells may be more significant due to aberrant DNA damage response and repair pathways. (Bentzen 2006)

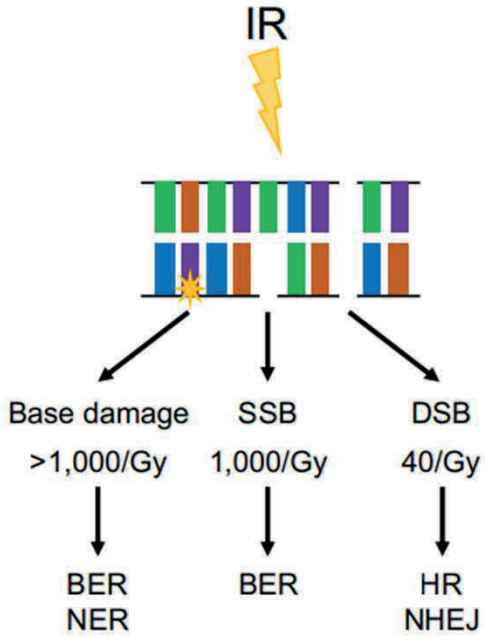


Figure 2.1. Major DNA Damage Types Caused by IR and Their Repair Mechanisms. IR causes 3 types of DNA damage, namely: base damage, single-stranded breaks (SSB), and double-stranded breaks (DSB). The cells repair them by distinct mechanisms, Base excision repair (BER) and nucleotide excision repair (NER) for base damage and SSB, and homologous recombination (HR) or non-homologous end-joining (NHEJ) for DSBs. (Hall and Giaccia 2019)

2.1.1 Ionising radiation side effects

Clinical radiotherapy-related side effects are generally classified as early (occurring within days or weeks after treatment) or late (occurring months or years later) (Bentzen 2006)(Lourenco 2017). Normal tissues contain replicative stem cells are vital for replacing lost cells and restoring tissue architecture and function within damaged tissues (Prise and Saran 2011)(Lourenco 2017). It is thought that radiation kills stem cells by causing DNA double-strand breaks that remain unrepaired, leading to cell death, thereby constraining subsequent normal tissue regeneration following radiation damage. In rapidly proliferating tissues with high cell turnover, such as the small intestine, loss of stem cell function is apparent within days/weeks and is associated with early toxicity. For tissues with a low cell turnover, stem cell

damage can take months or years to become apparent, and these tissues are associated with late toxicity (Hall and Giaccia 2019). In addition to stem cell damage in tissues, damage to other cells can cause an inflammatory response, for example, pneumonitis in the lung, which can become apparent days/weeks after radiotherapy. (Lourenco 2017)

Early side-effects linked with thoracic irradiation (e.g., when treating esophageal, lung or, breast cancer) include dermatitis and esophagitis, which have a high incidence but are reversible and treatable. Preventative measures include careful radiotherapy planning to limit normal tissue exposure to radiation. Palliative treatments for skin and esophageal toxicity include topical creams, analgesics, and dietary support. (Baker and Fairchild 2016)(Bolderston et al. 2006)(Werner-Wasik et al. 2010)(Lourenco 2017)

Alternatively, later side-effects of thoracic radiation are more complicated and include pneumonitis, pulmonary fibrosis, and cardiac toxicity. Three months following radiotherapy, patients may develop pneumonitis (lung inflammation), which can be clinically treated with corticosteroids. Pneumonitis can be asymptomatic though the incidence of symptomatic pneumonitis for patients receiving radiation is between 5-15% (Sekine et al. 2006)(Lourenco 2017). On the other hand, pulmonary fibrosis which results from extracellular matrix (ECM) build-up in the lungs, is considered an irreversible, untreatable side effect that can arise 6 months to several years following radiotherapy. The incidence of pulmonary fibrosis is between 10-15% of patients receiving radiation. (Sekine et al. 2006)(Carver et al. 2007)(Lourenco 2017)

Not all patients who receive radiation develop normal tissue complications, but several factors contribute, including absorbed dose to the organ, the volume of tissue being irradiated, and dose fractionation.

Another potential contributor to the development of radiation-induced complications is genetic polymorphisms. This concept has been strengthened by investigations using different mouse strains (BALB/c, C57BL/6, and SCID). In contrast to SCID mice with no DNAPKcs activity, BALB/c mice have two naturally occurring single nucleotide polymorphisms in the coding region of DNAPKcs (an essential protein in DSB repair (see section 2.3.1.), whereas C57BL/6 mice express wild-type protein. When these mice were irradiated, and the DNA repair was analyzed at different time points, it was shown that C57BL/6 mice recovered the damage within 24 h with very little residual DNA damage. On the other hand, the SCID mice had significant levels of unrepaired DNA damage, while the BALB/c mice had intermediate levels of unrepaired DNA damage. This was subsequently linked to the notion that similar to mice; people may have genetic polymorphisms, which could lead to varying tolerance to radiation that, may influence the development of radiation-induced side effects. (Rübe et al. 2008)

Multiple studies have tried to identify the major processes underlying radiation-induced lung toxicity; however, the fundamental mechanisms remain unknown (Lourenco 2017)(Graves et al. 2010)(Kainthola et al. 2017)(Tsoutsou and Koukourakis 2006). A standard view is that initial tissue damage triggers an acute activation of the immune cells which can lead to a persistent inflammation (pneumonitis) ending in excessive deposition of the ECM and reduced pulmonary function (irreversible fibrosis)(Lourenco 2017). Many molecular contributors, particularly cytokines, have been identified and investigated as accountable for systemic and local effects of thoracic irradiation (Rubin et al. 1995)(Lourenco 2017). Notably, the process involves a variety of cell types, including alveolar cells, bronchioepithelial cells, stromal cells, endothelial cells, and immune cells. (Almeida et al. 2013)(Andersson-Sjöland, Karlsson, and Rydell-Törmänen 2016) (Lourenco 2017)

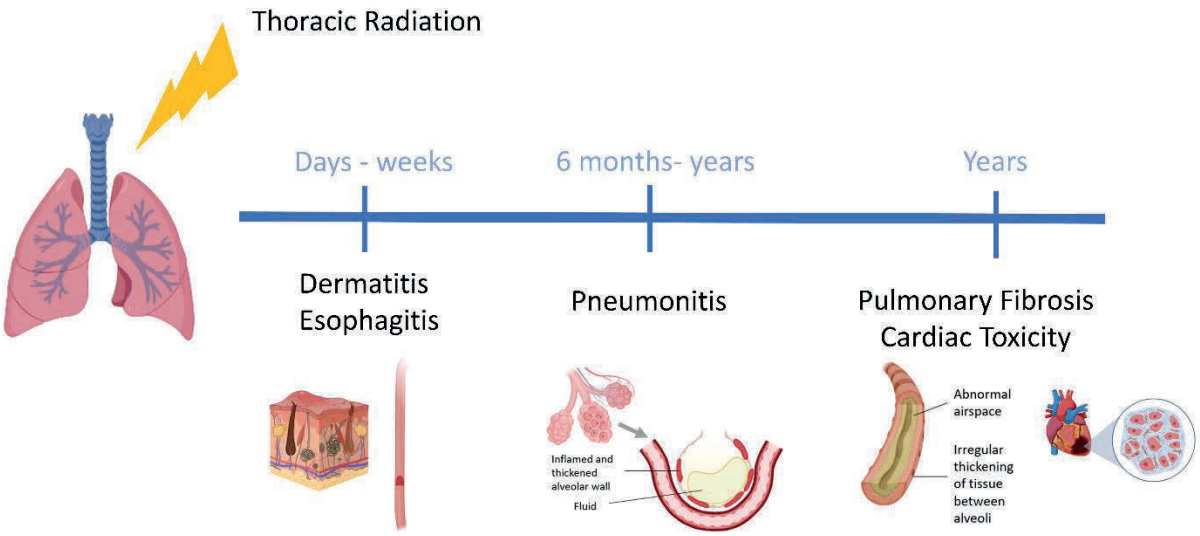


Figure 2.2. Time course of side effects of thoracic radiation. Dermatitis and esophagitis may develop days to weeks after irradiation. Pneumonitis may develop 6 months to a year later, followed by lung fibrosis and heart damage. [Created with BioRender.com]

2.1.2 Prevention of radiation induced side effects

The incidence and severity of radiation-induced side effects have been reduced in recent years as more advanced radiation planning methods, fractionation schemes, and better dose control have been developed (Lourenco 2017). For example, in the treatment of lung cancer, the adoption of methods such as intensity-modulated radiation (IMRT) has demonstrated a reduction in the dose delivered to normal tissues (Christodoulou 2014)(Lourenco 2017). Additionally, the development of image-guided irradiation techniques has increased dose delivery to the tumour. Another strategy for reducing normal tissue toxicity is to employ fractionated radiation regimens. Apart from preserving normal tissue, it has been suggested that fractionation may enhance tumor cell death, and reduce normal tissue toxicity through the application of the ´5Rs´of radiation therapy (repair, repopulation, reoxygenation, radio-

sensitivity and cell cycle redistribution) (Lourenco 2017). As a result, the use of fractionated radiation regimens may improve the therapeutic index. However, normal tissue damage continues to be a concern in the clinic, mainly when treating centrally located tumors, where avoiding critical normal tissues is more complex. (Lourenco 2017)(Good and Harrington 2013)

In order to minimize the risk of radiation toxicities, current non-small lung cancer therapy recommendations include dosage constraints and limiting the volume of the irradiated organ. For instance, in standard fractionation regimens, the total treated volume of the lung receiving a dose of greater than 20 Gy (V20Gy) is less than 35% (Fleming et al. 2016). In addition, a thoracic organ at risk plan has been constructed to denote the organ at risk following irradiation to ensure consistency between clinicians and treatment regimens. (Fleming et al. 2016)(Kong, Ritter, and Quint 2010)(J. Martin 2020)

2.2 Cellular Responses to Radiation Induced DNA Damage

Cells respond to radiation-induced DNA damage by activating signaling pathways that result in DNA repair, cell senescence, or cell death (Noda 2018). The choice of DNA repair pathway depends primarily on the cell cycle phase and nature of the damage, namely: base and nucleotide damage – is repaired by base excision repair (BER) and nucleotide excision repair (NER), single-strand breaks (SSBs)- predominantly by BER and double-strand breaks (DSBs) - either homologous recombination (HR) or non-homologous end-joining (NHEJ). BER, NER, and HR utilize the undamaged template strand (BER, NER) or the sister chromatid to guide DNA repair and therefore restore the genetic material and are considered error-free pathways. (Chalmers and Carruthers 2021)(Santivasi and Xia 2014)(Lourenco 2017)

For DSBs, error-free HR only operates during the S and G2 phases of the cell cycle, when a sister chromatid has been produced following DNA replication. Nonetheless, the predominant repair pathway of DNA DSBs is NHEJ, an error-prone pathway utilized by cells in all cell cycle phases, at which point the broken DNA strands are re-ligated quickly at the expense of losing genetic materials and subsequent mutation. Non-proliferating cells in tissues such as the lung rely on NHEJ for DNA DSB repair as very few of the cells are proliferating; therefore, the cells are in G1 phase (or G0, resting phase) without a sister chromatid template. (Lourenco 2017)

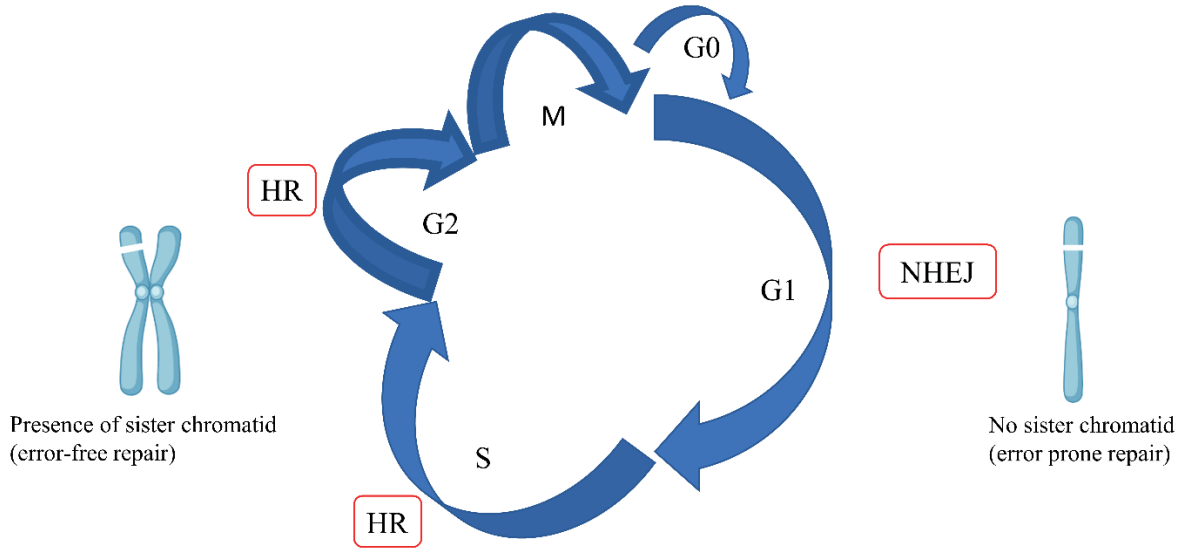


Figure 2.3. Schematic cell-cycle showing HR and NHEJ repair pathways. The HR DNA DSB repair pathway can only be used when a sister chromatid is available i.e. in S or G2 phases of the cell cycle. In contrast, DNA DSB by NHEJ does not require a sister chromatid and can be used in all phases of the cell cycle.

Crucially, non-proliferating cells, which make up the majority of cells in tissues such as the lung, are in the G1 (or G0) phase of the cell cycle and NHEJ is the only DNA DSB repair pathway available.

2.2.1 Non-homologous End joining

NHEJ's overall mechanism may be broken down into 4 segments, namely:

1) DNA end detection and assembly of a DNA damage repair complex of proteins on the double-strand breaks
2) Joining of the DNA ends
3) Processing of DNA ends
4) Ligation of the broken ends and the dissociation of the proteins.

The cell's initial response to DNA double-strand breaks activates DNA damage sensors, including ATM and ATR, that promote DNA repair and prevent the cell from progressing through the cell cycle until the break is successfully repaired. ATM and ATR belong to a family of phosphatidylinositol-3-kinase-related kinases (PIKK) and are activated in the presence of double-strand breaks (DSBs). A KU70/KU80 heterodimer attaches at the ends of a DNA double-strand break, followed by recruitment of DNAPKcs and repair of the DNA DSB (Figure 2.3). In S and G2 phase cells, the selection between HR and NHEJ repair pathways is partially regulated by the 53BP1 protein. DNA DSBs can be recognized by MRN complexes (MRE11/RAD50/NBS1), leading to activation of ATM, phosphorylation of histone H2AX, recruitment of 53BP1, and subsequent inhibition of the HR DNA repair pathway, (see section 4.3 for more details). (A. J. Davis and Chen 2013) (Hall and Giaccia 2019)

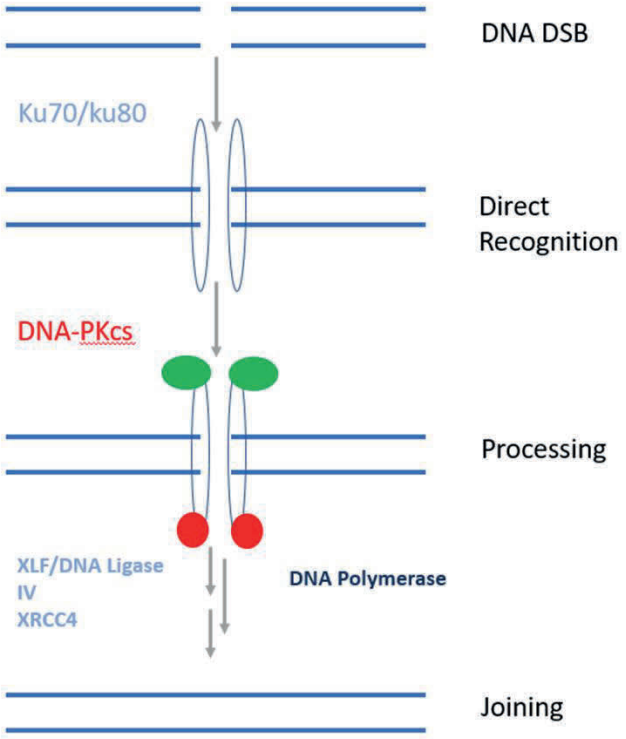


Figure 2.4. Schematic of Non-Homologous End Joining mechanism. DNA DSBs are sensed by Ku70/Ku80 which recruits DNA-PKcs which in turn recruits DNA polymerase and other DNA ligase factors to join the two DNA strands together.

2.3 The Respiratory System

Irradiation of the thorax may cause life-threatening complications such as pneumonitis and fibrosis. This makes the lungs a critical dose-limiting organ for radiotherapy treatments. This section examines the basic anatomy and histology of human and mouse lungs to highlight similarities and differences that might need to be taken into account when considering mouse models of human disease.

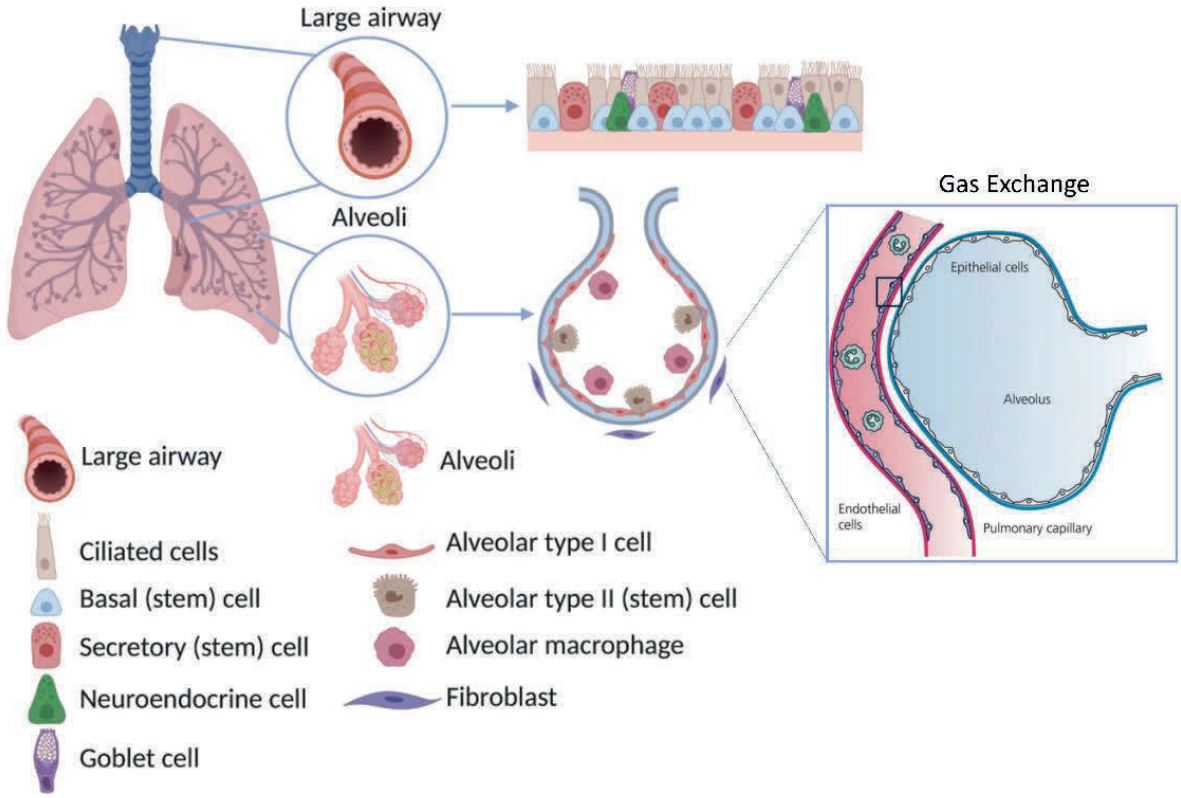


Figure 2.5. General overview of the lung, indicating the major cell types. The large airways are composed of ciliated, goblet and neuroendocrine cells, in addition to basal and secretory stem cells (EuroStemCell 2022)(Simmons et al. 2019).

2.3.1 The Human respiratory system

The respiratory system is made up of the nose, pharynx, larynx, trachea, right and left main bronchi and the lungs. Structurally, the respiratory system is comprises of the upper respiratory system (including the nose, nasal cavity, and pharynx) and the lower respiratory system. (which comprises of the larynx, trachea, bronchi and the lungs) (Marieb 1992)

The respiratory system can also be split functionally into two distinct zones: the conducting and the respiratory. The conducting zone is composed of a network of internal and external crossing tubes and cavities to the lungs, where the air is filtered, warmed, and moistened as it travels through the airways. The respiratory zone in turn, is made up of the tissues within the lungs where the air-blood gas exchange occurs, incorporating the bronchioles, alveolar duct, alveolar sacs and alveoli. (Marieb 1992)

2.3.2 The Human Lung

The lungs are broadly pyramid-shaped organs whose volume consists mainly of air. The apex of the lungs occupies the superior region, and the coastal region aligns with the ribs. Inferior to the lungs is the diaphragm, which is a dome-shaped muscle that contracts rhythmically, continually, and (primarily) involuntarily to aid breathing. (Marieb 1992)

The left and right lungs are separated by the heart and the mediastinum, and are linked to the trachea via the left and right main bronchi. The major difference between the left and right lung is size and shape. The left lung is 10% smaller than the right lung due to the presence of the cardiac notch, which is an indentation in the left lung where the heart apex lies. The right lung is broader and shorter than the left, and the diaphragm is higher on the right side. Notably, the left lung is made up of two pulmonary lobes: superior and inferior, while the right lung consists of three lobes: superior, middle, and inferior. These pulmonary lobes are sections formed as the bronchi branches into bronchioles; each lobe has one large bronchiole subdivides into

multiple smaller bronchioles. The interlobular septa, of connective tissues, separate the lobes. (Marieb 1992)

Both lungs are sealed and protected by pleura delicate serous membranes comprising the parietal pleura (the wall lining the thoracic cavity) and visceral pleura (the deeper membrane covering the lungs). Between the two pleura, is the pleural cavity which contains a lubricating fluid known as pleural fluid, allowing the parietal and visceral pleura to glide smoothly during breathing. (Marieb 1992)

2.3.3 The Mouse Respiratory system

The mouse has been widely utilized as a model for respiratory study (Irvin and Bates 2003). Mouse models enable researchers to investigate different lung diseases at a level of detail that is very difficult in human subjects. For example, with the development and understanding of human and mouse genomes, and the emergence of genetic engineering, it is possible to identify disease-specific genes in the mouse model and identify the equivalent gene in a human. In comparison to the human lungs, the total lung capacity (TLC) of mouse lungs is around 1 mL and around 3-4% of their body weight, whereas in humans, lung volume is around 6000 mL and about 8-10% of body weight, and the mouse has faster respiratory rates. (Irvin and Bates 2003)

Similar to the human respiratory system, the mouse respiratory tract can be described in two ways: function and structure. First, the mouse respiratory system is structurally split into three modules depending on the presence or absence of support structures for the airway conduits. The anterior component, which includes the nostrils, nasal cavities, and nasopharynx, is predominantly cartilage, bone, or a combination of the two. The intermediate segment is supported primarily with cartilage and includes the larynx, trachea, and bronchi. The third

module has no external structural aid and consists of the inner lung parts: the bronchioles, alveolar ducts, and alveoli. (Kling 2011)(Treuting and Dintzis 2012)

Functionally, the mouse tract is divided into two zones, namely the conducting zone and the respiratory zone. Corresponding to humans, the mouse conducting zone is where the air is transported to and from the lung; it includes the nostrils, nasal cavity, pharynx, larynx, trachea, bronchi, and bronchioles. The respiratory zone is where gas exchange happens and consists of the terminal bronchioles, alveolar ducts, and alveoli. (Treuting and Dintzis 2012)

2.3.4 The Mouse Lung in Comparison to the Human Lung

The lung is an organ involved predominantly in gas exchange. It is mainly a sequences of bifurcating tubes initiating from the trachea and ceasing at the terminal bronchioles attached to the alveolar ducts and alveoli. Even though mouse and human lungs have similar anatomical organization, there are considerable differences in the overall histological arrangements and connective tissue elements. (Pan, Deutsch, and Wert 2019)(Suarez, Dintzis, and Frevert 2012)

Trachea and bronchial tree: The mouse trachea consists of 15-18 C-shaped cartilaginous rings in which the ends are bound together by a thin fibromuscular membrane. The rings become less organized due to loss of cartilage and increased smooth muscle as it forks into two primary bronchi at the carina within the thoracic cavity above the heart. These primary bronchi penetrate the right and left lung and are further branched in a monopodial pattern (which gives rise to 16-23 branches), in which the parent bronchi of the mouse lung produce smaller daughter segments that extend out at various angles giving rise to bronchioles and terminal bronchioles. (Pan, Deutsch, and Wert 2019)(Suarez, Dintzis, and Frevert 2012)

In contrast, the human trachea is a build-up of 15-20 U-shaped cartilage rings which, similarly to mice, are connected by thin fibromuscular membranes. It then branches to parent bronchi in the left and right lungs in a dipodal or tripodal manner. Human lungs have several

intrapulmonary segmental bronchi with submucosal glands and cartilage. Each segmental bronchus provides distinct bronchial fragments, which are further separated into several respiratory lobules (13-17 branches in humans). (Mercer and Crapo 1993) (Pan, Deutsch, and Wert 2019)(Suarez, Dintzis, and Frevert 2012)

Lung Lobes: The right and left lungs of the mouse have different numbers of lobes: the right lung is composed of four lobes: superior, middle, inferior, and postcaval lobes, while the left lung is a single lobe (Mercer and Crapo 1993) (Pan, Deutsch, and Wert 2019). Key anatomical differences between human and mouse lungs are summarised in Table 2.1.

Cells: A significant distinction between mouse and human lungs is in their cellular composition. The trachea in mice is made up entirely of Club cells and cartilage. The bronchi of mice lack cartilage and are composed of columnar psuedostratified epithelium composed primarily of surfactant generating Club cells and 23-36% ciliated cells. The bronchiolar epithelium then changes from columnar to cuboidal, and the proportion comprising ciliated cells declines while that of Club cells rises to 60-80%. Additionally, submucosal glands are only found in the trachea. Murine neuroendocrine cells are located in clusters within the bronchioles and in smaller clusters across the epithelial layers. In the respiratory zone, alveolar type 1 and type 2 cells, resident macrophages, and fibroblasts are present. (Pan, Deutsch, and Wert 2019)(Suarez, Dintzis, and Frevert 2012)

The human trachea, on the other hand, is made up of mucus-secreting goblet cells with cartilage rather than Club cells. The primary bronchi retain some cartilage, with the majority of cells being ciliated cells, along with goblet cells (10%) and serous cells (3%). The structure of the bronchi differs from the trachea in that as it descends the bronchial tree, there is a loss of cartilage and an increase in smooth muscle. In the bronchioles, the proportion of goblet cells decreases while the proportion of Club cells increases. Additionally, submucosal glands are

found throughout the bronchial tree. In the respiratory zone, cell morphology changes from psuedostratified columnar to cuboidal. (Pan, Deutsch, and Wert 2019)(Suarez, Dintzis, and Frevert 2012)

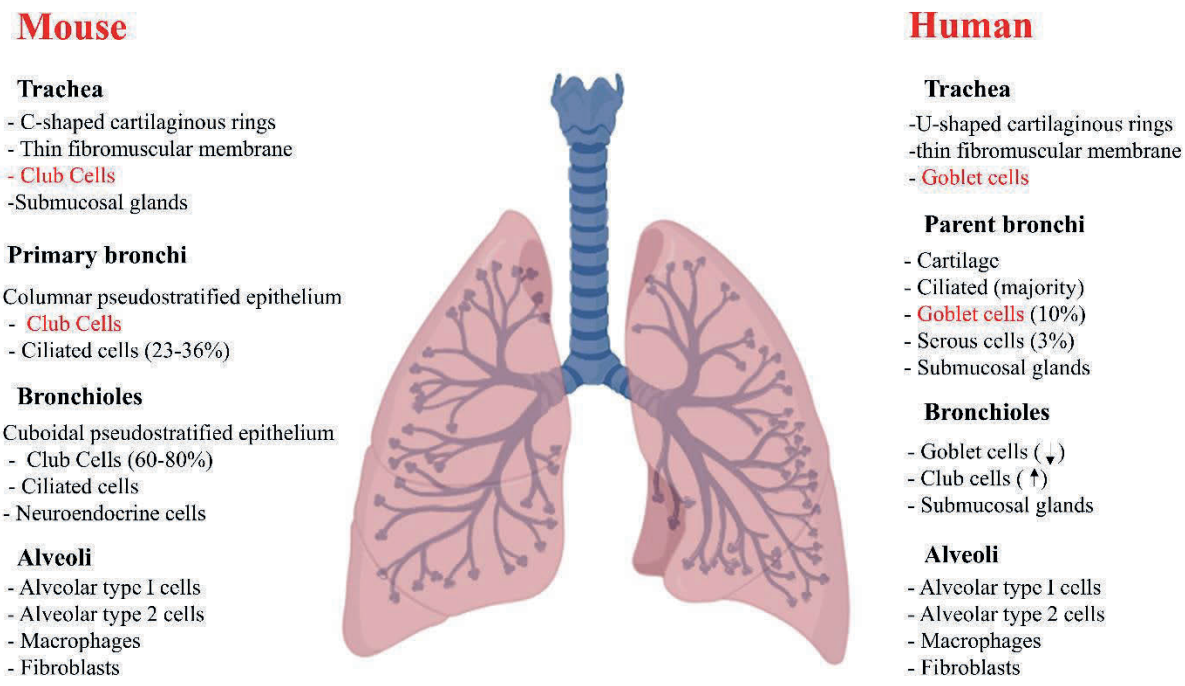


Figure 2.6. Mouse and human lung composition. General representation of the major cell types in different parts of murine and human lungs. [Created with BioRender.com]

Table 2.1. Comparison of Human and Mouse Lung Anatomy

	Human	**Mouse**
Number of Lobes	3 right lobes	4 right lobes
	2 left lobes	1 left lobe
Alveolar size	200-400 µm	39-80 µm
Trachea	Complete U-shaped rings	Cartilage less organized C-shaped rings
Bronchioles	Absent	Present
Airway branching	Dipodal- tripoidal	Monopodial

2.3.5 Lung Stem Cells and Their functions

The human lung has multiple specialized cell types to support various activities. Adult stem cells (ASCs) are more restricted in their potential to develop into different cell types than embryonic stem cells. ASCs, also known as somatic stem cells, may develop along a limited number of cell lineages (multipotent) or just one cell type (unipotent). A pool of ASCs are present in virtually all adult organs, repair and regenerate tissues throughout their development and after different kinds of injuries. ASCs produce terminally differentiated cells in high proliferative areas like bone marrow. There is no conventional stem cell hierarchy in tissues with modest proliferative ability, such as lung tissue. ASCs are triggered in cases of tissue injury or lung progenitor cell depletion. As mentioned previously, the stem cells might be involved in the development of radiation-induced side effects. (Pan, Deutsch, and Wert 2019)(Schilders et al. 2016)

2.3.5.1 Basal Cells

Basal cells have a cuboidal shape, are attached to the basement membrane, and are identified by the production of transformation-related protein 63 (Trp-63) and cytokeratins 5 and 14. In human lungs basal cells are present in respiratory epithelium from the trachea down to the bronchioles in decreasing numbers. Theses stem cells found in the conducting airways are essential for respiratory haemostasis and normal cell renewal and epithelial reconstruction after lung damage. (Pan, Deutsch, and Wert 2019)(J. D. Davis and Wypych 2021)(Schilders et al. 2016)

Basal cells constitute approximately 6-31% of alveolar epithelial cells in humans. They can differentiate into the essential lung cell types, including club, ciliated and, goblet cells. Several investigations have revealed the presence of at least two different subpopulations of basal cells in both murine and human respiratory systems, with ongoing research defining them such as

progenitor stem cells or basal cells dedicated to luminal differentiation (Pan, Deutsch, and Wert 2019)(J. D. Davis and Wypych 2021) (Crystal 2014) (Sit et al. 2019)(Schilders et al. 2016). Exposure to radiation or toxins such as cigarette smoke can lead to lung diseases as COPD and fibrosis. It has been shown that one of the earliest respiratory abnormalities seen in COPD patients and heavy smokers is basal cell overgrowth, indicating that these cells may play a critical role in disease progression. Chronic exposure to cigarettes may alter the genetic makeup of basal cells, causing them to enter a stressed condition and eventually lose their ability to regenerate. (Pan, Deutsch, and Wert 2019)(J. D. Davis and Wypych 2021)(Schilders et al. 2016)

Lung cancer is a disease strongly associated with smoking and may have basal cell involvement. A subtype of human adenocarcinomas has been identified with an overexpression of basal cell-associated genes, which was associated with a worse prognosis and shortened survival in comparison to other subtypes of adenocarcinomas. This suggests that changes to basal cells may be associated with more aggressive forms of lung cancer. (Pan, Deutsch, and Wert 2019)(Schilders et al. 2016)

2.3.5.2 Endothelial Progenitor Cells of Lungs

In the lungs, there are endothelial progenitor cells (EPCs), a subpopulation of circulating and resident vascular cells. The antibody reactivity phenotype of these cells is complex (positive for CD34, CD31, CD144, CD45, CD309, von Willenbrand factor, and nitric oxide synthase expression). As a consequence, determining the physiological functions and participation of potentially distinct EPC populations in tissue repair is challenging. Nevertheless, the small number of these markers in lung endothelium regeneration processes, as well as their paracrine interaction via exosomes, have been documented. EPCs may also help guard against chronic obstructive pulmonary disease by reducing inflammatory infiltration, slowing apoptosis, and increasing antioxidants. (Pan, Deutsch, and Wert 2019)(Schilders et al. 2016)

EPCs are implicated in the pathophysiology of a range of lung illnesses, including pulmonary fibrosis, asthma, and chronic obstructive pulmonary disease (COPD). Therefore, endothelial progenitor cells have been utilized as a potential treatment for these illnesses. Additionally, EPCs seem to be attracted to metastatic cancers in the lung, suggesting that engineering EPCs to express apoptosis-inducing proteins or other therapeutic molecules could be used in cell-based therapy techniques for lung cancer. (Weiss 2014)

2.3.5.3 Alveolar Type 2 Cells

Alveolar type 2 cells (AT2) reside in the alveolar sacs and are cuboidal in shape. AT2 cells produce pulmonary surfactant, which is required for normal lung function by moisturizing and reducing the surface tension of the lungs. Other functions of surfactant proteins include metabolic activity, innate host defence, fluid balance, and alveolar ion transport (A. Wu and Song 2021). AT2 cells act as progenitor stem cells and play a vital role in promoting epithelial healing in the alveoli. AT2 cells can proliferate and differentiate into alveolar type 1 (AT1), which are thought to be terminally differentiated because there is no evidence of them dividing. AT2 cells are usually non-proliferative with a turnover of 2-3 weeks. AT2 cells only comprise 7-10% of the alveolar area, while alveolar type 1 cells constitute over 90%, due to their long, thin, squamous morphology. (Pan, Deutsch, and Wert 2019)

AT2 cells are thought to be involved in different diseases such as chronic obstructive pulmonary disease (COPD), pulmonary fibrosis, cancer, and emphysema due to pathological changes in the alveoli. Pulmonary fibrosis is a degenerative condition that results in lung scarring. It is characterized by an abnormal growth of fibroblasts in the alveolar sacs and the build-up of extracellular matrix components. Recent research has demonstrated that silencing Cdc42 (a gene encoding a GTPase of a protein in the Rho-subfamily that modulates signalling pathways regulating cellular functions such as cell migration, morphology, and cell cycle progression (Qadir, Parveen, and Ali 2015)) in AT2 cells resulted in impaired alveolar

regeneration which progressed to fibrosis through activation of a TGF-signalling loop in AT2 cells in a model of partial pneumonectomy (H. Wu et al. 2020). Additionally, AT2 cells may be the primary cell type responsible for the development of human lung adenocarcinoma, and their oncogenic potential may be a direct consequence of their stem cell characteristics. The oncogenic G12D Kras mutation promotes the growth of AT2 cells in vivo and subsequent tumour development. (Desai, Brownfield, and Krasnow 2014)(A. Wu and Song 2021)

A number of different studies have identified sub-sets of AT2 cells that are activated following injury. Studies have identified these using different markers whether they are all different populations or the same population is unclear. One of the AT2 population express ScGb1a1 (secretoglobin family 1A member 1), which is a protein usually expressed on Club cells (Xu et al. 2020)(A. Wu and Song 2021). However, these cells have not been extensively studied for their role in lung growth and repair. Another subset of AT2 cells express Hnf1b1 and have stem cell potential, and may differentiate into cells in the alveoli and bronchioles; and when KrasG12D is expressed, these cells can develop adenocarcinomas and adenomas. (A. Wu and Song 2021)

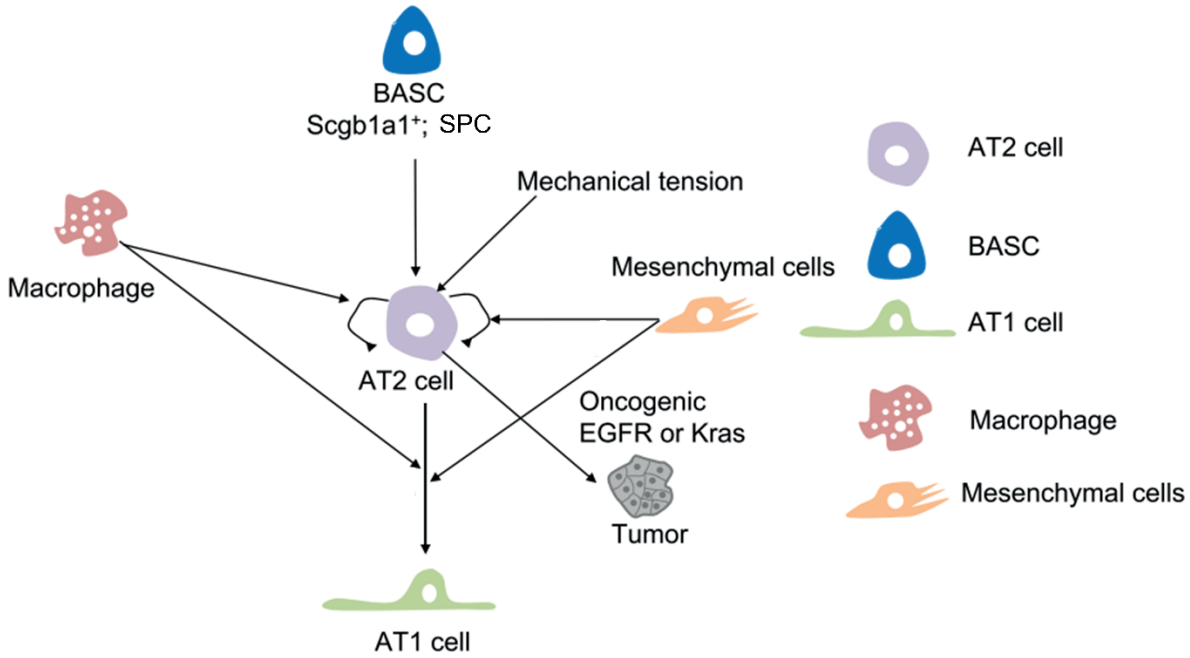


Figure 2.7. AT2 cell regulation during lung repair. AT2 cells are progenitor stem cells which can self-renew and also differentiate into AT1 cells following lung damage. Mesenchymal cells that reside near the AT2 cells regulate the regeneration and proliferation of AT2 cells by secreting signalling molecules. Inflammatory cells such as macrophages stimulate AT2 cells to promote the regeneration. Due to AT2 cells being progenitor stem cells, the expression of the oncogenic form of Kras and EGFR can effectively transform them to develop into lung tumours. The bronchoalveolar stem cells (BASCs) which express both Scgb1a1 and SCP can differentiate into AT2 cells to replace them during damage (A. Wu and Song 2021).

2.3.5.4 Club (Clara) cells

Club cells are non-ciliated stem cells that can self-renew to form new ciliated cells in the mouse's small airway. Club cells (previously Clara cells) are found in the distal airway epithelium and the bronchial tree, mainly at the terminal bronchioles making up 15-44% of all proliferating cells in this part of the lung. (Rokicki et al. 2016)(Barnes 2015)

Numerous defensive functions have been assigned to Club cells, including airway healing following injury, the release of immunomodulatory and anti-inflammatory agents regulating the immune system, and detoxification of toxins (Barnes 2015)(Ng Chee Ping 2013). One of the crucial functions of club cells is thought to be their protection of airways from external toxic and harmful chemicals. It has been established that when inhaling chemicals such as

furan, nitric oxides, and components of tobacco, club cells participate in their biotransformation by detoxifying these chemicals via cytochrome P450, monooxygenase, and flavin-containing monooxygenases. Several structural changes happen in club cells within an hour of exposure to these chemicals, which include mitochondrial enlargement, chromatin margination and clumping, and 24 h after exposure, club cells are enlarged. (Rokicki et al. 2016)

As tissue stem cells, club cells differentiate into intermediate mitotic Type A, which in turn divides to produce a ciliated and slightly differentiated daughter cell known as Type B. Type B cells can become club cells (Figure 2.8.). (Ng Chee Ping 2013)

Club cells, abundant around neuroendocrine regions, proliferate yielding ciliated cells. Club cells also operate as secretory cells, as shown by their production of Scgb1a1, a gene producing uteroglobin, the most prominent protein in the fluid lining the airways. Club cells and their secreted products are required for homeostasis. Their dysfunction contributes to a variety of respiratory conditions, such as fibrosis, asthma, and COPD. For example, uteroglobin, a protein secreted from club cells has been associated with anti-inflammatory and immunosuppressive properties, presumably by inhibiting monocyte and neutrophil chemotaxis and phagocytosis (J. D. Davis and Wypych 2021). Additionally, uteroglobin has been shown to inhibit leukocyte production of interferon and tumour necrosis factor-alpha (TNFα). Indeed, individuals deficient in uteroglobin are predisposed to an inflammatory condition. Smoking also has an effect on club cells. Serum uteroglobin levels are associated with a decreased risk of cancer death in smokers. Depleting club cells in mice airways inhibits the growth of lung tumours, suggesting that these cells may be involved in the development of pulmonary malignancies. Recently, it was demonstrated that asthma patients had decreased uteroglobin levels and in mice models, decreased uteroglobin was correlated with airway hyperresponsiveness. Interestingly, aberrant uteroglobin levels are connected with a broad variety of respiratory diseases. Nonetheless, research has started to elucidate club cells' functions beyond uteroglobin

production, including roles in regulating viral responses, barrier function, and host defence (Pan, Deutsch, and Wert 2019)(J. D. Davis and Wypych 2021)

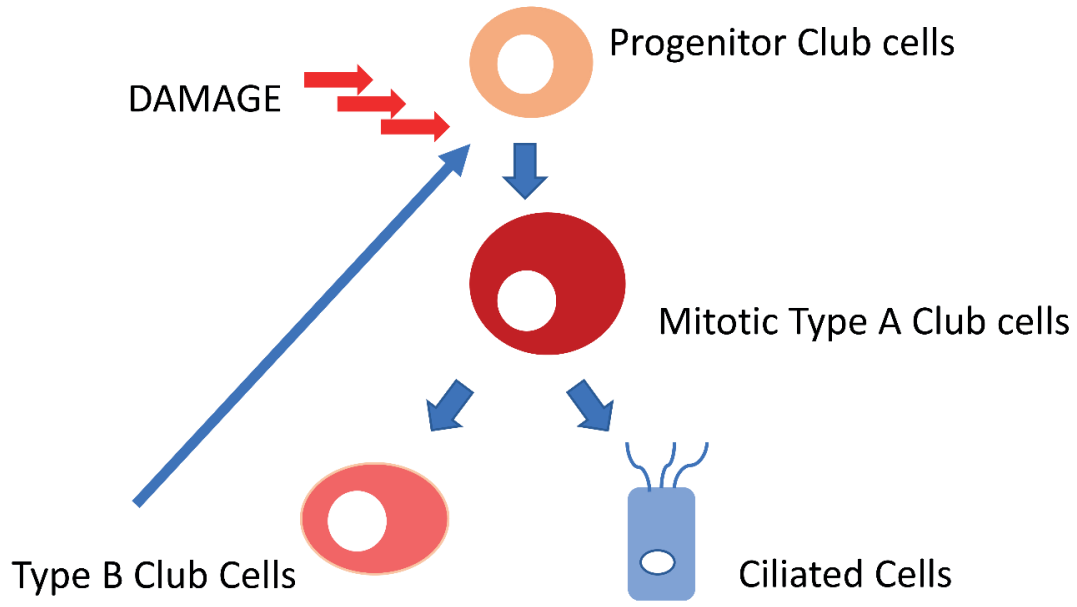


Figure 2.8. Club cell differentiation. When there is damage in the bronchi of the lungs, progenitor club cells sub-differentiate into mitotic type A which in turn divide and differentiate further into either ciliated cells or Type B club cells. Type B club cells can generate more progenitor club cells.

2.3.5.1 Bronchoalveolar Stem Cells

After club cell ablation following a parenteral administration of naphthalene, a widely recognised cytotoxicant of club cells (club cell knockout mouse by naphthalene)(Stripp et al. 1995)(Ng Chee Ping 2013), remaining cells at the bronchioalveolar junction may complete epithelial restoration and regenerate cells specific to these lung sites (Kawakita et al. 2020). These cells are known as bronchoalveolar stem cells (BASCs). In the hierarchy of stem cells, BASCs are said to be multipotent (Kawakita et al. 2020). BASCs are located at the junction of the bronchial and alveolar junctions. They are identified by both club cell and AT2 cell markers (Scgb1a1 and SPC) and may develop into club cells or ciliated cells in response to bronchial damage and into AT1 and AT2 cells for alveolar sac damage. BASCs have been demonstrated

in mice but have yet to be identified in humans. It is theorized that activation of BASCs by tissue damage can result in the development of tumours, suggesting that BASCs play a role in lung carcinogenesis. (Pan, Deutsch, and Wert 2019)(Q. Liu et al. 2019)

2.3.5.2 Mesenchymal Stromal Cells

Mesenchymal stromal cells (MSCs) are fibroblast-like cells that may be found in several tissue types, including lungs, and have varied protein expression profiles. They are present throughout the lungs in all of its lobes. Clinical studies for MSC-derived treatments have shown that these cells are effective mediators of tissue repair and regeneration (Sveiven and Nordgren 2020). Paracrine activities targeting epithelial, endothelial, and immunological cells establish the stromal environment and influence tissue regeneration. MSCs may migrate to damaged areas where they interact with and modulate neighbouring cells to promote tissue healing. Activated MSCs support cell survival, angiogenesis, and regeneration by releasing growth factors that impact cells in the surrounding tissues. MSCs also protect tissue integrity by suppressing ROS, a typical consequence of inflammation and tissue injury (including irradiation), thereby reducing oxidative stress. MSCs express several surface markers: CD13, CD106, CD124, CD44, CD73, CD90, CD105, CD45. As MSCs are multipotent and are being actively investigated in regenerative medicine, particularly in lung studies. (Pan, Deutsch, and Wert 2019)(Sveiven and Nordgren 2020)(Schilders et al. 2016)

2.3.6 The Pulmonary Immune System

As a strong immunological organ, the lung may produce protective immunity against respiratory infections without the participation or activation of the systemic immune system. Immunologically, the lung is divided into two compartments that are capable of interacting. Firstly, the upper respiratory tract consists of glandular and mucosal tissue with IgA as the predominant type of antibody. And secondly, the peripheral airways, which are devoid of

mucosal tissue and dominated by IgG antibody. In addition, the peripheral airways on the luminal side stay in continual interaction with broncho-alveolar cells, in which during normal homeostasis 90% are alveolar macrophages and 10% are lymphocytes. The respiratory lymphoid tissues are arranged within the bronchial walls and the lymphocytes of the respiratory system live across the epithelial membrane and in between the epithelial cells.(Gopal et al. 2020)

The lungs are constantly subjected to a wide variety of microorganisms as well as organic and inorganic pollutants. The respiratory system is made up of a variety of cell types and has developed sophisticated and efficient methods for screening out, inactivating, and eliminating extraneous elements. Mucociliary clearance and innate immune capabilities, such as the production of cytokines and antimicrobial proteins via resident leukocytes and pulmonary epithelial cells, which in turn recruit and activate the adaptive immune system. Therefore, mechanisms for detecting foreign substances and distinguishing potentially hazardous agents from harmless matter are essential. Higher vertebrates have two interconnected immune systems: innate and adaptive. The innate immune system consists of proteins that bind microbes and phagocytic leukocytes that circulate the bloodstream and are recruited into tissues at areas of inflammation or dwell in tissue to detect and eliminate foreign material. The innate immune system is presistently active and ready to identify and remove foreign particles and pathogens that reach the lungs. It has a relatively wide specificity that is based on the identification of common microbial characteristics. The adaptive immune system is comprised of lymphocytes that respond to the innate immune system signals by creating high-affinity antibodies to particular epitope sequences expressed on distinct antigen-presenting cells. In turn, these antibodies opsonize bacteria and viruses, allowing leukocytes to enter tissues and lymph nodes to destroy them. Cytokines and growth factors drive the adaptive immune system's specialized antibody responses as they are released by dendritic cells and

macrophages of the innate immune system. The innate and adaptive immune systems work together to allow the host to respond to a wide range of pathogens and other substances encountered daily. The major immune cells types in the lungs are: innate lymphoid cells (ILCs 1, 2, and 3), Natural killer cells (NK), dendritic cells, alveolar macrophages (AM), and interstitial macrophages (IMs) are all present in the lungs. (Gopal et al. 2020) (T. R. Martin and Frevert 2005)(Kumar 2020)

The capability of the lungs epithelium to identify pathogens via multitude of receptors is at the heart of the innate immune system of the lungs. These include different families of pattern recognition receptors (PRR), including the protease-activates receptor (PAR), bitter-and sweet-taste receptors, Toll-like receptors (TLR), and Nod-like receptor. (Hartl et al. 2018)

During acute inflammation, neutrophils are drawn first predominantly to the bronchoalveolar area, interacting with pathogens. Subsequently, monocytes and lymphocytes are recruited, infiltrating the parenchyma. It is important to note that lymphocytes may develop into ectopic lymphoid bodies. Aside from these well-known pulmonary immune system components, current research has highlighted new immune cells and mediators such as mucosal-associated invariant T cells and innate lymphoid cells, among others. (T. R. Martin and Frevert 2005)(Kumar 2020)

2.4 Models to Study Radiation-Induced Lung Toxicity

Given the long-standing problem of radiation-induced normal tissue toxicity in the lungs, experimental models have been employed to investigate radiation-induced normal tissue responses in preclinical settings. Yet the mechanisms are still unresolved, and radiation effects are still not well-understood (Lourenco 2017).

When a model disease system is employed, it is vital to be aware of the similarities and differences between the model and the clinical situation to identify the model's limits and ensure that the model is interpreted correctly. According to Bonfield et al., to ensure that a model provides the required circumstances, it is necessary to first evaluate the anatomy and physiology. Accordingly, a comparison between the chosen model's anatomy and physiology was made in the previous section to make a meaningful comparison to the human condition. The architectural patterns of the alveolar sacs and the bronchial tree has to be considered, as well as the milieu differences such as alterations in surfactant proteins and phospholipids, as well as physiological variables such as breathing rate and airway clearance processes. (Bonfield 2012).

Therefore, here, we provide a general overview of some of the available models and their benefits and limitations (summarized in Table 2.2).

Table 2.2. Comparison of experimental models for studying effects on lung cells/tissue

	Models			
	In vitro *(Cells in culture)*	**In vivo** *(Animals- mice)*	**3D** *(Organoids, Spheroids, cells on CHIP, ALI)*	**Ex vivo** *(Precision-cut tissue slices)*
All cell types represented	-	++++	+	+++
Normal tissue architecture	-	++++	+	+++
Normal physiology	-	++++	+	+++
Reproducibility	++++	++	+++	+++
Live cell imaging	++++	-	+++	+++
Ease of mechanistic studies	++++	-	+++	++++
Ease of running model	++++	-	++++	+++
Experimental control of cell environment	++++	+	+++	+++
Immune cells availability	-	++++	-	-
Long-term growth	++++	++++	+++	+

2.4.1 In Vivo Models

In vivo models are studies performed on live organisms. These models still serve as the foundation for research into anatomy, physiology, biological processes, as well as illnesses, and drug development. Prior to initiating clinical trials in humans, testing a prospective drug candidate's effectiveness, pharmacology, pharmacokinetics, and safety in animals (as surrogates for human subjects) remains the primary method to assess new medicines. In summary, the primary role of animal modelling is to provide an in vivo patient-relevant setting that enables the investigation of toxicity and the biological processes underlying disease and to provide a platform to evaluate novel interventional treatments on both the diseased and non-diseased tissues (Bonfield 2012). The striking anatomical and physiological commonalities between humans and animals, especially mammals, have motivated researchers to explore a variety of processes and evaluate new treatments in animal models before translating their findings to people. (Barré-Sinoussi and Montagutelli 2015)(Lourenco 2017)

Choosing the most appropriate model is contingent upon the nature of the issue being addressed and the rationale for adopting the model. Larger animals may be more comparable with human lung physiology and anatomy, but these models are not ethically or economically feasible when potentially suitable alternatives are available. On the other hand, the potential to use mice to study disorders such as cystic fibrosis is preferred where possible. While the exact disease may not be imitated, for example, the cystic fibrosis mice model does not acquire recurrent lung disease, the mouse models remain an excellent tool for studying infection-induced inflammation and, in certain cases, cell-specific disease effects. (Barré-Sinoussi and Montagutelli 2015)(Lourenco 2017) (Bonfield 2012)

To select a suitable model, it is necessary to identify the objectives of the study and understand that it is a balance between the clinical or mechanistic query. Animal models enable scientists to adjust and control several factors, including genetic background and habitat, to examine the

mechanisms involved in the development and treatment of a variety of lung disorders. Bonfield et al., in their article, describe different in vivo models with a focus on their advantages and weaknesses. (Bonfield 2012)

Much of our present knowledge on the normal response of the lung following radiation and the processes behind lung illness comes from animal research. Mice are the most widely used animal model, and they are also extensively used in lung research. The benefits of employing mice include a short reproductive cycle, a well-characterized genome similar to humans, a well-understood immune system, the introduction of transgenic technology (transgenic mice), and cost-effectiveness. Additionally, technologies have been developed to investigate human cells in mice, namely the xenograft models in immunodeficient mice such as SCID and nude mice (see section 5.3.3. for SCID), which makes it easier to study human cancers in mice. (Dabjan et al. 2016)(Lourenco 2017)

To study the side effects of thoracic irradiation, such as pneumonitis and fibrosis, which are the primary concerns of this project, Dabjan et al., provided an exhaustive overview. (Dabjan et al. 2016). The authors describe how C57BL/6 mice became the dominant model of IR-induced lung effects due to four factors, namely: their accessibility, being the most widely used for IR studies, their genetic background, and that they are prone to IR-induced fibrosis. More recently, Ghita et al., discussed how traditional thoracic radiation research gave critical information on the lung response of several mouse strains and established dosage criteria for lung toxicities.(Ghita et al. 2019). Additionally, a current finding in Wistar rats characterized dosage, location and time-dependent alterations when 50% of the total lung volume was irradiated, demonstrating that changes in pulmonary function were associated with pathological changes. The use of focal beam irradiators has resulted in significant improvements in the precision of dose delivery to small animals, including mice, enabling

experimental delivery of more clinically appropriate doses and fraction regimens.(Ghita et al. 2019)(Dabjan et al. 2016)(J. Martin 2020)

With all of the advantages stated above, utilizing animal models, particularly the mouse model in radiation research, does have some drawbacks. To begin, doing mechanistic investigations in vivo is challenging since it would involve extensive animal usage and costly technology that is not currently accessible in all laboratories. Additionally, this kind of research is difficult to finely control in animals since both the pharmacokinetics and pharmacodynamics of the medication have to be examined concurrently, complicating our understanding of the therapeutic effects. Most significantly, in vivo research is subject to many laws designed to protect animal rights and include the reduction, replacement, and refinement of animal experiments., therefore, alternatives to research on animals should be sought wherever possible. Additionally, some studies cannot be conducted on animals, as some compounds (especially those identified during early drug discovery) are not suitable for in vivo use (for example, if they are rapidly excreted or metabolized or not bioavailable). Some experiments could require the use of a large number of animals, such as drug combination studies without knowing what would be the most effective dose and schedule to test or what the appropriate biomarkers of effect would be, including what time they should be assessed. (Cornwell 2015)(Wilding and Bodmer 2014)

Dabjan et al. also discussed the difficulties inherent in adopting the C57BL/6 as a conventional model due to the widespread use of mortality and morbidity as measures for fibrosis rather than plethysmography, histology, and imaging. Moreover, the majority of studies in C57BL/6 employed whole-thorax irradiation (86%), and many did not take into account the effect of pleural effusions on these end goals. (Dabjan et al. 2016)(J. Martin 2020)

Despite its limitation, the C57BL/6 mouse model has been widely used mainly because it follows the general pathology of radiation-induced side effects in patients and would therefore be a choice for this work.

2.4.2 In vitro Cell Culture Models

In vitro cell, culture assays are widely utilized to screen and investigate compounds as potential therapeutic drugs. These are favoured for simplicity, the wide accessibility of cell lines, and low cost. Additionally, cell culture has made it feasible to perform large-scale studies, including high throughput screening, drug:drug combination studies, which are difficult and expensive to perform in animals. (Rockwell 1980)(Wilding and Bodmer 2014)(Hickman et al. 2014)

Although 2D cell culture has practical advantages for studying drug-radiation effects, there are some major limitations, for example: transformed cells are typically used (cancerous cells or fibroblasts), the correct tissue microenvironment is not present, there are usually limited cell-cell interactions, and tissue organization. Furthermore, physiological and toxicological endpoints are not possible, and cell signalling networks may be altered when cells are grown adhered to plastic compared with the native setting. (Hickman et al. 2014)

In recent years, techniques have advanced with co-culture of different cell types and the use of whole-genome RNA and DNA information to select disease-relevant cell lines, and the availability of techniques to knock down gene expression (e.g., siRNA) or to specifically modify gene sequences (e.g., CRISPR), which together made it possible to implement much more sophisticated in vitro studies. However, assessing primary cell effects is still a fundamental limitation of 2D cell culture methods. (Hickman et al. 2014) (Simian and Bissell 2017)

IR-induced normal tissue side effects such as fibrosis, and the complexity and time-course of the process in vivo, make it difficult to emulate the whole process in in vitro assays. However, there are available in vitro tests that can model certain aspects of fibrotic processes, such as myofibroblast migration, differentiation, and collagen synthesis. These techniques usually utilize primary human fibroblasts (e.g., from the lung) and can be helpful tools for determining the effects of drugs on human tissues (Sherman 2008). Other approaches have co-cultured fibroblast with other cells such as alveolar type 2 cells or macrophages to examine the effects on collagen production (Griffin et al. 1993). However, the development of fibrosis following IR is a multistep, complex biological process that is still incompletely understood but involves communication between multiple lung cell types and reorganization of lung architecture. Due to its complexity, lung fibrosis cannot be modelled in current 2D in vitro assays in a physiologically relevant way.

2.4.3 3D Cell Culture

Three-dimensional properties of tissues as well as cell-cell, and cell-matrix interactions are vital to understanding the biology and physiology of tissues and organs, and the effects of disease and drug treatments. Therefore, different types of 3D cell cultures have been developed, such as organoids, spheroids, and bioreactors, which try to capture some attributes of in vivo tissues while preserving the simplicity and manageability of in vitro models. (Hickman et al. 2014)

3D models facilitate the study of tissues that are difficult to study in animals and humans. Additionally, these models are not limited to tumour or stem cells, but some differentiated cell types can also be used in 3D cultures. Advancement in these models permits control of different additives and growth factors through, for example, microfluidic perfusion systems. In addition, co-culturing of tissue spheroids or organoids with myofibroblasts and immune cells may

increase the scope of biological processes that can be explored in vitro. (Simian and Bissell 2017)(Hickman et al. 2014)

However, 3D models exhibit significant drawbacks too, namely, not all the relevant primary cell types are present in spheroids or organoids, and the detailed hierarchical structure and microenvironment of tissues are absent. For example, for many 3D model systems, tissues are disaggregated and cell types separated, sorted, and reconstituted in vitro, which is likely to give rise to cell-cell interactions that are not found in vivo. (Hickman et al. 2014)

2.4.3.1 Organoids

Organoids are 3D constructs generated from progenitor and stem cells that replicate some organ's structural and functional elements, including lungs. Damage to the epithelia that encompass the different parts of the airways can cause inflammatory responses, which can progress into chronic obstructive pulmonary disease, bronchial asthma and fibrosis. Region-specific progenitor and stem cells have been identified the preservation of lung epithelia or the repair of lung cells following damage. Importantly, these stem cells can create lung organoids, which offer a novel platform for investigating human lung development and respiratory disorders. (Li et al. 2020)

Basal, Club, and AT2 cells may represent the primary innate progenitor cells for trachea, bronchi and alveoli, and have been intensively explored in murine lung models following the exposure of tissue injury and in organoid cultures. Furthermore, lung organoid cultures have been crucial in understanding mechanisms involved in restoring lung structure and functions during lung repair and studying cell-based therapies. In addition, recent studies on organoids coupled with clonal analysis and lineage tracing have revealed that there are yet more complicated and diverse resident progenitor and stem cells that become activated during lung injury. (A. Wu and Song 2021)

It is also crucial to note that different cell types are used in generating organoids depending on the experimental questions being studied and which cells are anticipated to be involved in the disease(s) under study. Wilkinson et al. created a model of chronic scarring similar to human fibrosis in lungs by treating organoids derived from human pluripotent stem cells with TGF-β (Wilkinson et al. 2016). There has been discussion about whether lung organoids require the use of feeder cells, for example, fibroblasts. It has been demonstrated that not all murine fibroblasts can act as feeder cells to promote the proliferation of organoid cultures, and only a subset, for example, immortalized MLg murine lung fibroblasts, can fulfil this role. (Li et al. 2020)

Organoids are likely to be a more effective model for studying how various cell types contribute to disease development compared with 2D methods. However, cells within organoids are not in their normal tissue structures, and not all tissue cell types are present, and cell:cell interactions may be non-physiological. Together this puts limits on the understanding of the underlying biological mechanisms of disease that can be addressed using this approach.

2.4.3.2 Organ-on-a-Chip

"Organ-on-a-chip" methods attempt to recapitulate the activities, mechanics, and physiological response of a whole organ or organ system in an in vitro system. These bioengineered devices enable control and adjustment of the tissue architecture, composition of the media, and cell-cell interactions. For example, combining lung cells with micro/nanoengineered devices has resulted in the development of novel in vitro models for the research of treatment approaches for respiratory disorders. Indeed, "lungs-on-a-chip" mimic the parenchymal shape and some physiological or pathological states in the human lung milieu, such as liquid-gas interfaces. The first lung-on-a-chip was developed in 2010 by Huh et al.; since then, further developments have enabled e.g., modelling of the alveolar-capillary junction of human lungs (Huh et al. 2010). The lung-on-a-chip device has been considered to be partway between a 2D and 3D

model (or “2.5D”) system because it comprises monolayers of endothelial and epithelial cells that aim to replicate the alveolar-capillary barrier allowing dynamic biomechanical perfusion changes that are analogous to those experienced during breathing. However, this model lacks important components of the tissue microenvironment, such as fibroblasts. Consequently, Sellgren et al. have developed a novel model for co-culturing fibroblast with endothelial and epithelial cells (Sellgren et al. 2014). Correspondingly, a human lung device has also been developed to simulate critical biomechanical phenomena associated with lung fibrogenesis, including alveolar tissue stiffness and contraction.(Asmani et al. 2018). This approach was utilised to predict the effectiveness of anti-fibrotic medications in patients with fibrosis, revealing that these therapies may decrease tissue contractility and reverse tissue stiffening (Picchio et al. 2021)(Asmani et al. 2018). Together, these 3D models have enabled researchers to understand some of the biological processes involved in lung disease. However, it remains a simplified model for in vivo settings, with the absence of complex tissue architecture, physiological cell:cell interactions, and extracellular matrix, which will restrict their utility, for example in studying fibrosis, the most problematic side effect of radiotherapy.

2.4.3.3 Air-Liquid Interface

Culturing pulmonary cells on microporous membrane scaffolding at the air-liquid interface (ALI) is an airway model whereby cells can be directly exposed to vapours, gases, and aerosols. (Cao et al. 2021)

Differentiated, organ air-liquid models (as opposed to immersed monolayer cultures) have in vivo-like characteristics and metabolic function and barrier systems that closely resemble those found in vivo. Additionally, exposure to drugs in the ALI systems may be more relevant to in vivo conditions than 2D or 3D models. The use of human cells in these cultures have enabled researchers to investigate the genesis of respiratory disorders such as COPD, fibrosis, and asthma. (Cao et al. 2021)

In the late 1980s, primary tracheal epithelial cells from guinea pigs were grown at the air-liquid interface. Through the porous gelatine barrier, two compartments were created that simultaneously exposed cells to air and growth media. Somatic primary airway cells developed into polarized mucociliary cell populations, reflecting the parent tissue from where they came. With advancements in stem cell culture, ALI models from human nasal, proximal and distal airway epithelium have been developed. In respiratory research, tracheobronchial epithelial models have been widely studied. Using semi-permeable membrane support (e.g., Millipore Millicell), normal human bronchial epithelial cells may be differentiated into an organotypic ALI airway model in situ. The exposed apical surface of the ALI culture provides oxygen to the epithelial cells and promotes differentiation. The microporous membrane nourishes cells in the basolateral compartment. When grown in biphasic culture, the normal epithelial cells form a polarized pseudostratified tissue-like structure mimicking the airway epithelium, with ciliated cells interspersed with goblet cells facing the apical side and basal cells extending along the basolateral membrane. During differentiation, the extracellular matrix is secreted and deposited on the basolateral epithelium. ALI preparations are more closely related to the natural epithelial tissues than submerged monolayer cultures. However, ALI cultures express more basal cell-related genes and genes involved in cell cycle and proliferation than in vivo tissue. (Cao et al. 2021)

Nonetheless, the ALI model is gaining popularity as a physiologically realistic in vitro culture method for respiratory research. Commercially available semi-permeable culture inserts can efficiently support the biphasic culture environment necessary for primary cell differentiation. ALI airway cultures go through three stages: primary cultures on plastic substrates, secondary cell proliferation on culture inserts in submerged settings, and primary cell differentiation on culture inserts in ALI conditions. Extracellular matrix proteins like collagen, gelatine, or fibronectin are placed on culture vessels to help cells connect and differentiate. Several

methods for ALI models have been established, and the degree of differentiation, cell population proportions, and overall shape vary depending on culture technique and the normal epithelial cells passage number. (Cao et al. 2021)

2.5 Ex Vivo Precision-Cut Tissue Slices

2.5.1 History of Ex vivo Tissue Slice Method

Organ culture was initially established in the mid-1920s. However, it was primarily employed to investigate the development of embryonic organs in vitro, as adult organs were more challenging to grow, as reviewed in (J. M. Davis 1967). However, Trowell, on the other hand, demonstrated in 1959 many developed organs could be kept in culture for up to 10 days. Trowell utilized sealed chambers with tissue supported on lens paper in a petri dish containing culture media. The petri dish was maintained in contact with a large gas reservoir that contained 95% oxygen and 5% carbon dioxide. It was noted that oxygen diffusion may be a limiting issue for successful culture and therefore concluded that a continuous gas flow could be advantageous. A technique was devised in which the gas was continuously pumped through the culture fluid, reoxygenating the tissue. The structure and architecture of guinea pig lung tissue were preserved for an extended length of time, up to 6-7 days, using this method (See Figure 2.3).(J. M. Davis 1967)(Trowell 1959)

Historically, the tissue explant models have been mainly used to study the brain; therefore, many articles describing the technique and model development were focused on this area. Many alternative methods have been tried to keep the brain tissue explants alive in culture. Among them is the roller-tube method, which was first proposed by Hogue in 1947, then refined by numerous scientists, and ultimately described in detail by Gähwiler in 1981. Slices of several different regions of the brain were cultured for many weeks using this method. The method entails adhering the explants to a glass coverslip with a clot made from chicken plasma.

The coverslip is then placed in a plastic test tube with sufficient medium and set on a roller drum that spins at a specified speed and angle. In 1991, Stoppini et al. presented a more straightforward method in which the explant is put on a transparent, porous membrane at the interface between air and medium, allowing the explant of central nervous tissue to be maintained in culture without the need for rolling. They discovered that the results achieved with this approach were similar to those obtained with the roller-tube technique.(Stoppini, Buchs, and Muller 1991) (Gähwiler 1981)(Hogue, 1947)

A review by Parrish et al. noted that the manual sectioning of the liver tissues yielded relatively thick and variable slices that were viable for only a short time. The review introduced two different automated sectioning machines (Krumdieck/Alabama Research and Development tissue slicer and Brendel/Vitron slicer) that enabled accurate and reproducible slices of near-identical dimensions.(Parrish, Gandolfi, and Brendel 1995)

Since then, laboratories have been interested in establishing reproducible precision-cut tissue-slice techniques to study different tissues and organs in culture, maintaining viability time period (Davies et al. 2015) (Bussek et al. 2009) (Sanderson 2011). Other groups have utilized precision-cut human lung cancer tissue as a clinically relevant model that does not require extrapolation of data from animal studies (Davies et al. 2015).

The groups of Siminski et.al. and Mendoza et al. have generated a protocol for maintaining mice lung tissue slices on gel foam. Additionally, this model has been used to study asthma and COPD (G. Liu et al. 2019) to study the movement of cells during alveologenesis using live-cell dyes and conjugated antibodies. (Akram et al. 2019) (Siminski et al. 1992) (Mendoza et al. 2010)

Although only resident macrophages were anticipated to be present in the precision-cut lung slice (PCLS) model, various viable immune cells, including macrophages, neutrophils, T-cells,

and dendritic cells, have been reported in murine PCLS. Additionally, the PCLS model has been used to study inflammatory responses and viral infections as well as co-infection with viruses and bacteria. Furthermore, PCLS are being used to image immunological interactions in real-time. The three-dimensional structure of the PCLS is critical for understanding the dynamic behaviour of immune response in vitro. By incorporating bio-imaging technologies into PCLS, it becomes possible to study the very earliest immunological processes, cellular responses, and host-pathogen interactions that would not be possible in vivo. (Bryson et al. 2020)(Lyons-Cohen et al. 2017)

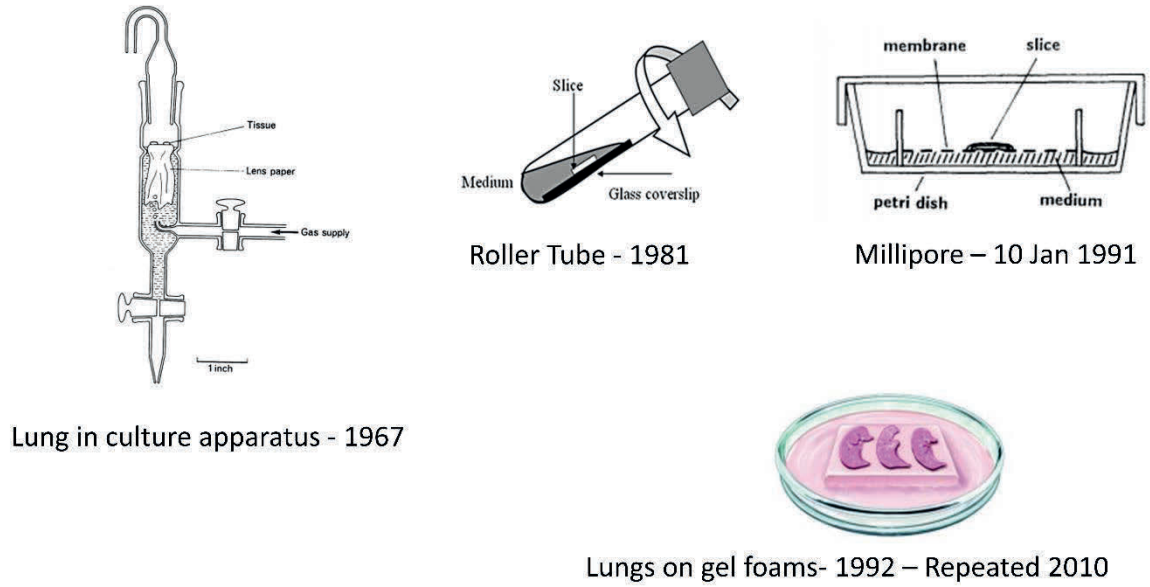


Figure 2.9. Schematic Timeline for Key Steps in the Development of Ex Vivo Lung Tissue Slice Models

1967: A gas chamber method where gas is supplied across tissue placed on a membrane.(J. M. Davis 1967)

1981: A roller tube method where a brain tissue slice is placed on a coverslip and into a tube and is rolled so that the tissue is in contact with constantly moving medium.(Cavaliere and Matute 2011)

1991: A brain tissue slice on a porous filter (e.g. Millipore) at a medium-air interface in a petri dish (Stoppini, Buchs, and Muller 1991)

1992: Mouse lung tissue slices on gelfoam (repeated in 2010).(Mendoza et al. 2010)

3 Research Objectives

The study goal was to determine if ex vivo precision-cut lung slices could serve as a surrogate for in vivo investigation of the effects of radiation and drug-radiation combinations and therefore serve as a bridge between in vitro and in vivo studies (Figure 2.10).

Aim 1: Establish the methodology for the ex vivo culture of precision cut lung slices from C57BL6 mice

Aim 2: Characterise the DNA damage response (DDR) in lung slices after radiation, and compare with in vivo DDR

Aim 3: Determine the impact of a DDR inhibitor on radiation responses in the ex vivo lung slice model

Aim 4: Determine the initial feasibility of studying DDR responses in individual cell types in ex vivo cultured lung slices

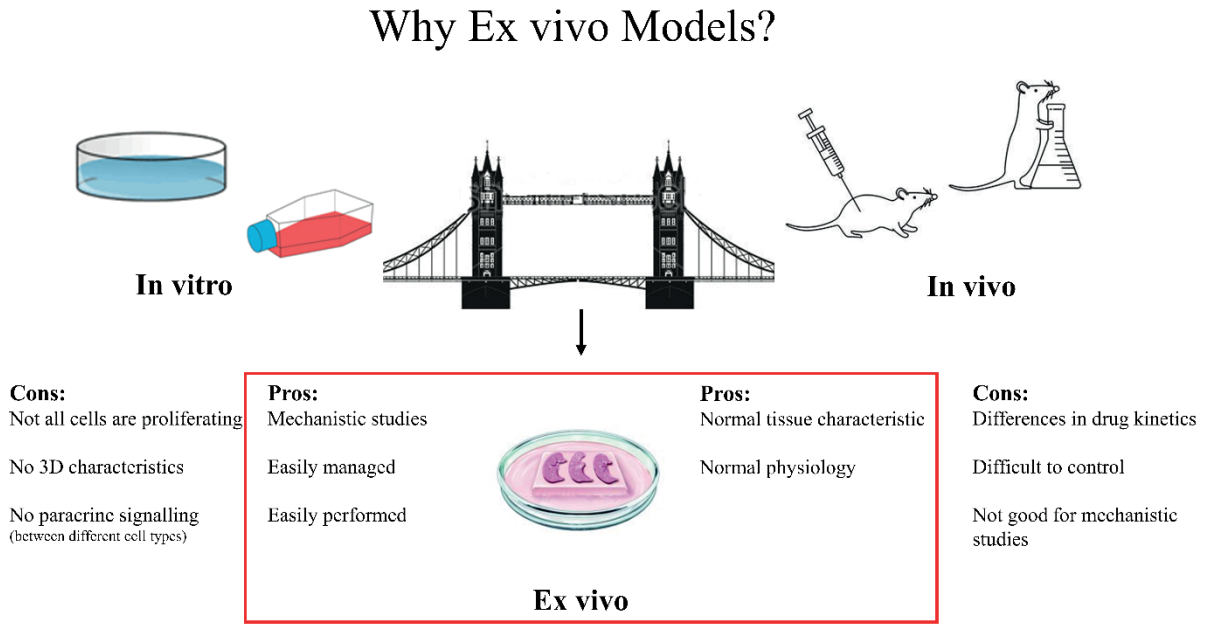


Figure 2.10. Ex Vivo Tissue Slices as a Bridge between In Vitro and In Vivo Models. In vitro and in vivo models have their own benefits and limitations and are used to study different experimental questions. The ex vivo models act as a bridge between the two models, making it easier to perform mechanistic studies while maintaining the normal tissue characteristics and physiology.

4 Methodology

4.1 C57BL/6 Lung Dissection

Performed by Dr. Yanyan Jiang under UK Home Office Project Licence PPL30/3395. Female C57BL/6 mice (6-8 weeks of age, Charles River, UK) were killed by a Schedule 1 method (euthanasia by an overdose of phenobarbitone followed by removal of the heart). An incision was made from the abdomen to the chest exposing the trachea, which was then separated from connected tissues. A catheter was inserted in the tracheal opening and was stabilised with a suture thread. The lungs were inflated using 1 mL of hand warm 4% low gelling temperature agarose in PBS perfused through the catheter. The lungs were then immediately dissected from the mouse and placed into PBS solution and placed on ice to allow the agarose to solidify.

4.2 Vibratome Slicing

The left lung was placed in warm (37°C) solution of 4% low gelling temperature agarose in PBS and then left in the fridge for 15 minutes to solidify. Excess agarose around the lung was removed and the lung-agarose sample was glued with super glue on to an Epoxy-coated metal buffer tray and left for 10 minutes to set, and then placed into an ice bath tray on a bed of crushed ice. Meanwhile the vibrating blade vibratome (Leica VT1200S) conditions were set: the blade was placed on the blade holder at a 90° angle and was lowered to the buffer tray setting the blade angle (17°), amplitude (3.00 mm), speed (0.60 mm/s), thickness (250 µm), and the distance of slicing according to the lung size. The slicing tray was filled with cold PBS (+Pen/Strep) and the lung was sectioned. The 250 µm slices were placed in a 6-well plate filled with PBS (+Pen/Strep). A control lung section was fixed in paraformaldehyde overnight directly after vibratome slicing, and then transferred into 70% ethanol and stored at 4°C for up to 7 days before embedding in paraffin wax.

4.3 Culture Conditions

4.3.1 Preparation of the incubating 6-well plates

6-well plates were prepared by placing Millicell Millipore filters (0.4 µm pore size 30 mm height) inside the wells using sterilised tweezers. The inner part of the filters was moistened using 1 mL of Advanced Dulbecco modified Eagle medium plus F-12 (DMEM F12) medium complemented with 1:100 Glutamax, 5% Fetal Bovine Serum, 1:100 penicillin-streptomycin and Primocin (1:500 dilution in media). When the filters were completely wetted (transparent) the medium was pipetted from the filter and the filter was placed into a tissue culture plate well and medium (1.65-2 mL) added to each well. Plates were left in the incubator overnight for the filter to stabilise.

4.3.2 Culturing

Newly sectioned 250 µm lung slices in PBS were positioned carefully on the pre-prepared Millicell Millipore filters inside a tissue culture hood and then incubated in a humidified environment containing 95% air and 5% CO_2 at a 37°C. The medium was changed every day unless stated until the end of the experiment, by removing 1 mL of medium and replacing with 1 mL of fresh medium.

4.4 Sytox Green Assay

Sytox green was diluted 1:100 in medium. 100 µL of the diluted Sytox green was added to the tissue sections which had approximately 50 µL of medium inside the filter. The tissues were then incubated (37°C, 5%CO_2) for five minutes and imaged with a Floid Cell Imaging Station (ThermoFisher).

4.5 Ionising Radiation

Tissue slices were irradiated with ionising radiation (γ rays) from a ^{137}Cs irradiator (GSR D1, Gamma Service Medical GmbH, Germany) at a dose rate of 1.35 Gy/min. Dosimetry was performed by the Mark Hill and James Thompson (Radiation Biophysics Group, Department of Oncology, (University of Oxford). Irradiated Gafchromic EBT2 dosimetry film (ISP Technologies, USA) was scanned and the optical density values converted to a dose using a calibration curve derived from known doses of irradiation.

4.6 Fixing, Processing and Embedding

Lung slices were gently removed from the millicell filter (at different time points according to the experiment) using a cell scraper and placed on to cell inserts with the assistance of 1 mL of PBS (further information in section 5.1.4.) noting which side of the tissue was at the filter interface and marking that side of the cell insert with a pencil. Cell inserts were put into cassettes and placed in a sealed jar with enough 4% paraformaldehyde to completely cover all cassettes (this was done to ensure that samples would not fold, later making the embedding procedure easier). After leaving overnight at 4°C, the samples were transferred into a sealed box containing 70% ethanol (ensuring samples were kept covered and flat). Within 10 days, the samples were processed (STP 129 Spin tissue processor) using an ethanol series (70%, 80%, 80%, 100%, 100%, 100%) followed by xylene (3 times) and paraffin (3 times).

Samples were then embedded into paraffin blocks (HistoStar™ Embedding Workstation). The procedure employed ensured both a flat lung slice was obtained and that the slice side that was on the filter was cut last. The cassette and cell insert were carefully opened. The slice was gently picked up with tweezers and placed in a pre-warmed metal mould, making sure that the slice side that was on the filter is facing us and the side that was at the air-interface was facing

the mould. Paraffin was then poured into the moulds slowly and carefully (making sure the slices did not flip). The lung slice was subsequently flattened using the curvature of the tweezers as well as a square-shaped stamp.

4.7 In vivo Experiments

Experiments were performed by Dr. Luiza Lourenco under a project license (PPL30/3395) issued by the UK Home Office under the UK Animals (Scientific Procedures) Act of 1986.

Mice were sedated with an intraperitoneal injection of 100 µL of a mixed solution at a final concentration of 8 mg/mL Ketaset and 100 mg/mL Dormitor in saline. The animals were anaesthetized within 5-10 min and then placed into the Gulmay Medical RS320 X-ray irradiator (set at 300 kV and 10 mA). The mice were covered with lead shields, leaving the thoracic area uncovered (roughly 1x2 cm) and 10 Gy of radiation was delivered at a rate of 1.82 Gy/min over 5 min and 30 sec. Following irradiation, the mice received an intraperitoneal injection of 100 µL Antisedan (stock concentration 0.25 mg/mL in saline), and they were placed in recovery rack at 37°C for about 30 min to completely recover from anesthesia.

4.7.1 Sampling left lung, fixing and processing

Mice were euthanized at different time points following radiation (2, 8 and 24 h) by receiving a 200 µL injection of 200 mg/kg sodium penobarbitone. Left lungs were dissected and placed in 10% neutral buffered formalin or 4% paraformaldehyde for 24 h at 4°C before being transferred to 70% ethanol. Within 14 days of collection, samples were processed using an automated tissue processor (Leica TP1050) using ethanol series (70%, 80%, 80%, 95%, 100%, 100%), then by xylene (3 times), and finally paraffin (3 times). The lungs were then embedded in paraffin blocks (HistoStar™ Embedding Workstation).

4.8 Preparation of the slides

Parrafin blocks were sectioned (4 µM) using a microtome (Leica RM2125) and the sections placed on charged glass slides (ThermoFisher Scientific, J3800AMNZ). The slides were left to dry at 37°C in an incubator overnight. Sections were then deparaffinised in citroclear and hydrated in a declining concentration series of ethanol (100, 100, 80, 80, 70, 50, 0%) for 3 min each. To detect 53BP1, γH2AX and SPC, antigen retrieval was carried out at 110°C for 2 minutes in citrate buffer (0.1M citrate, 0.05% TWEEN 20, pH 6.0) in a Decloaker Chamber (Biocare Medical). After 20 minutes of cooling, the slides were removed from the citrate buffer.

4.9 Immunohistochemistry (IHC)

Immunohistochemistry staining was performed using the Real EnVision Detection System HRP/DAB, Rabbit/Mouse (Dako) following the manufacturer's instructions. Following antigen retrieval, samples were washed in PBS for 3 min and blocked for 1 hour at room temperature with Mouse-on-Mouse Blocking Reagent (Vector Laboratories, MKB-2213) (for mouse antibodies). Incubation with the blocking reagent (Dako) was carried out for 1 h at room temperature. Slides were treated with diluted primary antibody (Table 3.2) in antibody diluent (Abcam, ab64211) over night at 4°C. The next day slides were washed for 3 times for 5 minutes with PBS and were incubated for 1 hour with polymer reagent (Dako kit) at room temperature. Slides were then washed in PBS (3 x 5 min). The stained sections were dehydrated in increasing concentrations of ethanol (50-100%) and then xylene, and were then mounted with DPX and scanned using the Aperio ScanScope CS digital slide scanner (20X objective with 2x doubler) and viewed with ImageScope Software (v11.2.0.780).

4.10 Analysis of IHC

Using ImageScope (v11.2.0.780), we identified positively stained cells in 2 random selected fields of view for each sample (for sections from in vivo lungs around 200 cells were counted and for sections from ex vivo lung slices around 100 cells were counted due to the ex vivo

samples being inflated while the in vivo were not). Each experiment was done twice and for ex vivo samples there were two experimental replicates. Samples (positive staining) were counted manually.

4.11 Haematoxylin and Eosin Staining

Sections of lung slices were stained by Harris Haemotoxylin for 5 min and were then washed for 3 min under running tap water. The slides were then dipped 10 times in 1% acid alcohol then in Scott's tap water and 0.5% lithium carbonate and washed with water after each of the reagents. Before the Eosin staining the samples were dehydrated with series of increasing concentrations of ethanol and then placed in the eosin solution for 3 min. The slides were then washed with 90%- 100% ethanol until the samples were clean. The slides were then dehydrated using increasing concentration of ethanol and then placed in xylene and mounted with DPX and scanned using the Aperio ScanScope CS digital slide scanner (20X objective with 2x Doubler) and examined with ImageScope Software (v11.2.0.780).

4.12 Double Staining Immunofluorescence (IF)

Tissue sections (4 µm) were washed with PBS three times and then blocked for one hour with 5% goat serum, 2% BSA 0.5% triton X-100 in PBS (blocking buffer) at room temperature. The tissues were then stained with two primary antibodies: γH2AX (mouse) and 53BP1 or SPC (rabbit) diluted in blocking buffer, overnight at 4°C. The slides were washed with PBS three times for five minutes and incubated in Alexa flour 488 goat anti-mouse IgG and Alexa flour 555 goat anti-rabbit IgG diluted in blocking buffer for one hour in a dark chamber at room temperature. The slides were counterstained and mounted with Fluoromount medium containing DAPI (0.1 µg/mL). The edges of the cover slip were sealed with nail polish to avoid the movement of the slides. Slides were stored in 4°C in the dark before microscopic analysis.

4.13 Detection of dual stain (IF)

Images were acquired using LSM 710 point scanning confocal microscope (Carl Zeiss, Germany), using a 63x / 1.40 NA Oil DIC M27 Plan-ApoChromat objective. DAPI was excited with laser line 405 nm and emission collected between 410 nm and 507 nm. "GREEN" was excited with laser line 488 nm and emission collected between 495 nm and 573 nm. "RED" was excited with laser line 561 nm and emission collected between 568 nm and 697 nm.

4.14 Analysis of IF

Zen software (Zeiss) was utilized to analyse the IF stained pictures. The images collected from the Ziess710 as a z-stack, were combined to create a maximum intensity image. Positive cells and foci were manually counted. All cells in a field of view were counted (~300-400 cell nuclei for sections from in vivo lungs and 50-75 cell nuclei for sections from ex vivo tissue slices).

4.15 Statistics

Data are presented as means ± SEM unless otherwise stated. Data were tested for normality using the Kolmogorov–Smirnov test (GraphPad Prism). Unless otherwise stated data had a normal distribution (by Kolmogorov-Smirnov test) and were analyzed by ANOVA or T-test as indicated in the results. Data with non-normal distribution (by Kolmogorov-Smirnov test) were analyzed with a non-parametric test (Mann-Whitney). All statistical analyses were considered exploratory and therefore no corrections were made for multiple comparisons.

Statistical significance was assumed if $p \leq 0.05$. *$p \leq 0.05$, **$p \leq 0.001$, ***$p \leq 0.0001$. NS or ns = not statistically significant ($p > 0.05$).

Table 3.1. Reagents List

Reagents	**Company**	**Cat. No.**
Acetic Acid	BDH Chemicals	100012k
Agarose	Sigma-Aldrich	A6013-25G
Bovine Serum Albumin	Acros Organics	9048-46-8
Citrate buffer	TCS Biosciences	HC5005
Citroclear	TCS Biosciences	HC5005
Collagenase D	Sigma-Aldrich	11088858001
Criterion™ TGX gels	Bio-Rad	5671085
Dimethylsulfoxide (DMSO)	Thermo Scientific	85190
DPX Mount	Sigma-Aldrich	44581
Dulbecco Modified Eagle medium plus F-12	Life Technologies	12634-010
Eosin	Sigma-Aldrich	HT110132
Ethanol	Fisher Chemicals	E/0665DF/17
Fetal bovine Serum	Sigma-Aldrich	F7524
Flouroshield with DAPI	Sigma	F6057-20ML
Glutamax	Life Technologies	35050-038
Goat Serum	Millipore	S26-100ML
Haematoxylin Aqua	Sigma Aldrich	SLCH6216
Harris Haematoxylin	VWR	351945S
Methanol	Sigma-Aldrich	32213
Nitrocellulose membrane (0.45 µm pores)	Bio-Rad	162-0115
Paraffin (Histoplast)	Thermoscientific	8330
Paraformaldehyde	BDH Chemicals	28794.295
Penicillin-streptomycin (Pen/Strep)	InvivoGen	ant-pm-1
Phosphate-buffered Saline (PBS)	Lonza	BE17-517Q
Ponceau S solution	Sigma-Aldrich	P7170
Primocin	Sigma-Aldrich	534056
Protease inhibitor	Complete	11697498001
REAL EnVision Detection System HRP/DAB/,Rb/Mo	DAKO	K406511
Red Blood cell lysis	Roche	11814389001
Running buffer (10x)	Bio-Rad	1610732
SDS Page Sample buffer 5X Concentration	Jena Bioscience	114.149
Sodium hydroxide (NaOH)	BDH Chemicals	28244.262
Superglue Pen	RS Pro	473-445
Sytox Green	Invitrogen	S7020
Transfer buffer (10x)	Bio-Rad	1610734
Triton X-100	BDH Chemicals	437002A
Tween-20	Sigma-Aldrich	P1379-500mL
Xylene	Sigma-Aldrich	534056

Table 3.4. Drugs

	Company	**Cat. No.**
NU7441	Selleckchem	S2638

Table 3.2. Primary Antibodies

	Company	Cat. No.	Dilution	Incubation
Primary Mouse anti-phospho-histone H2AX (ser139)	Millipore	05-636	1:1000 (IHC)	ON 4°C
Primary Rabbit anti-53BP1	Cell Signalling	4937	1:1000 (IHC)	ON 4°C
			1:20000 (IHC)	ON 4°C
Pro-surfactant C (Spc)	Abcam	ab90716	1:2000 (WB)	ON 4°C
β-actin (mouse)	Sigma-Aldrich	A1978	1:20000 (WB)	ON 4°C

Table 3.3. Secondary Antibodies

	Company	Cat. No.	Dilution	Incubation
Alexa flour 488 goat anti-mouse IgG	Life Technologies	A21422	1:400	1h RT
Alexa flour 555 goat anti-rabbit IgG	Life Technologies	A11008	1:400	1h RT
Mouse IgG (H + L) conjugated to IRDye® 680RD	LI-COR Biosciences	926-68070	1:5000	1h RT
Rabbit IgG (H + L) conjugated to IRDye® 800CW	LI-COR Biosciences	926-32211	1:5000	1h RT

Table 3.4. Mice

	Company	Strain code	Age
C57BL/6	Charles River	027	Female 6-8 weeks old
SCID CB17/Icr-Prkdc ^{SCID}/IcrIcoCrl	Charles River	236	Female 6-8 weeks old

5 Results

5.1 Establishment of the Ex Vivo Precision-Cut Lung Slice (PCLS) Model

5.1.1 Introduction

Tissue slices have been used as research tools since the 1960s, and many changes have been made since then to create a simple, reproducible procedure that keeps cells alive and in their original structure for an extended period of time. Mendoza et al. (Mendoza et al. 2010) established a working protocol for ex vivo precision-cut slices of mouse lung, which we modified based on prior knowledge of other tissue slice protocols and established a protocol in our lab that yields live tissue slices for up to 7 days following mouse lung sectioning in a well-controlled and reproducible environment (Fig 5.1).

Although Mendoza et al. used gel foams to keep the lungs in culture we used Millicell-CM (Millipore) filters as described by others for brain and other tissues. (Stoppini, Buchs, and Muller 1991) (Davies et al. 2015)

Due to its strain stability and ease of breeding, the C57BL/6 mouse strain is one of the most commonly used mouse strains in biological research. In 2002 this was the first mouse strain to have its whole genome sequenced, soon after the completion of the human genome. C57BL/6 mice have been widely used to investigate radiation-induced lung fibrosis, a late toxicity (occurring ≥ 6 months after treatment) that can develop following exposure to external beam ionising radiation both in mice and in humans. Compared with males, female C57BL/6 mice were found to be more sensitive and to have a shorter latency period before exhibiting symptoms of lung toxicity following irradiation. (Travis et al. 2011) As the effects of irradiation were the major interest for this project, we focussed on ex vivo precision-cut lung slices from C57BL/6 mice.(Lourenco 2017)(Dabjan et al. 2016)

The PCLS method that we have established and used in this project is shown in Figure 5.1 (detailed in Table 5.1). The experimental steps were investigated and adjusted to enhance the overall performance of the PCLS model and are explored in more detailed below (See 5.1.2-5.1.5)

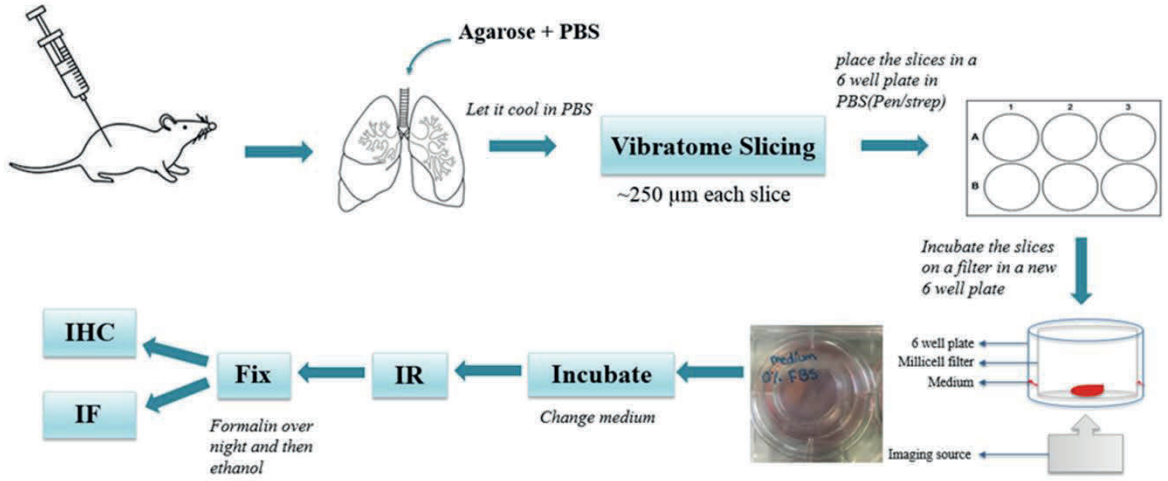


Figure 5.1. Summary of the mouse PCLS model.
A C57/BL6 female mouse is sacrificed and lungs are dissected and perfused with agarose and left to solidify at 4°C (see methodology for more details). The left lung is separated from the right and placed in warm agarose prior to vibratome slicing. The lung is thesn sectioned into 250 µm slices which were picked up from the vibratome tray and placed in PBS. Following slicing samples are then placed in the well of pre-prepared 6-well plate containing a millicell filter and medium and then incubated at 37°C, in 95% air 5% CO_2. Tissue slices are incubated overnight to stabilize and then irradiated. Following treatment (according to experimental protocols), the tissue slices are fixed in formalin and then stored in 70% ethanol in the fridge until the end of the experiment. The fixed tissue slices are then processed and embedded in paraffin wax before sectioning and staining by IHC and IF.

Table 5.1. A summary of the sectioning and culture conditions investigated for mouse PCLS.

Preparation	
Time for agarose to solidify	15 min
Position of the lung	Posterior glued to slicing tray
Time limit for slicing (from dissection to incubation of slices)	Max 45 min
Vibratome	17°
Angle of the blade	0.60 mm/s
Speed	3.0 mm
Amplitude	250 µm
Thickness of slices	
Culture conditions	
Filter	Millicell Biopore hydrophilic PTFE cell insert, 0.4 µm pore size 30 mm height
Medium choice	Advanced DMEM F12
Glutmax	1:100
Penicillin- streptomycin	1:100
Fetal bovine serum	5%
Primocin	1:500
Volume of medium	1.65-2 mL
Changing the medium	Removing 1 mL of medium and adding fresh 1 mL
When to change the medium	Every day

5.1.2 Tissue sectioning with a vibratome (Leica VT1200S)

A vibratome is an instrument that is similar to a microtome but which uses a vibrating blade to cut through tissue. Tissues sliced on vibratomes retain tissue morphology and have minimal compression deformation and cell damage. The amplitude, speed, and angle of the vibrating blade can each be controlled, and need to be optimised for each tissue type. The lung is difficult to section with a vibratome as it easily deforms due to the large proportion of air within the tissue. In order to maintain tissue architecture, whole lungs were inflated with low-gelling temperature agarose (Sanderson 2011) which was solidified by cooling prior to sectioning (See Methods). Using this methodology, we reproducibly achieved 7-12 tissue sections of 250 µm thickness from the left lung, and 13-15 sections of 250 µm thickness from the right lung. Lung sections of 250 µm were the thinnest that we could reproducibly produce using the Leica VT1200S vibratome. The left lung was chosen for future work, as in the mouse the left lung consists of a single lobe and in our hands, it produced more uniform sections for the in vitro studies.

5.1.3 In vitro culture: Filter choice

According to Davies et al. the morphology of tissues cultured on filters was better preserved in comparison to tissues floating within cell culture media (Davies et al. 2015). In addition, previous studies have suggested that in vitro culture of tumour slices on filters creates an air-liquid interface that can reduce tissue hypoxia (Davies et al. 2015). Therefore, filter choice was likely to be important to support the tissue above the medium at an air-liquid interface for the model setup. We selected Millicell Biopore PTFE membranes (0.4 µm pore size, diameter 3.15 cm, and height 30 mm) due to their optical transparency and potential suitability for future live cell microscopy and immunofluorescence studies.

5.1.4 In vitro culture: Media

Millicell PTFE filters are hydrophilic and designed such that media moves freely from the well through to the tissues. In preliminary experiments, samples quickly dehydrated when there was insufficient medium inside the filter. We determined that 1.65 –2.0 mL of medium in a 6-well tissue culture dish was sufficient to keep the filter sufficiently wetted from both sides and to maintain an air-liquid interface for tissue slice (see Supplementary Table1.). Medium was initially changed every other day following published methodology of (Mendoza et al. 2010) and then daily until the end of the experiment. However, this was then modified to changing media every day as changing every other was insufficient to routinely prevent signs of tissue stress and loss of tissue integrity.

Various media and serum concentrations were tested to identify suitable culture conditions for the culture of mouse lung tissue slices. Tissue integrity was assessed by bright field microscopy and H&E staining, and cell viability was assessed by Sytox green staining and the production of gH2AX nuclear foci following irradiation which is an active enzymic process requiring ATP (Francisco and Francisco 2008).

Bright field microscopy indicated an intact tissue structure was maintained in tissue slices incubated in F12/DMEM medium for up to day 7 post-incubation with or without the addition of serum (FBS; up to 5%) (Figures 5.2 and 5.3). Fig. 4.4 shows the integrity is maintained in slices cultured in 0.5% and 5% FBS compared with a section taken immediately after vibratome sectioning.

We then evaluated the integrity of the cellular DNA damage response (DDR) by assessing the induction of γH2AX and 53BP1 nuclear foci following irradiation. H2AX is a variant form of histone H2A that is phosphorylated at ser139 by the DNA-damage responsive kinases ATM, ATR and DNA-PK (Francisco and Francisco 2008). By convention, phosphorylated H2AX is

termed γH2AX, and it can be detected as nuclear foci at sites of DNA double strand breaks (e.g. after ionising radiation exposure). 53BP1 is a nuclear protein that is actively recruited to, and accumulates at, sites of DNA double strand breaks following radiation, where it can also be also detected as nuclear foci (Gupta et al. 2014). Together, the generation of both γH2AX and 53BP1 foci indicate an intact DDR signalling pathway requiring precise protein modification and intranuclear protein trafficking suggesting that cells are metabolically active and viable.

Tissue slices were incubated for up to 7 days, and then irradiated (10 Gy) and 2 h after irradiation (to allow DDR repair foci to form), the slices were fixed and stained by IHC for γH2AX and 53BP1. Tissue slices cultured in DMEM/F12 with the addition of 0.5% or 5% FBS showed an intact DDR (as evidenced by the induction of nuclear foci), even after 7 days in culture (Figures 5.5 and 5.6). In contrast, cells incubated with PBS or defined media (M199) did not form DDR foci following irradiation.

Sytox green is a cell impermeant nucleic acid stain for distinguishing dead cells from live cells. Loss of membrane integrity associated with cell death allows Sytox green to enter the cell and bind to double stranded DNA whereupon it becomes highly fluorescent. Sytox green staining of lung tissue slices demonstrated widespread cell death in lung slices cultured in PBS or DMEM/F12 without the addition of FBS (Figure 5.7). Slices cultured in DMEM/F12 with 5% FBS had lower levels of cell death than slices cultured in 0.5% FBS (Figure 5.7).

It has been reported that in tumour slices cultured ex vivo, cells in tissue immediately adjacent to the filter can develop hypoxia during culture (Davies et al. 2015). In our studies we identified which side of the section was adjacent to the filter. Tissue sections are gently picked up from the filter using a cell scraper and placed on a cell insert. PBS (1 mL) was used to slide the tissue on to the cell insert by pipetting out the PBS parallel to the cell scraper. The cell

insert could then be marked with a pencil to note which side of the tissue was towards the filter. Following processing, tissues were embedded with the tissue side exposed to air towards the front of the block (i.e. these were sectioned first).

5.1.5 Structural integrity and cellularity throughout the seven days of the ex vivo precision-cut mouse lung slice model

To evaluate potential changes in structural integrity and the DDR response throughout 7 days of culture, we irradiated different sections on day 1 (D1), day 3 (D3) and day 7 (D7) with 10 Gy. Irradiated and mock irradiated samples were fixed 2 h following irradiation on each day and were evaluated by H&E, γH2AX and 53BP1 staining. Throughout the 7 days in culture irradiated samples demonstrated an intact DDR confirmed by expression of γH2AX and 53BP1 foci, although there was also some occasional staining in mock irradiated samples. Though the alveolar structures were generally intact throughout the 7 days of culture some disruption in broncho-epithelial cells was noted from day 3 onwards, with widespread disruption by day 7. (Figure 5.8)

5.1.6 Immunofluorescence (IF) visualisation of DDR foci

Quantifying DDR foci with insoluble deposits of chromogenic stains (e.g. DAB) by IHC is challenging as the nuclei in the most common cell in the lung (alveolar cells) are too small to make counting individual foci practical (Figures 5.5 and 5.6). IF methods offer the potential of higher resolution imaging of foci using confocal microscopy, and could also allow double staining for both γH2AX and 53BP1. Initial experiments demonstrated the feasibility of this approach (Figure 5.9) which was further developed into a quantitative assay for DDR in specific cell types in the lung tissue (see section 5.4).

5.1.7 Discussion

We established a protocol to generate and maintain precision-cut mouse lung slices for up to 7 days in DMEM/F12 medium supplemented with 5% FBS when grown on Millicell Biopore PTFE filters (Table 5.1).

The single-lobed left lung was preferred as the multi-lobed right lung produced irregular slices, likely due to the more complex bronchial tree. In contrast, the left lung reproducibly produced more uniform slices suitable for ex vivo culture and subsequent tissue analysis. The lung slices were viable for at least 7 days (Sytox Green staining), and retained an intact DDR response (induction of γH2AX and 53BP1 foci) and alveolar tissue architecture (H&E, bright field microscopy). Because, broncho-epithelial architecture showed evidence of disruption from day 3 onwards, experiments in the present work were generally limited to 2 days in culture, consistent with the observations of others (Sanderson 2011). Future studies are required to identify whether the changes seen from day 3 onwards are a specific biological response to sectioning and culture, or a non-specific response associated tissue damage and cell death. Also, further work is required to determine whether viability and DDR responsiveness are similarly retained across the major cell types in lung tissue (e.g. type I and II alveolar cells, broncho-epithelial cells, endothelial cells, fibroblasts).

A limitation of the tissue slice model is that it does not have an intact inflammatory/immune response, although tissue-resident macrophages are present. This has to be noted when comparing irradiated ex vivo slices to irradiated in vivo lungs to evaluate any differences that could be affected by this.

Despite the high degree of cell viability and the intact DDR following irradiation, there were some signs of disruption of lung architecture after 3 days culture when compared with sections fixed directly after tissue slicing. Surprisingly, tissue sections cultured in PBS retained

recognisable tissue architecture although a large proportion of the cells were not viable. This suggests that the broncho-alveolar structure of the lung can persist even after extensive cell death, possibly because the supporting extracellular matrix is not degraded.

Immunohistochemical quantification of DAB-stained DDR foci in lung tissue is impractical due to the small size of the nuclei in lung alveolar, endothelial and fibroblast cells. In contrast, immunofluorescence using confocal microscopy appears to be a suitable method for both the visualisation and quantification of DDR foci. Occasional cells in unirradiated lung slices were positive for both γH2AX and 53BP1 foci. The nature of these cells is not known, but they could represent cells damaged during the tissue slicing procedure. Experiments described later in this thesis establish quantification methods to evaluate the DDR in individual cell types for up to 3 days after radiation, and then compare the results to parallel lung samples obtained from in vivo studies. Here we have established a method for culturing PCLS from mice that retain tissue integrity and viability for at least 2 days, and which are suitable for investigating the DNA damage response following treatment with ionising radiation. Subsequently the ex vivo tissue slice model will be used to study the response to combination of radiation and DDR modulators/inhibitors such as DNAPK inhibitors.

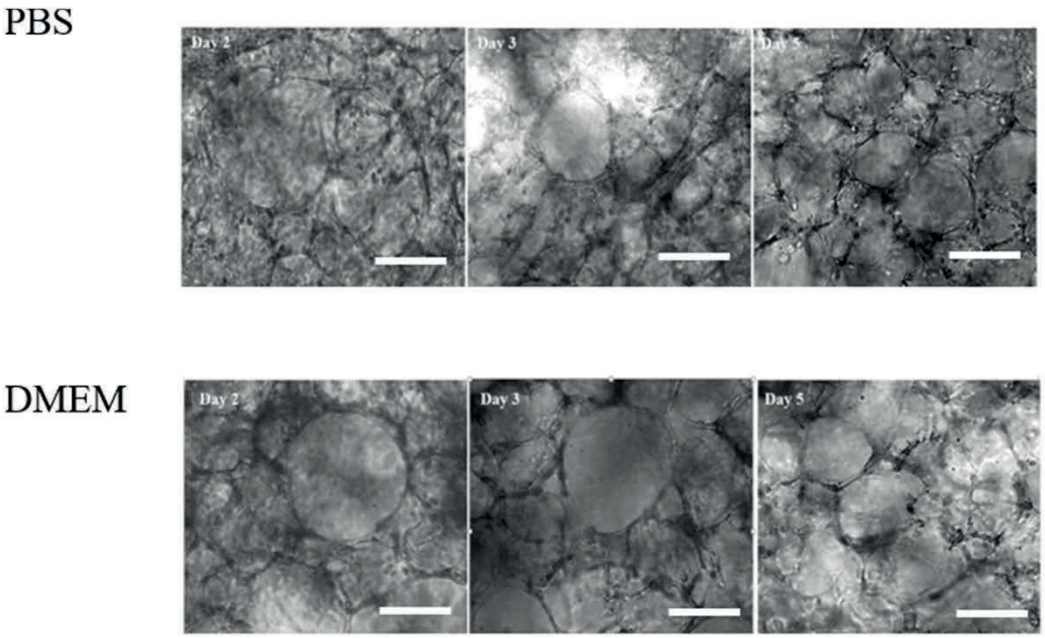


Figure 5.3. The cellular integrity of lung tissue slices incubated in PBS and DMEM/F12 plus 5% FBS.
Cellular integrity of tissue slices decreased over 5 days in in PBS, but is retained in the DMEM/F12 5% FBS, with less evidence of cellular dissociation and debris. Scale bars represent 100 µm.

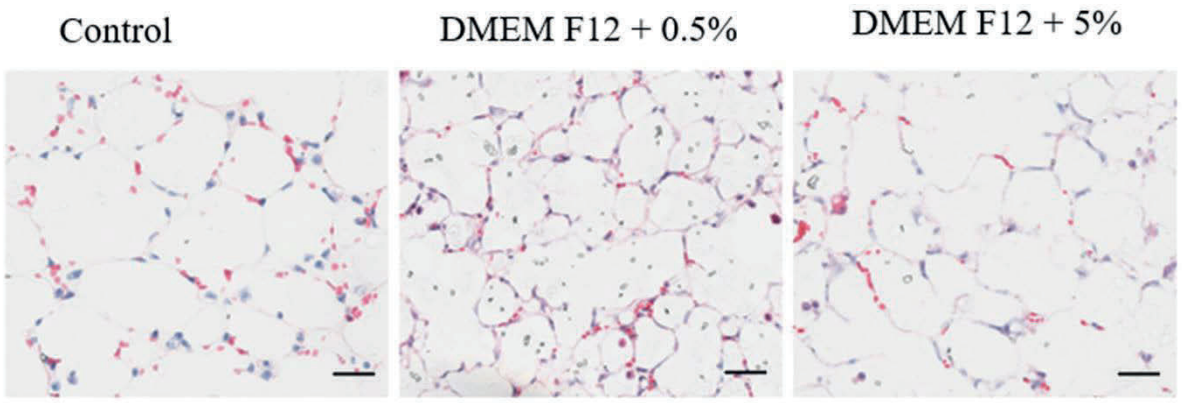


Figure 5.4. H&E staining of lung tissue slices cultured for 7 days.
Tissue structure is maintained when lung slices are cultured in DMEM/F12 media with either 0.5% or 5% FBS compared with sections fixed directly after slicing (Control). Scale bars represents 15 µm.

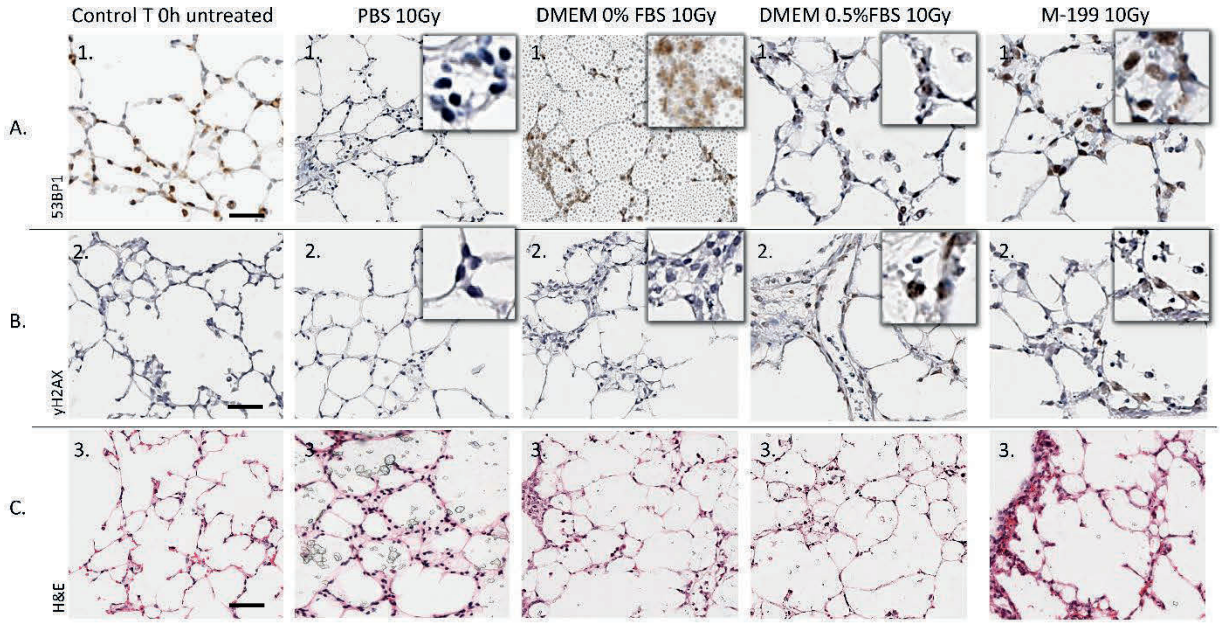


Figure 5.5. DNA damage response (DDR) following irradiation in different culture conditions.

DDR was tested in PCLS after 7 days of incubation in various conditions (PBS, M-199 and DMEM F12 with or without 0.05% FBS) by staining for 53BP1 (A) and γH2AX (B) foci compared with tissue slices fixed directly after vibratome sectioning (control). After incubation for 7 days, tissue slices were irradiated (10 Gy) and fixed two hours later. Lung tissue slices incubated in PBS or DMEM F12 without FBS had no evidence of radiation-induced 53BP1 or γH2AX foci. In contrast, tissue slices cultured in DMEM F12 with 0.5% FBS, showed clear foci for both 53BP1 and γH2AX throughout the tissue section. Tissue slices cultured in defined medium (M-199) showed staining for 53BP1 and staining for γH2AX in patches across the tissue but with no clear foci. H&E staining of tissue sections is also shown (C). Scale bars represent 15 µm. Insert images are enlarged for clarity.

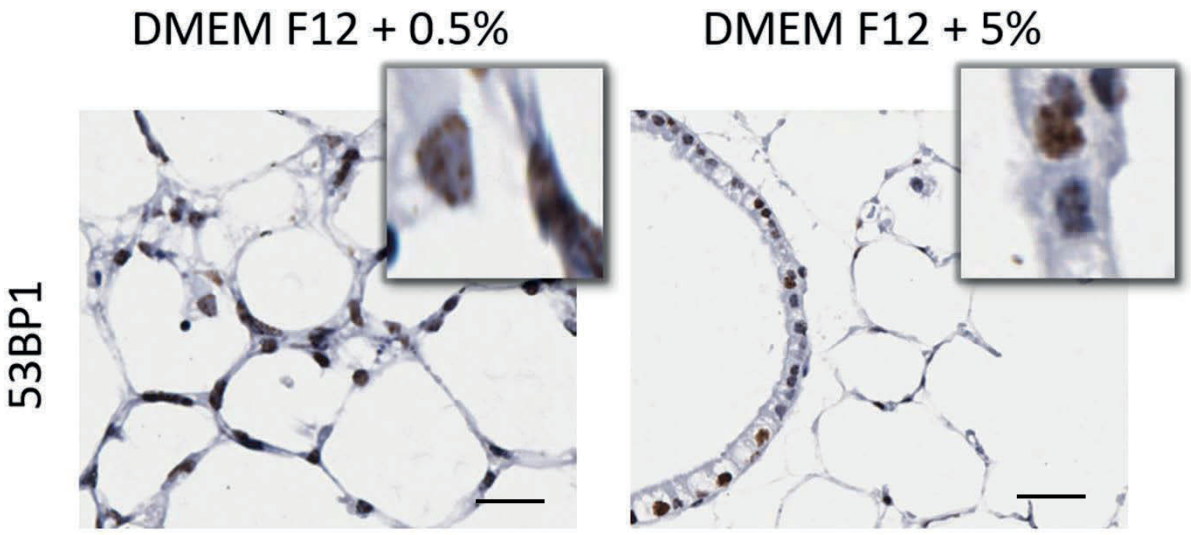


Figure 5.6. Culturing PCLS in DMEM F12 plus 0.5% or 5% FBS.
Lung tissue slices were cultured in DMEM/F12 with either 0.5% or 5% FBS for 7 days and were then irradiated (10 Gy). Both culture conditions had similar distribution of 53BP1 foci throughout the tissue sections, demonstrating an intact DDR. Scale bars represent 15 µm insert images are enlarged.

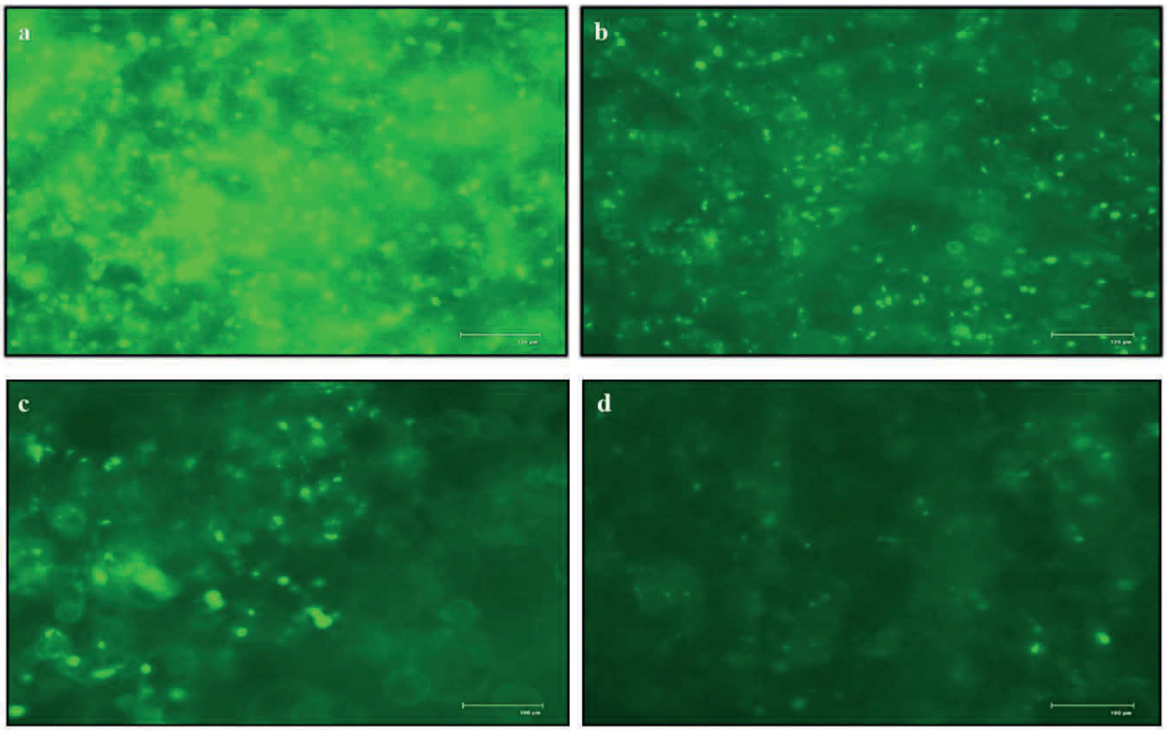


Figure 5.7. Evaluation of cell death in PCLS under different culture conditions.
Sytox green staining of lung tissue slices after 7 days in culture. (a) PBS; (b) DMEM/F12, (c) DMEM/F12 plus 0.5% FBS, (d) DMEM/F12 plus 5% FBS. Scale bars represent 100 µm

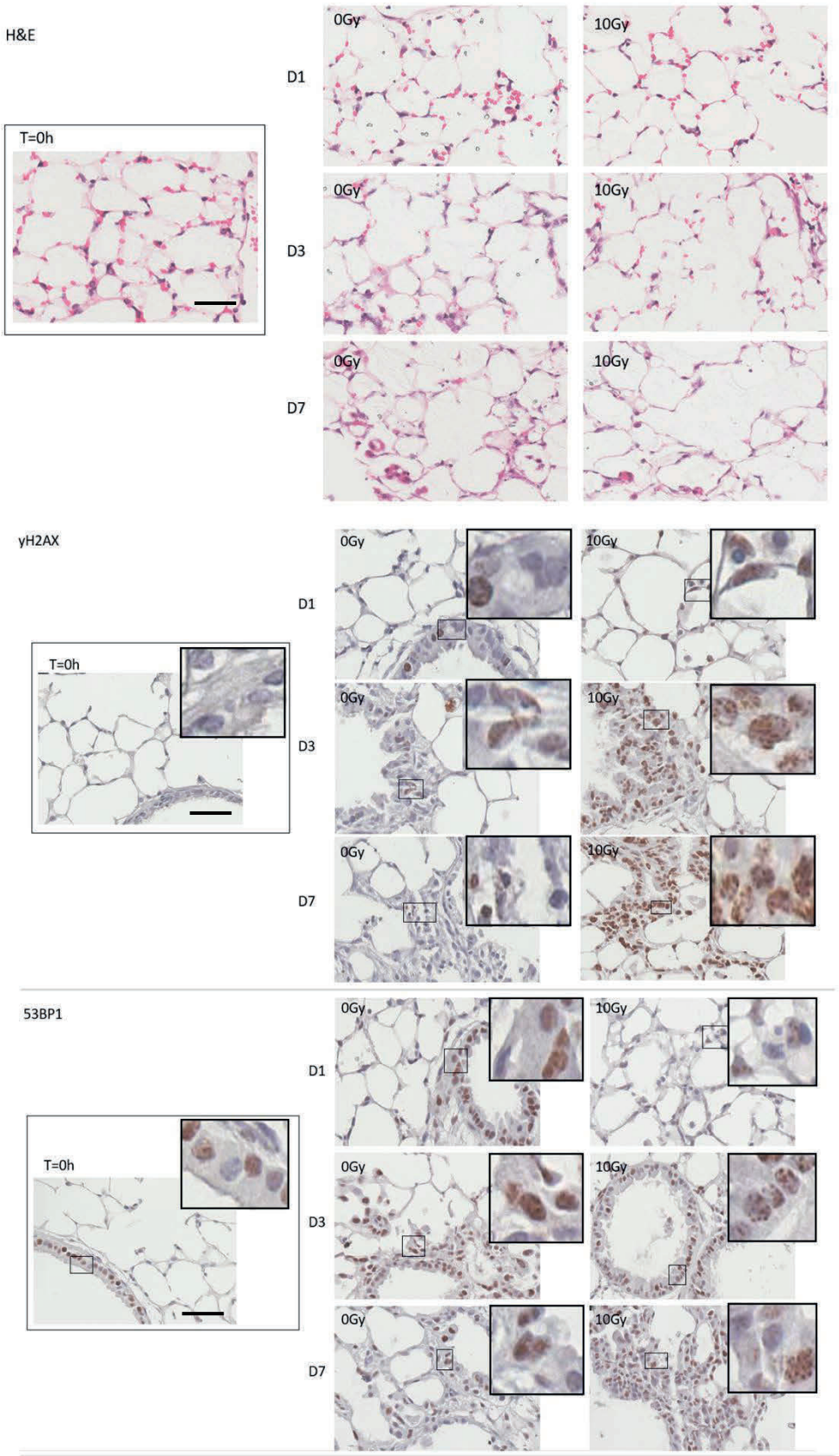


Figure 5.8. Evaluation of precision-cut lung slice structure and cellular integrity in culture throughout 7 days.
PCLS were incubated in Advanced DMEM F12 + 5% FBS for up to 7 days. Lung slices

were irradiated (10 Gy) on day 1, 3 and 7 and fixed 2 h later. Controls were slices taken and fixed immediately after vibratome sectioning (T= 0 h).
A) H&E staining of the tissues. Both γH2AX (B) and 53BP1 (C) foci are visible after irradiation throughout the 7 days of culture. There are occasional IHC positive cells in the mock irradiated samples. Alveolar structure appears intact though on day 3 there was some evidence of broncho-epithelial structural damage which was increased after 7 days in culture for both irradiated and mock irradiated PCLS. Scale bars represent 15 µm. Inset images are 2x enlarged.

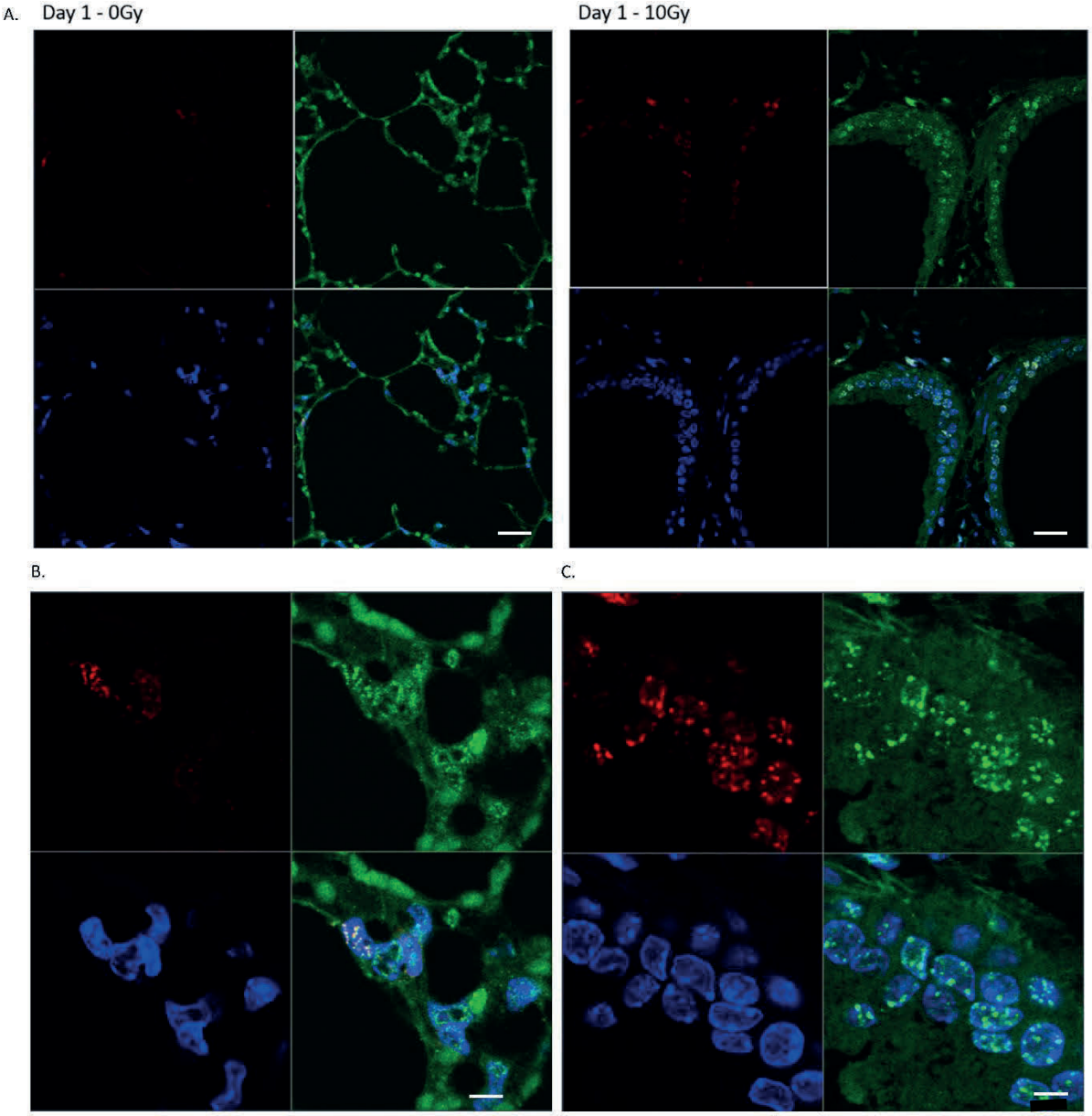


Figure 5.9. Dual staining for DDR using immunofluorescence.
Separate and composite images of staining for DNA (blue) and γH2AX (red) and 53BP1 (green) foci in lung tissue slices 2 h after irradiation (0 or 10 Gy) performed after 1 day in culture. Irradiation induces co-localised γH2AX/53BP1 foci across the tissue section, whereas occasional cells contain double stained foci in unirradiated tissue (A). Higher magnification images of unirradiated and irradiated (10 Gy) slices are shown in (B) and (C), respectively (scale bars represent 10 µm).

5.2 Evaluation of DNA Damage Response in Ex Vivo Precision-Cut Lung Slice Model Following Radiation

5.2.1 Introduction

We established that ex vivo precision-cut lung tissue slices are viable and structurally intact for up to three days, in culture. We next examined whether the DNA damage response following ionising irradiation in ex vivo lung slices was similar to the responses that are observed in in vivo studies.

Quantitation of γH2AX and 53BP1 nuclear foci are widely-used assays to measure DNA DSBs formed following irradiation (Valdiglesias et al. 2013) (Francisco and Francisco 2008). The number of γH2AX and 53BP1 nuclear foci generated after irradiation is proportional to the number of DNA DSBs (Rothkamm and Löbrich 2003) (Mariotti et al. 2013) and can be visualized by methods such as IHC and IF. As DNA DSBs are repaired over time, decreasing levels of γH2AX and 53BP1 nuclear foci can be used as a measure of DNA repair (Mariotti et al. 2013) (Rothkamm and Löbrich 2003) (Barnard, Bouffler, and Rothkamm 2013).

The number of DNA DSBs induced by IR is dose-dependent it had been estimated that around 20-40 DSBs are produced per cell per Gy (Chalmers and Carruthers 2021) (Iwamoto et al. 2014). Although DNA DSBs are highly cytotoxic, (Chalmers and Carruthers 2021) cells and tissues can tolerate exposure to certain levels of radiation by utilising highly efficient DNA damage repair pathways (see Introduction). At higher radiation doses, unrepaired DNA DSBs (residual DNA DSBs) are associated with radiation-induced toxicity (Noda 2018). In our hands, for C57BL/6 mice, a single dose of irradiation (10 Gy) to the thorax is the maximum well-tolerated dose (no significant weight loss or short or long term toxicity), with higher doses inducing weight loss, pneumonitis and fibrosis (Lourenco 2017).

We first designed experiments to measure γH2AX levels by IF in ex vivo lung slices at 2 h (for induced DNA DSBs) and 24 h (for residual DNA DSBs) following a single dose of radiation (10 Gy). We aimed to compare the results to corresponding in vivo samples that were collected 2 h and 24 h after a single dose irradiation (10 Gy) to the whole thorax. We then performed a larger experiment examining γH2AX levels at 2, 8 and 24 h following increasing doses of irradiation (0, 2, 10 Gy) in lung slices to investigate dose-dependency of DNA DSBs in this model. As a confirmation that γH2AX staining signified persistent DNA DSBs (and not other cellular responses such as apoptosis), 53BP1 foci were also measured as an additional marker of DNA DSBs. Equivalent lung samples isolated from mice treated in vivo with whole thorax irradiation (10 Gy) at similar time-points were also analysed for both DNA DSB markers.

5.2.2 Categorising γH2AX expression levels following 10 Gy irradiation

Lung slices were cultured ex vivo overnight and then irradiated (10 Gy) and then fixed in formalin 2 h or 24 h following irradiation. Samples were stained for γH2Ax using immunofluorescence and imaged using confocal Ziess 710. Corresponding lung samples from animals irradiated in vivo were stained as controls.

There is no established or widely-accepted method for determining different levels of DNA DSBs in lung tissue stained for γH2AX. Therefore, for the current work, we defined our own criteria for categorising γH2AX expression levels in lung tissue (Table 5.2, Figure 5.10A)).

Table 5.2. Categories of γH2AX staining in lung tissue

Category	γH2AX foci staining (per nucleus)
#1	none
#2	1-4 foci
#3	5-10 foci
#4	10+ (countable, distinct)
#5	uncountable

For untreated lung tissue isolated directly from mice in vivo, around 90% of cells were categorized as #1 (no γH2AX foci) and the remainder were classified as group #2 (1-4 foci) (Fig. 4.10B). Two hours after ionising radiation (10 Gy), the large majority of cells had evident γH2AX foci with the greatest proportion (35%) in group 5 with multiple overlapping, but uncountable γH2AX foci (Figure. 5.10B). Lung samples taken 24 h after in vivo irradiation and stained for γH2AX showed a high proportion of cells in categories #1 and #2, with only about 5% of cells with uncountable foci suggesting a substantial amount of DNA DSB repair, but with clear evidence of unrepaired (residual) DNS DSBs in a subpopulation of cells (Figure 5.10B). Crucially, the lung slices irradiated ex vivo showed a very similar pattern of γH2AX staining, with a broadly similar distribution between the categories with both unirradiated and irradiated samples when compared with the in vivo lung samples (Figure 5.10C), providing evidence that the induction and repair of DNA DSBs in PCLS was similar to the lung in vivo in mice exposed to whole thorax irradiation.

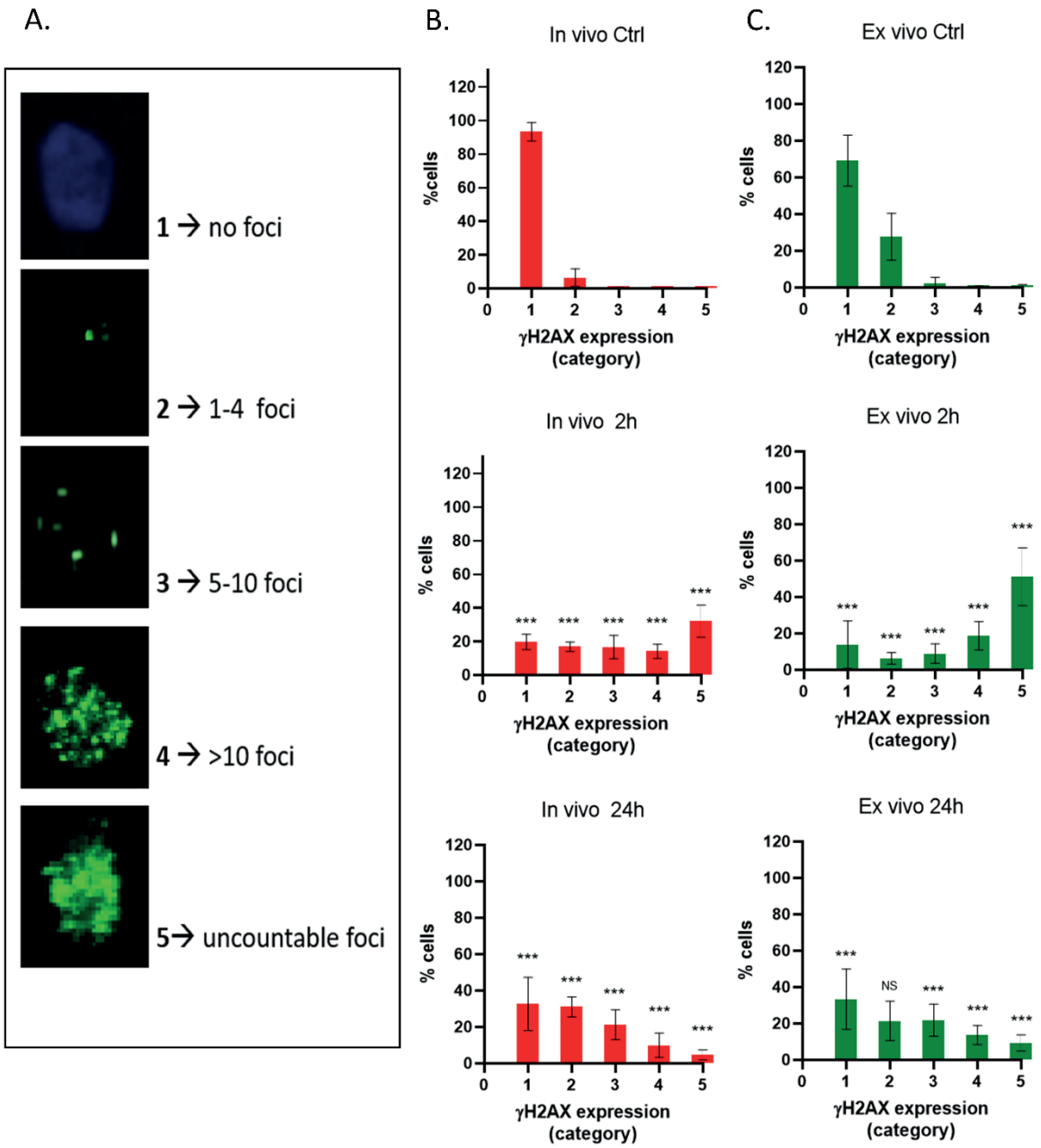


Figure 5.10. Categories of γH2AX staining following in vivo or ex vivo irradiation of lung tissue.

A. Example staining of categories of γH2AX staining. Distribution of cells/nuclei across the different staining categories 2 h or 24 h following irradiation (10 Gy) of in vivo (B) or ex vivo (C) lung tissue. Control (Ctrl unirradiated) tissue was also evaluated. Graph bars represent the average in the group (Each bar represents for in vivo n=2 and ex vivo n=3 where for each sample 5 fields of view were counted for each experiment- around 300-350 cells were counted in each field of view for in vivo and 50-80 cells were counted for each field of view ex vivo), and error bars represent ±SEM. γH2AX levels in each category at 2h or 24h were compared with the equivalent category in the controls (Ctrl) using the Mann-Whitney test. *p<0.05, **p<0.001, ***p<0.0001. (Supplementary Figure 1. Shows mock irradiated ex vivo samples. Appendix)

5.2.3 DNA Damage response in vivo and ex vivo at different doses of radiation

Precision-cut lung slices were prepared from C57BL/6 mice using the vibratome according to the established protocol; slices from each lung were fixed immediately after cutting as controls, or cultured overnight to acclimatise to the culture conditions. Tissue slides were then irradiated (0, 2 or 10 Gy) and fixed at 2, 8, and 24 h later to evaluate γH2AX and 53BP1 nuclear foci (Figure 5.11A). Corresponding lung samples from mice irradiated in vivo (10 Gy) were stained for both markers as a control for the whole experiment.

5.2.3.1 γH2AX

Lung sections from mice irradiated (10 Gy) in vivo showed that γH2AX positive cells increased from 1% ±0.5% at baseline (control) to 61 ± 3% at 2 h after radiation (Figure 5.11B). The proportion of γH2AX positive cells which decreased over time (37 ± 5 % at 8 h and 33 ± 3% at 24 h) indicating DNA repair (See Supplementary Table 2). A nested t-test was used to compare all irradiated samples to all mock irradiated samples, the mean difference was 42.4 ± 7.62% (42.38%, 95% CI. [26.04 to 58.73], p-value <0.0001).

A similar trend was seen in the ex vivo lung slices irradiated with 10 Gy: 64 ± 4% γH2AX positive cells at 2 h, declining to 31 ± 2% 24 h (Figure 5.11C). A nested t-test indicated a mean difference of 52 ± 3.82% in the proportion of γH2AX positive cells between irradiated and unirradiated sections (58.58%, 95% CI. [44.33 to 59.72], p-value<0.001).

To address whether the PCLS ex vivo model is a potential surrogate for the in vivo model we compared γH2AX positive staining in the irradiated (10 Gy) in vivo samples with the corresponding ex vivo irradiated samples (10 Gy) and saw a small but statistically significant difference [9% (8.973, 95%CI [1.290 to 16.66], p-value =0.026).

To address whether there is any dose-dependency in the ex vivo model we next examined a dose of 2 Gy, a commonly used dose fraction in the clinic (Healey and Abner 1995). Two hours following irradiation (2 Gy) there was a high proportion of γH2AX positive cells (48 ± 3%) and which decreased 31 ± 3% and 18 ± 2% after 8 h and 24 h, respectively. Notably, the fraction of cells expressing γH2AX 2 h after 2 Gy was not proportionately (i.e. 5-fold) less than 2 h after 10 Gy (48% vs 64%) indicating that in this assay system γH2AX staining is not directly dose related, although a caveat is that we are measuring the % γH2AX positive cells rather than the number of foci. It was also noteworthy that the proportion of γH2AX positive cells increased over time in unirradiated tissue slices in the ex vivo model (11 ± 1% at 24 h) perhaps suggesting that there is an increasing amount of background cellular /DNA damage in the ex vivo model (Figure 5.11C) (see Supplementary Table 3. Appendix).

Overall, across all time points assessed in the ex vivo model with 2-way ANOVA, 2 Gy and 10 Gy irradiation increased the proportion of γH2AX positive cells by 24.6% (95% CI [27.83 to 21.40], p-value <0.0001) and 44.9% (95% CI [50.1 to 39.6], p-value >0.0001), respectively, compared with unirradiated control tissue slices in culture.

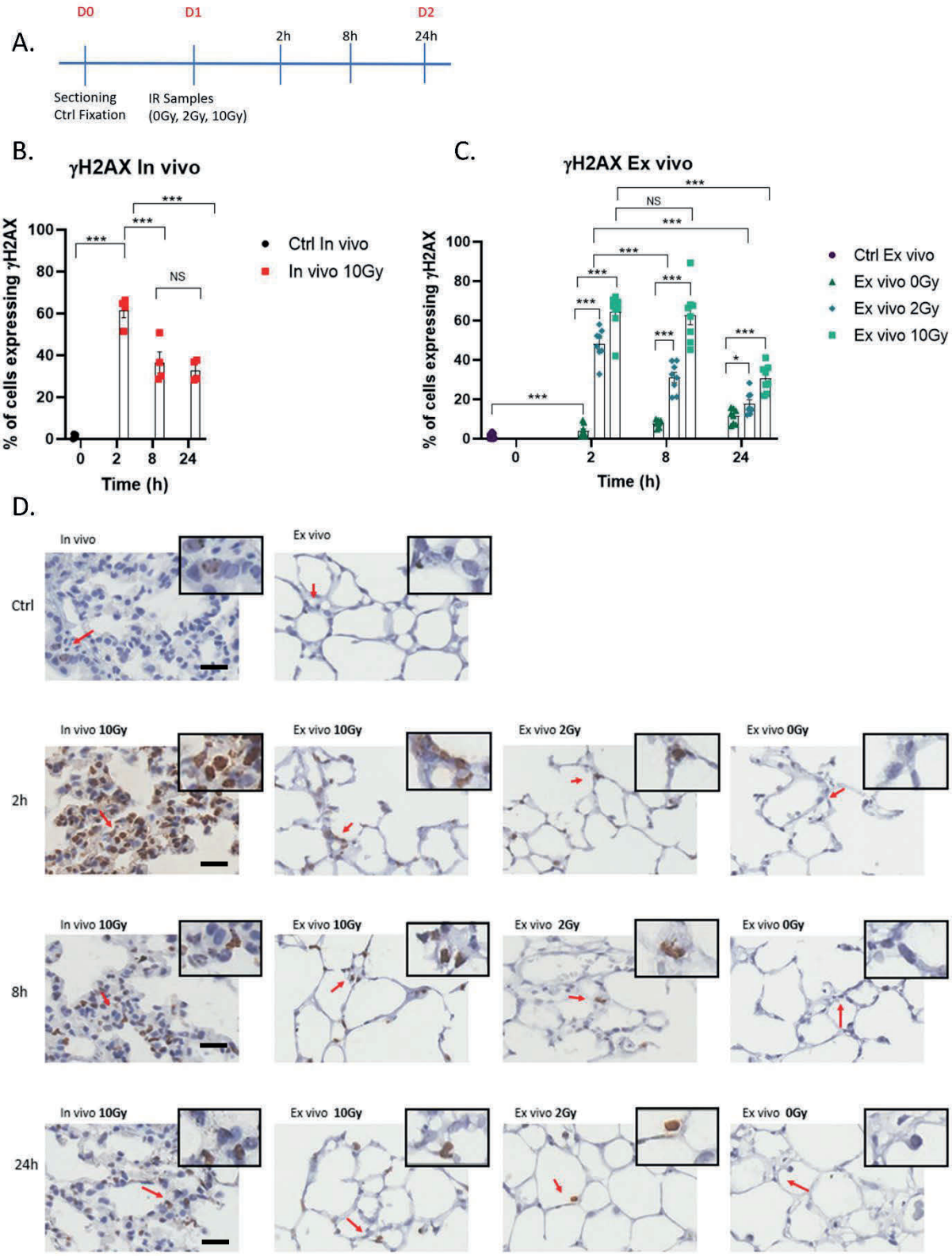


Figure 5.11. Evaluation of γH2AX levels in PCLS: The effect of dose and time.

Schematic representation of timing of PCLS preparation, irradiation and sampling. D0-2 (in red) represent nominal days. B. γH2AX positive cell counts in lung sections from mice irradiated in vivo (10Gy). C. γH2AX positive cell counts in sections from lung slices irradiated ex vivo. D. Representative images of γH2AX stained samples (scale bars represent 15 µm

insets are 2x enlarged). Graph bars represent mean n=2 in vivo 2 fields of view per lung section was analysed per experiment, 200-250 cells were scored per section. For the ex vivo each sample had a technical replicate within experiments, 2 fields of view in each section were scored for each experiment, 80-100 cells were scored per section) Error bars represent the SEM. *p<0.05, **p<0.001, ***p<0.0001 (T-test).

5.2.3.2 53BP1 as a marker of DNA damage response

In contrast to γH2AX, which is a modified (phosphorylated) form of H2AX that is only produced in response to DNA damage, 53BP1 is protein that is constitutively present in cell nucleus with undamaged DNA. Following DNA DSB damage, 53BP1 protein accumulates at the site of the DNA strand break, resulting in increased localised staining by IHC, associated with the formation of distinct foci. 53BP1 foci were counted in bronchioepithelial cells for this experiment, since the antibody was not sensitive enough to detect foci in the small nuclei of lung alveolar cells, which was previously seen in our laboratory (Lourenco 2017).

The proportion of cells staining positive for 53BP1 was generally similar to that for γH2AX (Figure 5.11 and 5.12) suggesting that γH2AX and 53BP1 both detect DNA DSBs in these assays. However, although there was reduced γH2AX staining 8 and 24 h after irradiation in vivo (compared with levels at 2 h) (Figure 5.11B), this was not apparent for similar samples stained for 53BP1 (Figure 5.12A), although there was considerable variability in the data (See Supplementary Table 4. And 5).

However, the number of 53BP1 foci may be a more sensitive measure of DNA DSBs (Schultz et al. 2000) and when the number of foci per positive nucleus was calculated, there was clear evidence of DNA repair in both the in vivo and ex vivo models (Figure 5.12C, D) with both the proportion of positive cells and the number of foci per positive cell reaching background/control levels 24 h after 2 Gy irradiation in the ex vivo model (Figure 5.12B, D).

In the in vivo model following irradiation (10 Gy) the average number of 53BP1 foci (per 53BP1 positive nucleus) increased from 3 ± 0.75 to 10 ± 1.28 at 2 h post irradiation and then decreased to 7 ± 0.75 and 4 ± 0.02 at 8 h and 24 h respectively. A similar trend was observed in the ex vivo lung slice model where the average number of foci increased from 3 ± 0.41 to 12 ±0.88 at 2 h and declined to 8 ± 0.53 at 8 h and 5 ± 0.32 foci at 24 h (See Supplementary Table 6. And 7).

A comparison between the mean number of foci/cell in in vivo and ex vivo lung tissue treated with ionising radiation (10 Gy) revealed a small but non-significant difference (mean difference was 1.09 (CI [-1,057 to 3.24], p-value=0.203) suggesting the ex vivo PCLS model could be a potential surrogate for in vivo radiation studies (See Supplementary Table 6).

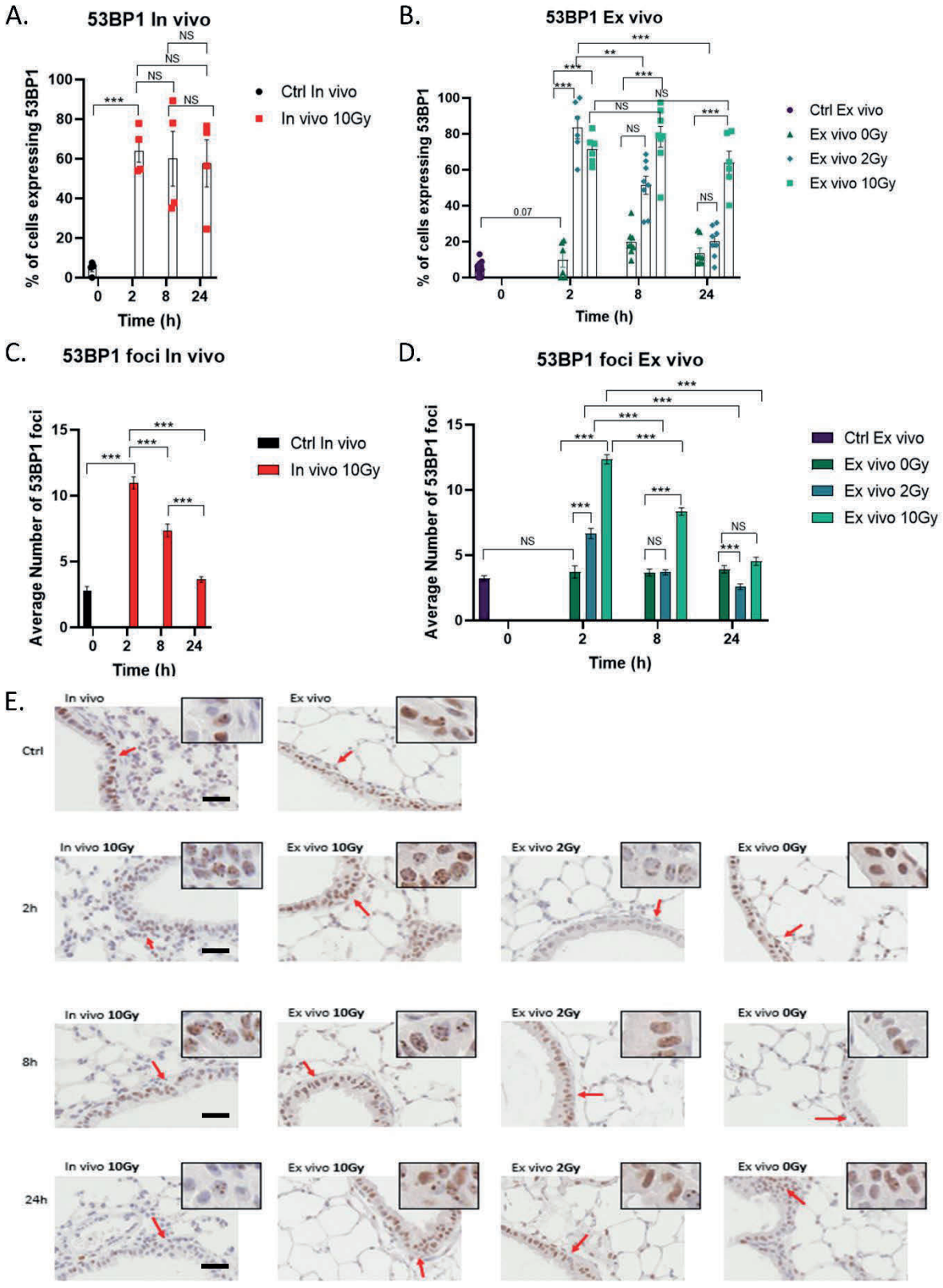


Figure 5.12. Evaluation of 53BP1 levels in PCLS: The effect of dose and time.
53BP1 staining of bronchioepithelial cells in lung sections from animals irradiated A) in vivo (0, 10 Gy) or B) PCLS ex vivo (0, 2. 10 Gy). 53BP1 foci count per nucleus in 53BP1-positive bronchioepthilial cells in lung sections from animals irradiated C) in vivo (0, 10 Gy) or D) PCLS ex vivo (0, 2. 10 Gy). E) and D) Representative images of γH2AX stained samples (scale bars represent 15 µm inset images are enlarged). Graph bars represent mean (n=2 experiments

in vivo and 2 fields of view per lung section were analysed per experiment, 100-120 cells were scored per section; for foci counting where approximately n=40 53BP1 positive cells were scored. For ex vivo, each sample had a technical replicate within experiments, 2 fields of view from each section were scored for each experiment, approximately 50-90 cells were scored per section; For foci counting where possible 40 53BP1 positive cells were score) Error bars represent the SEM and error bars ±SEM. *p<0.05, **p<0.001, ***p<0.0001 (T-test).

5.2.4 Discussion

Phosphorylation of H2AX (γH2AX) and the recruitment of 53BP1 to form foci can be detected in tissues using standard immunological methods such as IHC and IF (Valdiglesias et al. 2013) (Mariotti et al. 2013) (Barnard, Bouffler, and Rothkamm 2013) (Asaithamby and Chen 2009). It is generally accepted that the detection of foci of either of these markers in cells demonstrate the presence of DNA DSBs, whereas reduced staining and reduction in detectable foci is correlated with repair (Barnard, Bouffler, and Rothkamm 2013) (Mariotti et al. 2013) (Valdiglesias et al. 2013). In our laboratory, it was previously established for C57BL/6 mice irradiated in vivo that in the lungs both γH2AX and 53BP1 foci are at the highest levels 2 h after radiation and that these markers gradually decrease over time indicative of DNA DSB repair. In the present work, in the ex vivo precision-cut lung slice model, we demonstrated that both γH2AX and 53BP1were increased at 2 h following irradiation and they decreased over time indicating a broadly similar pattern of DNA damage and repair to that which was seen in the in vivo studies.

However, there were some differences. For example, 8 h after irradiation; the lung sections from animals irradiated in vivo (10 Gy) showed a clear reduction in γH2AX positive cells compared with the 2 h time point, which was not evident in samples from the ex vivo lung model. This may be due to the ex vivo lung slices having a slower DDR in comparison to in vivo lungs due to culturing conditions. Also, mock irradiated lung slices cultured ex vivo showed increasing levels of γH2AX staining after 8 h and 24 h, potentially indicating some

cell death as γH2AX can also be produced during apoptosis (A. Sharma, Singh, and Almasan 2012) which could have contributed to the differences between in vivo and ex vivo response to radiation-induced DNA DSBs.

Previous work by other groups has shown that number of γH2AX and 53BP1 increases approximately linearly with increasing radiation dose, consistent radiation inducing 20- 40 DNA DSBs per Gy (Chalmers and Carruthers 2021) (Iwamoto et al. 2014). However, the large majority of these studies have been performed in vitro in cell lines where the whole nucleus can be assessed with high sensitivity by IF. Previous in vivo work in mice (Rübe et al. 2008) demonstrated a linear dose response for the induction of γH2AX foci in lymphocytes by IF, at least up to 1 Gy, but only reported a level of 8 foci/Gy rather than 20-40 foci/Gy which has been reported for in vitro cell lines (Iwamoto et al. 2014). The same study also reported the kinetics of γH2AX foci reduction (i.e. DNA repair) in a range of tissues and mouse strains, including lung tissue from C57BL/6 mice where 2 Gy of radiation induced ~12 foci/nucleus which were rapidly repaired to <1 foci per nucleus within 48 h, with the large majority of repair occurring within 24 h (Rübe et al. 2008). In our study, for technical reasons, we were unable to count foci in lung alveolar cells due to the small size of the nucleus and the large size of the foci formed by the insoluble DAB stain (Figure 5.11). However, bronchioepithelial cells present with large nuclei which are amenable to foci counting (Figure 5.12E). By focusing our analysis on this cell subset, we were able to count 53BP1 foci to assess DNA damage and repair in ex vivo tissue slices, though the number of radiation-induced foci we observed after 2 Gy (~7 foci/nucleus, Figure 5.12D) was lower than reported by Rube et al. using the same dose (Rübe et al. 2008). Importantly, we also saw evidence of rapid repair at this dose, with the number of foci/cells reduced to background levels by 8 h post irradiation. There is wide body of literature describing the relationship between ionising radiation dose and DNA double strand breaks (Hall and Giaccia 2019) and we would expect a dose of 10 Gy to induce at least 5-fold

more DNA DSBs than a dose of 2 Gy (Hall and Giaccia 2019). Therefore, the IHC assays that we are using may be unsuitable for measuring radiation-induced DNA DSBs at doses higher than 2 Gy because at this dose (in vivo or ex vivo) already >40% of lung cells are positive for γH2AX and >80% positive for 53BP1 staining. Foci counting could potentially offer a more sensitive assay for DNA DSB damage with a greater dynamic range but this would require further studies to evaluate.

It is generally accepted that DNA double strand breaks are potentially lethal lesions, and the number of residual (unrepaired) DSBs is directly associated with the toxic effects of ionising radiation for both non-tumour and tumour cells (Valdiglesias et al. 2013). A single dose of 2 Gy ionising radiation is not markedly toxic to non-tumour cells. The ability of non-tumour cells to very effectively repair radiation-induced potentially lethal DNA damage between daily doses of 2 Gy is one of the underpinning principles of fractionated radiotherapy regimens used clinically to spare normal tissue from radiation-induced toxicity. In our studies, 24 h after irradiation of ex vivo tissues with 2 Gy produced near-background levels in the proportion of γH2AX- and 53BP1-positive cells, as well as in the number of 53BP1 foci/nucleus, suggesting very effective repair of radiation-induced DSBs. In contrast to 2 Gy, a radiation dose of 10 Gy is highly toxic with clonogenic survival values that are generally <1% (Brodin, Lennartsson, and Nilsson 1991) and in both the in vivo and in vitro irradiated tissues we detected a significant level of residual DNA DSBs 24 h after treatment with 10 Gy (but not 2 Gy). Taken together, the data suggest that in our ex vivo lung slice model, a radiation dose of 2 Gy may be useful for examining the impact of therapies on the *induction* of radiation-induced DNA DSB damage (in particular treatments that reduce DNA DSBs), whereas a dose of 10 Gy may be more useful for studying the impact of therapies that affect the *repair* of DNA DSBs, in particular treatments leading to increased or decreased residual DNA DSBs.

5.3 The Impact Of NU7441 On The Radiation-Induced DNA Damage Response In The Ex Vivo Precision-Cut Lung Slice Model

5.3.1 Introduction

Having evaluated the effects of radiation in the ex vivo precision-cut lung slices we next wanted to assess whether model could be used to study drug effects on tissue/cell response to radiation. In principle, radiosensitizers targeting the DDR could increase radiation-induced cell death of tumour cells and enhance the outcome of radiotherapy. However, the potential effects of DDR modulators on non-tumour tissue also need to be considered. Unrepaired DNA damage can lead to mutations which are a known cause of human cancer, and deficits in the DNA damage response lead to increased genome instability; a characteristic of many cancers (Hanahan and Weinberg 2011).

DNA-dependent protein kinase (DNA-PK), is a serine/threonine kinase which is one of the crucial proteins in the NHEJ DNA-DSB repair pathway. It belongs to the phosphatidylinositol 3-kinase-related kinase (PIKK) family which also includes ATM and ATR. DNA-PK incorporates a DNA-end-binding regulatory heterodimer (KU70/KU80) and a catalytic subunit (DNA-PKcs). Dimers of KU70 (XRCC6) and KU80 (XRCC5) bind at sites of DNA double strand breaks and recruit DNA-PKcs to form the active DNA-PK holoenzyme (Chaplin et al. 2021). Subsequent autophosphorylation of DNA-PKcs leads to a downstream signalling cascade which directs the recruitment of several proteins such as DNA ligase IV that are involved in the end joining of the damaged DNA (Figure 5.13).

Inhibition of DNA-PK activity has been linked to radio-sensitization (Mohiuddin and Kang 2019). Small molecules that bind within the ATP binding pocket of DNA-PKcs kinase domain have been shown to be effective at inhibiting DNA-PK function. Despite their selectivity and efficacy, early candidate drugs were limited by poor pharmacokinetic properties although clinical candidates have now been identified (Mohiuddin and Kang 2019)(Fok et al. 2019).

One problem that initially limited the development of DNA-PK inhibitors was their lack of selectivity towards the different PIKK family members (e.g. ATM and ATR). Later examples such as LY294002 (derivative of the flavonoid quercetin), showed that there was potential to enhance the pharmacokinetics of these molecules and to achieve more selective DNA-PK inhibition (Mohiuddin and Kang 2019). NU7441 is an ATP-competitive DNA-PKcs inhibitor (DNA-Pki) and a derivative of LY294002 (Figure 5.14) with enhanced potency for the inhibition of DNA-PK activity, which in combination with radiation inhibited DNA DSB repair for extended periods (Mohiuddin and Kang 2019). NU7441 increased the cytotoxicity of ionising radiation in a range of cancer cell lines (Mohiuddin and Kang 2019) and although the inhibitor was shown to have activity in in vivo xenograft models (Fang et al. 2021) the overall pharmacokinetic properties of the compound were not sufficiently promising and precluded future development. However, because of its in vitro potency and superior selectivity compared with earlier compounds, NU7441 (Figure 5.14) has been widely used in preclinical research. A major aim in establishing the ex vivo tissue slice model was to be able to study compound pharmacology, target biology and biomarker effects in the tissue/organ context by better utilisation of 'probe' or early development compounds with potentially poor in vivo properties (e.g. due to short plasma/tissue half-life, rapid excretion, high liver metabolism or systemic toxicity).

An early understanding of the potential in vivo effects of new therapies by using an ex vivo model could also aid in compound selection and future planning and refinement of in vivo experiments and reduce animal usage.

The aim of this chapter was to investigate the effects of NU7441, a compound with limited clinical potential, in the ex vivo precision-cut lung slice model both alone and in combination with ionising radiation to understand if the model could provide mechanistic and biological insights that could potentially guide future development of DNA-PK inhibitors.

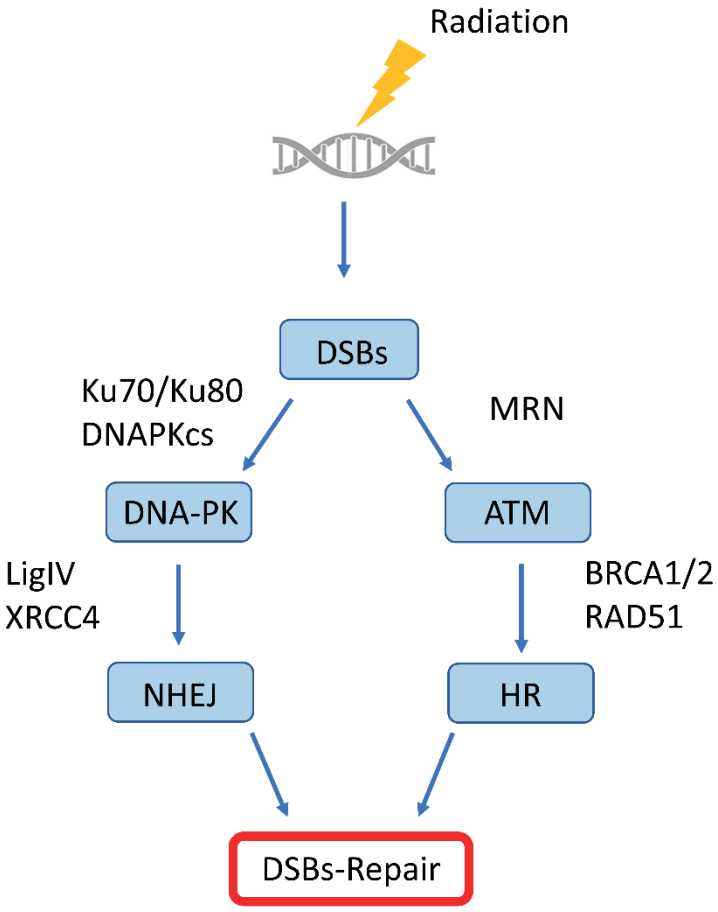


Figure 5.13. Schematic illustration of DNA DSB repair.

Radiation-induced DNA DSBs are repaired by one of two general pathways: non-homologous end-joining (NHEJ) involves the recognition of the DNA break by KU70/80, recruitment and activation of DNAPKcs, and subsequent recruitment of accessory factors such as XRCC4 that promote DNA end re-joining by DNA ligase IV (LIG4). Alternatively, in where there is a sister chromatid present (S- and G2-phases of the cell cycle) DNA DSBs can be repaired by homologous recombination. The MRN complex (MRE11-RAD50-NBS1) recognises DNA DSBs and though a series of downstream signalling that may involve ATM, resection and recombination between the damaged and undamaged DNA templates is promoted through a complex series of steps involving BRCA1/2 and RAD51.

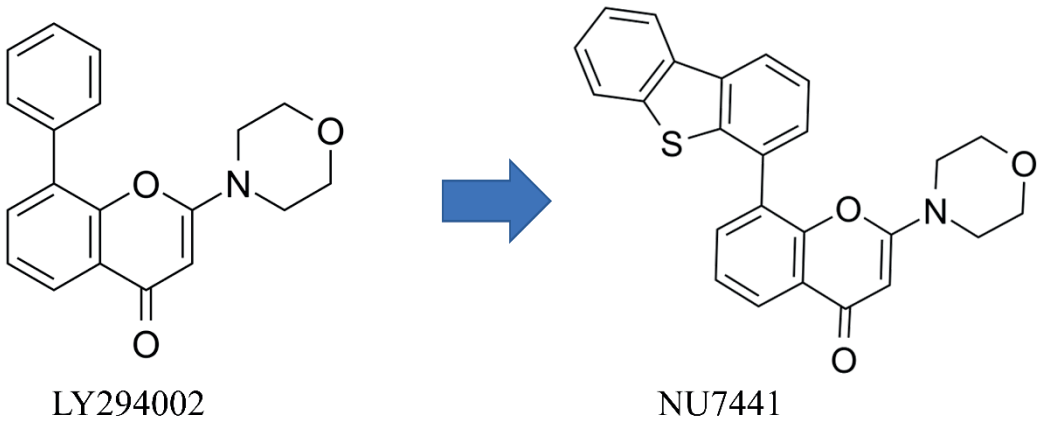


Figure 5.14. Structure of the DNA-PK inhibitors LY294002 and NU7441

From (Nickoloff et al. 2020).

5.3.2 DDR Responses In Ex Vivo Lung Tissue Slices Following Treatment With NU7441 And Radiation

5.3.2.1 Introduction

C57BL/6 lungs (n=2) were sliced using the vibratome according to the established protocol and slices from each lung (n=2 per lung) were fixed immediately as controls. Remaining lung slices were cultured as ex vivo slices overnight at 37°C to stabilize to their new environment. Tissue slices were treated with different concentrations of NU7441 (0 -10μM) and 1 h later mock-irradiated (0 Gy, control) or 10 Gy. Lung slices (n=2 from each treatment group) were fixed 24 h following irradiation. The 24 h time point was chosen to measure the effects on residual DNA DSBs, which have been reported to be associated with the increased cytotoxicity of DNA-PK inhibition in combination with radiation (Willoughby et al. 2020).

Sections were stained for γH2AX and 53BP1 using IHC to investigate the effects of NU7441 on tissue slices in the presence or absence of irradiation (10 Gy) (Figure 5.15 A).

5.3.2.2 γH2AX

There was no difference in % γH2AX positive alveolar cells when treated with NU7441 alone compared with untreated control samples (0 Gy) (mean 6.35 ±2.14%). Although, there was an increase in % γH2AX positive cell following irradiation at 10 Gy (40 ± 1.51%), there was no significant difference between the irradiated ex vivo tissue slices compared with irradiated slices receiving NU7441 in combination with radiation treatment (Figure 5.15B) (See Supplementary Table 8).

For bronchoepithelial cells a similar pattern was observed for slices that were treated with NU7441 alone. Samples treated with radiation alone (73.09±1.63%) or 1 μM NU7441 (73.09±1.88%) express a similar proportion of γH2AX positive cells. However, at higher concentrations of NU7441 there was a significant increase ($p < 0.001$, ANOVA) in the percentage of γH2AX positive cells (5 μM, 91.38±2.08% and 10 μM, 97.54±0.85%) in combination with radiation (10 Gy) compared with radiation alone (Figure 4.15C) (Supplementary Table 9).

When counting the number of foci per nucleus in γH2AX in bronchioepithelial positive cells there was evidence for dose related effect, with increasing concentrations of NU7441 associated with an increasing number of residual radiation-induced γH2AX foci per nucleus (1 μM; 4.95±0.32, 5 μM;8.45±0.42, 10 μM;12.73±0.51) (corresponding P-values provided in the figure 5.15. legend) in comparison with samples receiving 10 Gy irradiation alone (4.01 ±0.28). Interestingly, with increasing concentrations of drug alone there was a decreased number of γH2AX foci (1 μM; 3.62±0.39, 5 μM;2.95±0.51, 10 μM;2.31±0.36) in comparison to control samples in culture (0 μM, 0 Gy) (3.93±0.38) (Supplementary Table 10).

Importantly, there was a markedly higher number of foci/nuclei for samples receiving 10 μM NU7441 plus 10 Gy compared with samples treated with 10 Gy alone (+8.713±0.58 foci/cell (95% CI [7.57 to 9.86], p-value<0.001) (Figure 5.15D).

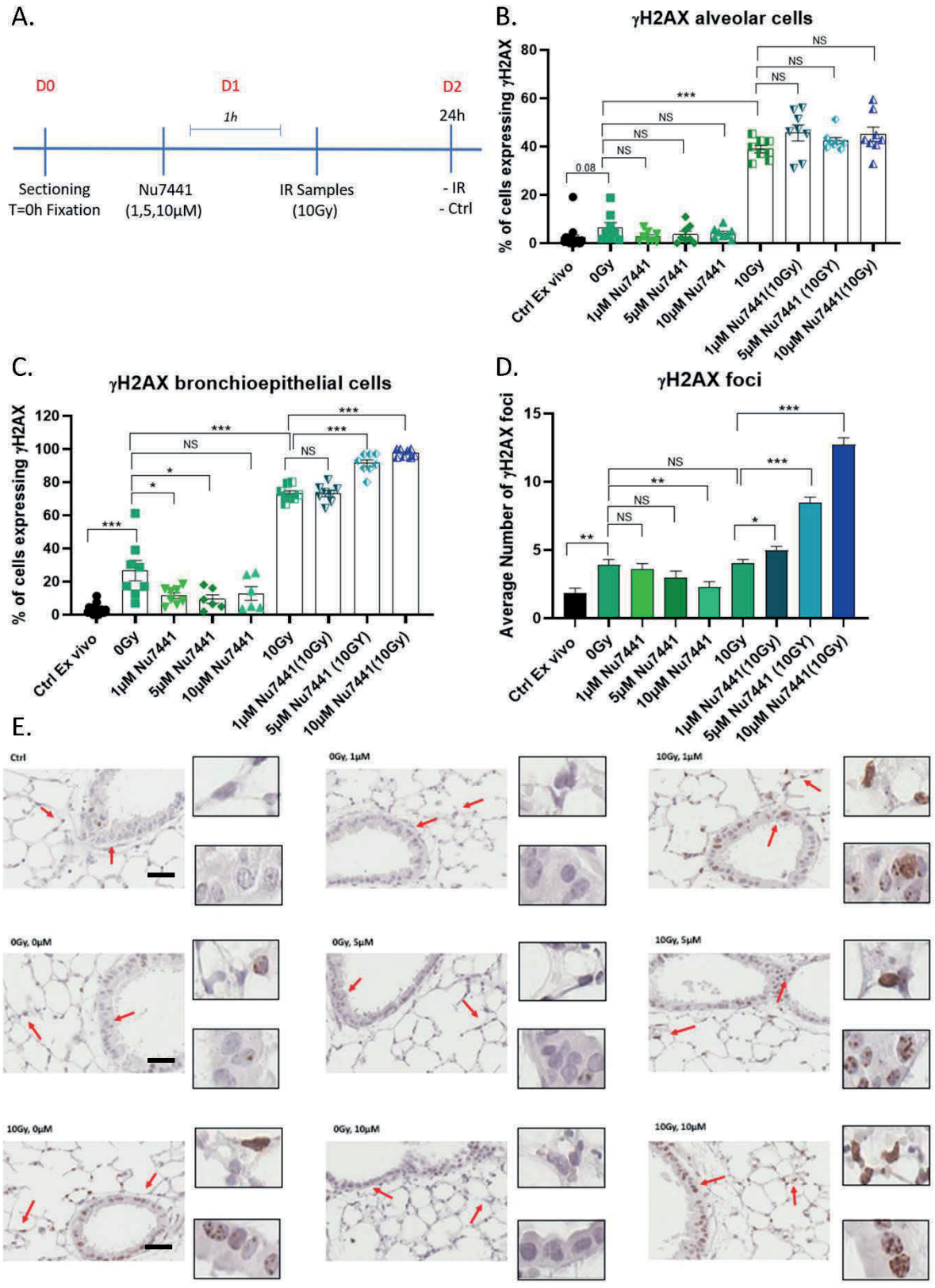


Figure 5.15. γH2AX IHC staining in ex vivo PCLS ex vivo precision-cut lung slices 24h following treatment with NU7441 and ionising radiation.

Experimental plan. B) γH2AX % positive alveolar cells. C) γH2AX % positive bronchioepithelial cells. D) Number of γH2AX foci per γH2AX foci positive bronchioepithelial cells E) Representative IHC images (scale bars represent 15µm, inserts 2X enlarged top alveolar, bottom bronchioepithelial). Graph bars represent mean (n=2, each experiment had technical replicates for each sample, and from each 2

fields of view were scored, around 100-150 of each cell type were scored, some samples were identified as not scorable due to the absence of bronchioepithelial cells. For foci counting 40 γH2AX positive cells were scored). Error bars represent the SEM. Red arrows indicate regions were enlarged images are shown. *p<0.05, **p<0.001, ***p<0.0001 (T-test).

5.3.2.3 53BP1

The proportion of cells expressing 53BP1 when treated with NU7441 alone decreased with increased concentration of the drug (1 µM; 6.95%±1.64, 5 µM; 3.78%±0.98, 10 µM; 4.85±1.03%) in comparison to the control (0 µM, 0 Gy) (13.28±0.54%), although the differences were not statistically significant (Figure 5.16A). In contrast, samples that were treated with radiation in combination with NU7441 had an increase in percentage of cells expressing 53BP1 with increased drug concentration from 60±5.11% for samples receiving 10 Gy only to 94.61±2.63% for samples receiving 10 µM of NU7441 in combination with 10 Gy (Figure 5.16B, p<0.001, ANOVA) (Supplementary Table 11).

When measuring 53BP1 foci, ex vivo slices treated with NU7441 alone had a lower number of 53BP1 foci/cell in 53BP1 positive cells (2±1.43) compared with controls (4±0.31) (Figure 5.16B). In combination with radiation, the higher concentrations of NU7441 (5 and 10 µM) led to increased 53BP1 foci/cell (Figure 5.16B)(Supplementary Table 12. Appendix).

The number of 53BP1 foci in 53BP1 positive cells for samples receiving 10 µM NU7441 with radiation (10 Gy) was significantly higher (+5.23±0.48, 95% CI [4.28 to 6.17], p-value <0.001) than samples receiving radiation alone (10 Gy) (Figure 5.16B).

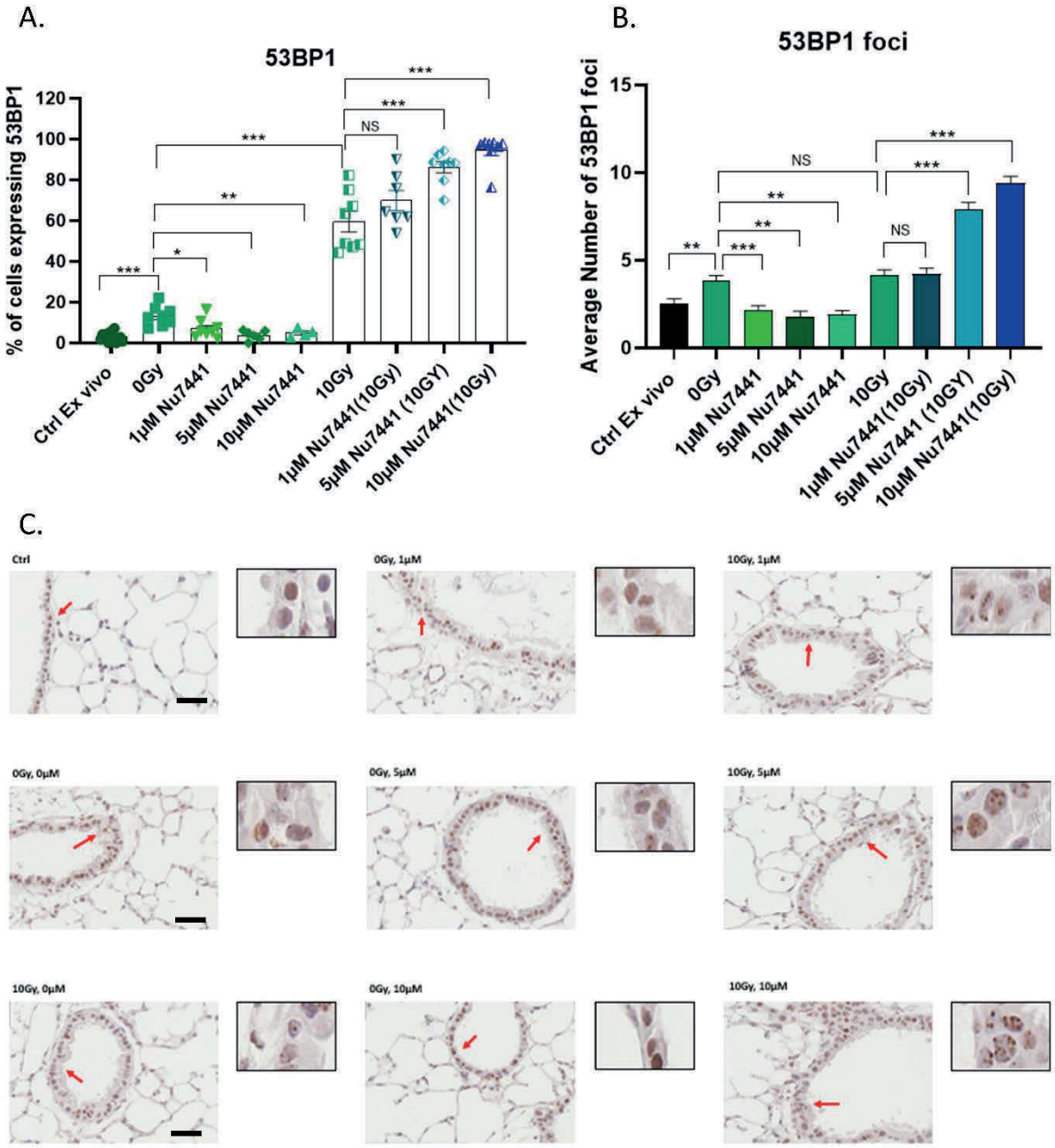


Figure 5.16. 53BP1 IHC staining in ex vivo PCLS ex vivo precision-cut lung slices 24 h following treatment with NU7441 and ionising radiation.

A) % 53BP1 positive cells count. B) 53BP1 foci/cell in 53BP1 positive cells. C) representative 53BP1 IHC images (scale bars represent 15μm, inserts 2X enlarged). Graph bars represent mean (n=2, each experiment had experimental replicates, and from each 2 fields of view were scored, around 100-150 cells were scored, some samples were identified as not scorable due to the absence of bronchioepithelial cells. For foci counting 40 γH2AX positive cells were scored when possible). Error bars represent the SEM. Red arrows indicate the enlarged regions; bronchioepithelial. *p<0.05, **p<0.001, ***p<0.0001 (T-test).

5.3.1 Cleaved Caspase 3

In an effort to develop a model in which drug toxicity could be explored, cleaved caspase 3 (CC3) an apoptotic marker, was employed as a marker to investigate whether NU7441 is toxic to the lung tissue at higher doses. Slices described in section 5.3.2.1. were stained with antibodies to CC3 (Fig. 5.17). There was a significant difference between the ex vivo tissue slice that was fixed directly following sectioning and the control sample that was left in culture for 24 h (6.91±2.18, CI [2.33 to 11.50], p-value<0.001). There was no significant difference when comparing samples that received 10 Gy or different doses of NU7441 alone with control sample in culture. There was no 9632there any significant difference between samples receiving 1 µM and 5 µM of NU7441 in combination with radiation when compared to samples receiving only 10Gy of radiation. However, there was a small but significant difference when comparing samples irradiated with 10 Gy and samples that received 10 Gy in combination with 10 µM of Nu7441 (3.83±1.71, CI [0.17 to 7.49], p-value<0.05).

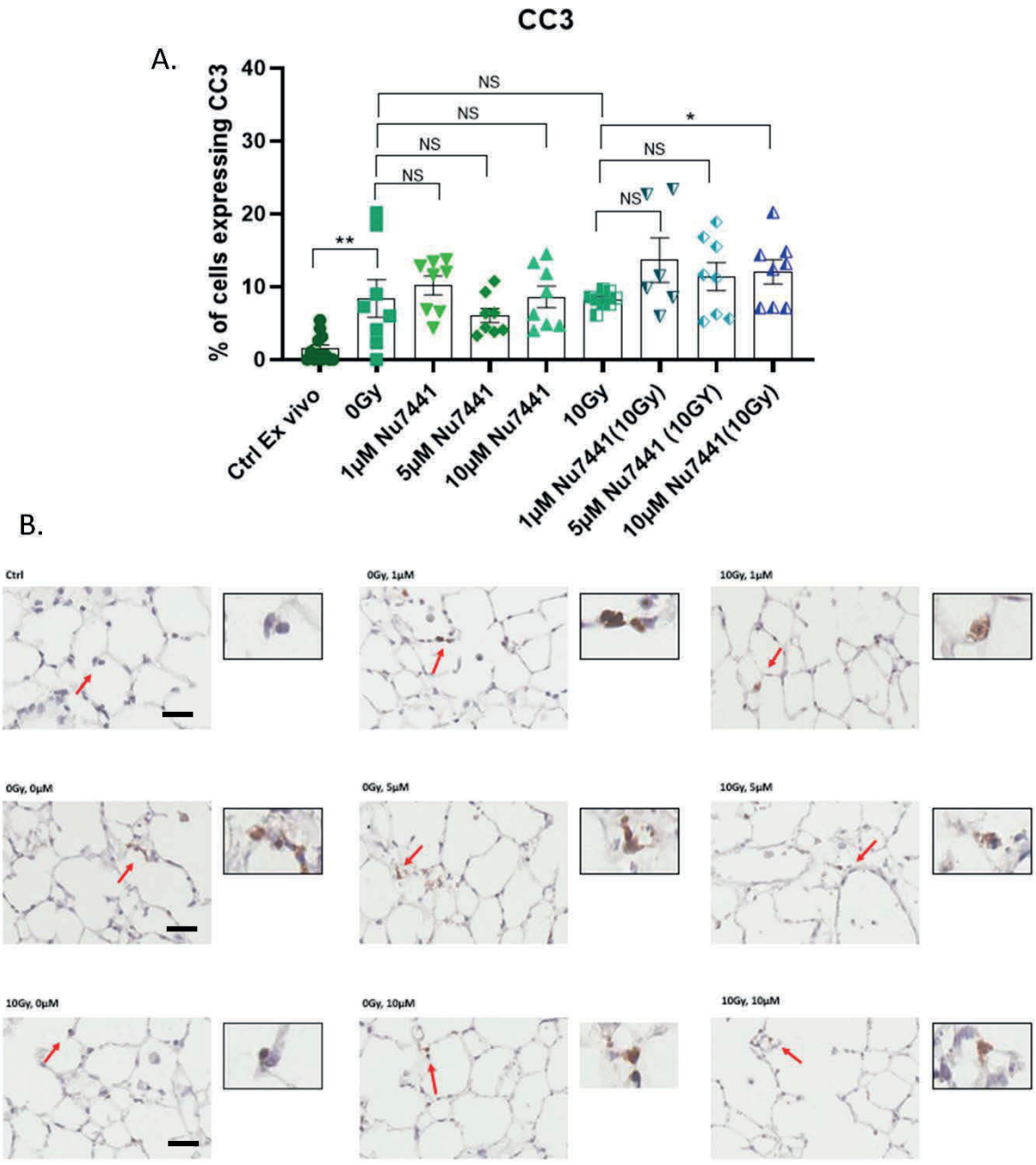


Figure 5.17. Cleaved Caspase 3 (CC3) staining to check for toxicity of the NU7441 on PCLS.

Samples from Figure 4.15 were stained with CC3 to check for evidence of apoptotic cell death caused by NU7441. There is no statistical significance between samples that were in culture with samples that received NU7441, radiation and a combination treatment except for the samples that received 10 μM of NU7441 in combination with 10 Gy.

5.3.2 Radiation induced DNA damage response in SCID mice

5.3.2.1 Introduction

Severe combined immunodeficiency (SCID) mice lack mature B and T-cells due to their inability to produce functional immunoglobulin and T-cell receptor molecules. This is related to an impaired V(D)J recombination as a result of an inactivating mutation in *PRKDC,* the gene encoding DNA-PKcs. As a consequence of loss of DNA-PK activity, SCID mice are markedly sensitive to ionising radiation.(Gerweck et al. 2006)

We next used ex vivo lung slices from SCID mice to indirectly compare the results obtained with genetic loss of DNA-PK activity compared with small molecule inhibition of DNA-PK activity using NU7441.

5.3.2.2 Experimental Design and Results

Lung slices were prepared from SCID mice (n=2) and using the vibratome. One slice from each lung was fixed directly after sectioning as a control. Remaining lung slices were culture ex vivo overnight to acclimatise, and slices (n=6) were irradiated (10 Gy) or mock-irradiated and fixed 24 h later. Tissue sections were prepared and stained by IHC for γH2AX and 53BP1.

Twenty-four hours after irradiation (10 Gy) of ex vivo lung slices from SCID mice the proportion of γH2AX positive alveolar cells was significantly increased from 4.29±1.28% (Control, 0 Gy) to. 51±2.34% (10 Gy) ($p<0.001$) (Figure 5.18B)(Supplementary Table 13. Appendix). Similarly, for bronchoepithelial cells the mean proportion of positive cells was 92±1.68 % compared with 11.96±2.49% in the control ($p<0.001$) (Figure 5.18C) (Supplementary Table 14). The number of foci in γH2AX positive cells increased from 4±0.41to 9±0.35 when following irradiation ($p<0.001$) (Figure 5.18D)(Supplementary Table 15).

Broadly similar results were obtained in bronchioepithelial cells after 53BP1 staining. (Figure 4.17). Twenty-four hours after irradiation (10 Gy) there were 75.6±3.26% 53BP1 positive cells compared to 12.32±2.21% in the mock-irradiated controls ($p<0.001$) (Fig 5.18F) and the number of foci in positively stained cells was 10±0.35 for irradiated samples compared with 3±0.22 for the unirradiated control (p,0.001) (Figure 5.18G)(Supplementary Tables 16 and 17).

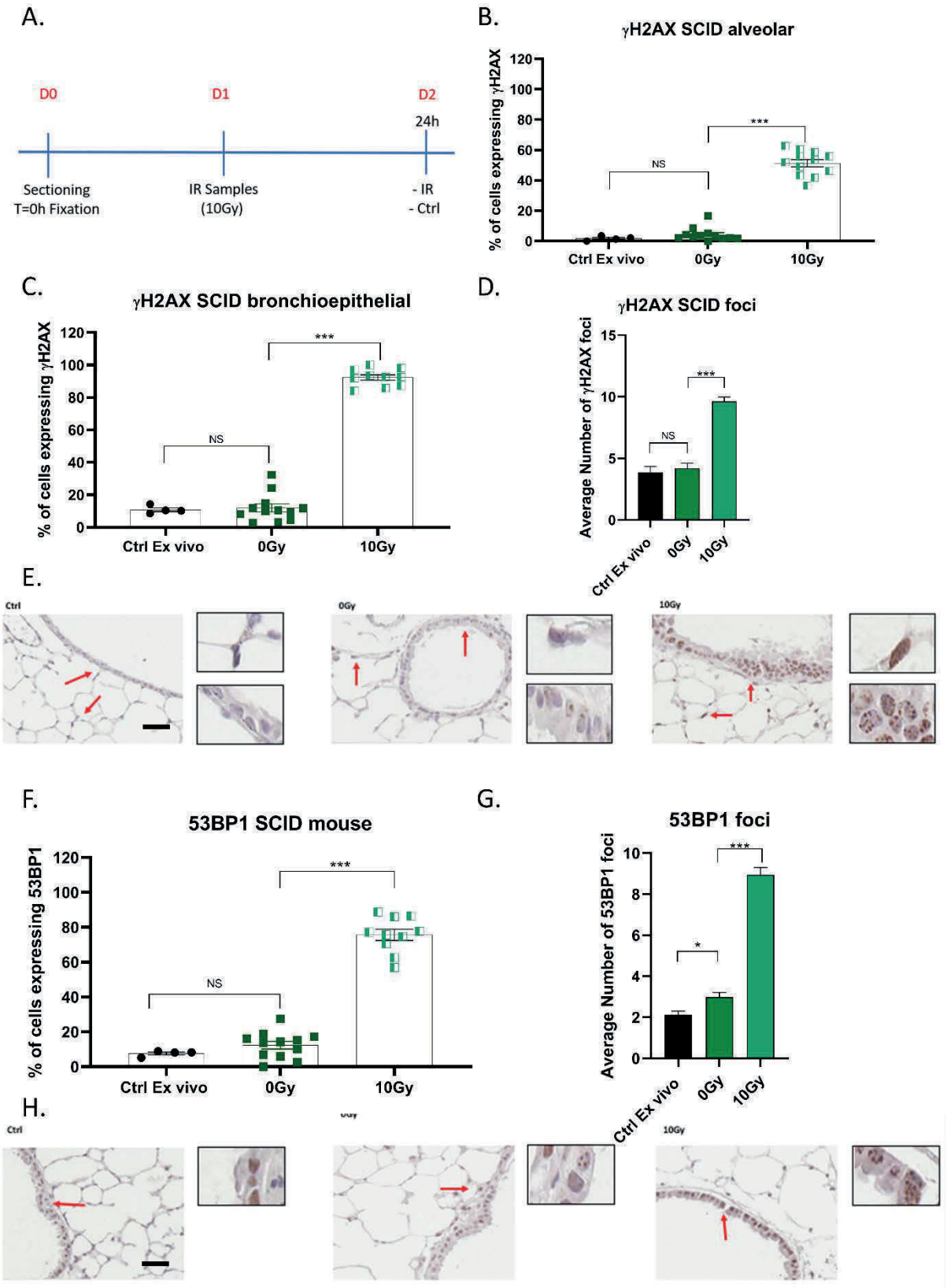


Figure 5.18. IHC staining 24h after irradiation (10 Gy) of ex vivo lung slices from SCID mice.

A) Experiment outline. B) Proportion (%) of alveolar cells expressing γH2AX. C) Proportion (%) of bronchioepithelial cells expressing γH2AX. D) Number of γH2AX foci per γH2AX positive bronchioepithelial cell nucleus. E) Representative γH2AX staining (top

insert alveolar cells bottom insert bronchioepithelial cells). F) Proportion (%) of bronchioepithelial cells expressing 53BP1. G) Number of 53BP1 foci per 53BP1positive bronchioepithelial cell. H) Representative 53BP1 IHC staining. Data represent mean values ± SEM. Ctrl (unirradiated lungs fixed immediately after euthanasia, n=12), PCLS 24 h after mock irradiation (0 Gy, n=6), PCLS 24 h after irradiation (10 Gy, n=6). 2 fields of view in each section were scored with 100-150 cells foci positive cell count and 20 cells were counted for foci for each section 10 from each field of view. (*p<0.05, **p<0.01, ***p<0.001) (T-test) (scale bars represent 15µm, inserts are enlarged).

5.3.3 Discussion

Alveolar cells make up the alveolar epithelium whose main function is gas exchange. The primary function of bronchial epithelial (bronchioepithelial) cells is to act as a protective barrier and maintain normal airway function. Following irradiation, γH2AX staining by IHC was measurable in both alveolar and bronchial epithelial cells so we were able to evaluate both types of cells separately although foci were only discernible in the bronchioepithelial cells. In contrast, 53BP1 staining by IHC was not clear in lung alveolar cells after irradiation so we could only reliably assess bronchioepithelial cells. 53BP1 staining in alveolar cells was faint and variable, as previously reported from our laboratory (Lourenco 2017) though whether this could have a biological basis or is a technical issue has not been resolved.

The presence of γH2AX or 53BP1 nuclear foci is a measure of DNA double strand breaks. When we irradiated ex vivo lung slices in the presence of NU7441 there was increased unrepaired (residual) DNA DSBs as shown by higher levels γH2AX and 53BP1 foci compared with radiation alone. There was a dose-related effect, with higher doses of NU7441 treatment leading to higher numbers of residual DNA DSBs as measured by 53BP1 or γH2AX foci. Importantly, the level of residual DNA DSBs at the highest concentration of NU7441 (10 µM) was similar to that in DNA-PK deficient SCID mice suggesting a high degree of DNA-PK inhibition by NU7441 at this concentration.

There were no significant differences in the number of positive alveolar cells expressing γH2AX between the samples receiving radiation and samples receiving a combination of NU7441 and irradiation, which was also shown in vivo in a previous study (Willoughby et al. 2020). However, when evaluating bronchioepithelial cells, there was a trend for increasing γH2AX positive cells for ex vivo lung slices treated with NU7441 in combination with radiation at the highest drug concentrations tested. The difference between alveolar and bronchial epithelial cells may in part be due to the bronchial epithelial cells having larger nuclei and consequently a larger stained area in the IHC sections. Additionally, a higher proportion of alveolar cell nuclei do not express detectable γH2AX after irradiation. As noted earlier, it is not known if this is a technical issue or biological difference, but as a result γH2AX staining of alveolar cells may be less sensitive and/or have a narrower dynamic range than IHC staining of bronchioepithelial cell nuclei.

When evaluating the number of γH2AX foci in γH2AX-positive cells, we saw a significant increase with increasing doses of NU7441 in combination with 10 Gy in comparison to radiation alone and this was also reflected in similar dose-related increase in 53BP1 foci, providing strong support to the conclusion that these foci represent unrepaired residual DNA DSBs, and that treatment with a DNA-PK inhibitor significantly inhibited DNS DSB repair.

Of note, the number of γH2AX and 53BP1 foci in positive cells for ex vivo lung slices receiving only NU441 decreased with increasing drug concentrations in comparison to vehicle treated slices. The biological basis of this observation is not understood, but could in part be due to the non-selective effects of NU7441 at higher doses, as this compound has been reported to inhibit both ATM and MTOR with IC50 values of <5 μM (Fok et al. 2019).

Studies with a chemically related DNA-PK inhibitor (NU5455) used in vivo in combination with 10 Gy thoracic irradiation in CD-1 nude mice showed very similar results to our ex vivo

lung slice model. Alveolar γH2AX positive cells increased from background to ~30-40% at 24 h post-irradiation, and this was not increased by co-treatment with NU5455 (Willoughby et al. 2020). Interestingly, in the same study, NU5455 treatment led to an increase in residual DNA damage (γH2AX positive cells) in tumour cells, suggesting a differential effect of DNA-PK inhibition in tumour versus non-tumour tissues.

Additionally, the in vivo study by Willoughby et al showed that genetic inactivation of DNA-PK in SCID mice led to markedly higher levels of γH2AX positive cells 24 h after 10 Gy irradiation compared with DNA-PK wild-type mice. We saw similar comparable effects in our studies with ex vivo lung slices from SCID mice.

Taken together, our data on irradiated ex vivo tissue slices from SCID mice or C57BL/6 mice in combination with DNA-PK inhibition are consistent with in vivo data and provide strong support for the ex vivo model as a relevant alternative to (or addition to) in vivo models of radiation-induced DNA damage and repair.

When NU7441-treated slices were tested for CC3 (an apoptotic marker), there was no significant difference between control samples (0 μM, 0 Gy), samples receiving radiation alone (10Gy), NU7441 alone at different concentrations and combination treatments. The increase in CC3 staining when NU7441 was combined with radiation suggests that DNA-PK inhibition increase cell death although the data were highly variable. In our hands, CC3 positivity in IHC sections was technically difficult to identify and score and future research should incorporate additional methods for evaluating cell death and/or cytotoxicity endpoints which might assist in planning more accurate in vivo investigations using less animals in each experiment.

In conclusion, precision-cut ex vivo lung slices could be an effective alternative model to study the pharmacodynamic effects of drugs, either alone or in combination, and would be of particular utility for drugs early in discovery process (chemical ‘probes’) that have suboptimal

in vivo pharmaceutical properties (e.g. rapid clearance, poor bioavailability, rapid metabolism etc). In addition, even for optimised drugs, the lung slice model allows much more careful control in the study of the biological effects of e.g. varying drug concentrations, duration of treatment, combination treatments and drug scheduling than in vivo studies, and this data could then be used to optimise the design of future in vivo studies.

5.4 Alveolar Type II cells

5.4.1 Introduction

Alveolar type II cells (AT2) are one of the known stem cells present in the lungs, located in the alveolar sacs (Griffin et al. 1993). AT2 cells are cuboidal progenitor stem cells that can either proliferate or differentiate into alveolar type I cells (AT1)(Griffin et al. 1993). While the thin AT1 cells are involved primarily in gas exchange, AT2 cells have several metabolic roles such as surfactant production and alveolar ion transport.(WARD and NICHOLAS 1984)

The surfactant produced by AT2 cells comprises lipoproteins (mainly dipalmitoylphosphatidylcholine) and several types of glycoproteins. Surfactant lowers the surface tension of the lung during breathing whereby hydrophilic regions bind water and hydrophobic regions interact with air. The surfactant secreted by the AT2 cells is composed of 4 different types of glycoproteins: SP-A, SP-B, SP-C and SP-D. Although SP-A is the most abundant glycoprotein in the surfactant produced by AT2, SP-C is produced solely by AT2 cells can be utilized as a cell-specific marker (Fehrenbach 2001).

The organelles present in AT2 cells are very similar to highly metabolically active cells and include a large number of mitochondria, Golgi apparatus and polyribosomes. However, a feature that distinguishes AT2 cells in the lung is the presence of apical microvilli on their

surface and lamellar bodies in the cytoplasm where the surfactant is stored (Fehrenbach 2001) (WARD and NICHOLAS 1984).

Damage to AT2 cells has been linked to a variety of lung diseases such as bronchopulmonary dysplasia and idiopathic pulmonary fibrosis which has been hypothesized to be associated with aberrant communication between AT2 cells, other epithelial cells, basement membrane and interstitial cells underneath the basal membrane (Sucre et al. 2018) (Griffin et al. 1993).

In this part of the work, investigated whether the ex vivo precision-cut lung slices could be used to study AT2 cells within a tissue context, and in addition whether the effects of radiation could be evaluated in cell subtypes (AT2 cells).

5.4.2 Evaluation Of AT2 Cells In The Ex Vivo Tissue Slice Model

The difficulty of growing primary AT2 cells has been a major obstacle in researching these progenitor cells. Numerous groups have attempted to retain AT2 cell differentiation in culture by co-culturing or creating 3D technique (Gonzales et al. 2001)(Dobbs 1990)(Sucre et al. 2018). However, AT2 cells cease producing SPC after a few days in culture making them difficult to identify, track and study further (Gonzales et al. 2001) (Dobbs 1990) (Sucre et al. 2018).

Our first aim was to determine whether AT2 cells could be detected and remain viable in the ex vivo lung slices model.

SPC a marker of AT2 cells) staining was performed on freshly cut ex vivo lung slices from C57BL/6 mice [from Figure 5.8.]. SPC staining was seen in individual cells within the alveolar sacs but not in the bronchioepithelial structures for lung slices fixed directly after slicing (day 0), suggesting that the antibody binds selectively to AT2 cells (Figure 5.19A). After 1 day in culture, with or without radiation, similar staining was seen in ex vivo tissue slices (Figure

5.19B). However, on after 3 days in culture, SPC staining was still apparent in the alveolar sacs, but SPC was also detectable in bronchipepithelial structures (with or without radiation) (Figure 5.19B). Remarkably after 7 days in culture, SPC staining was restricted to bonchioepithelial cells with no SPC staining seen in the alveolar sacs (Figure 5.19B).

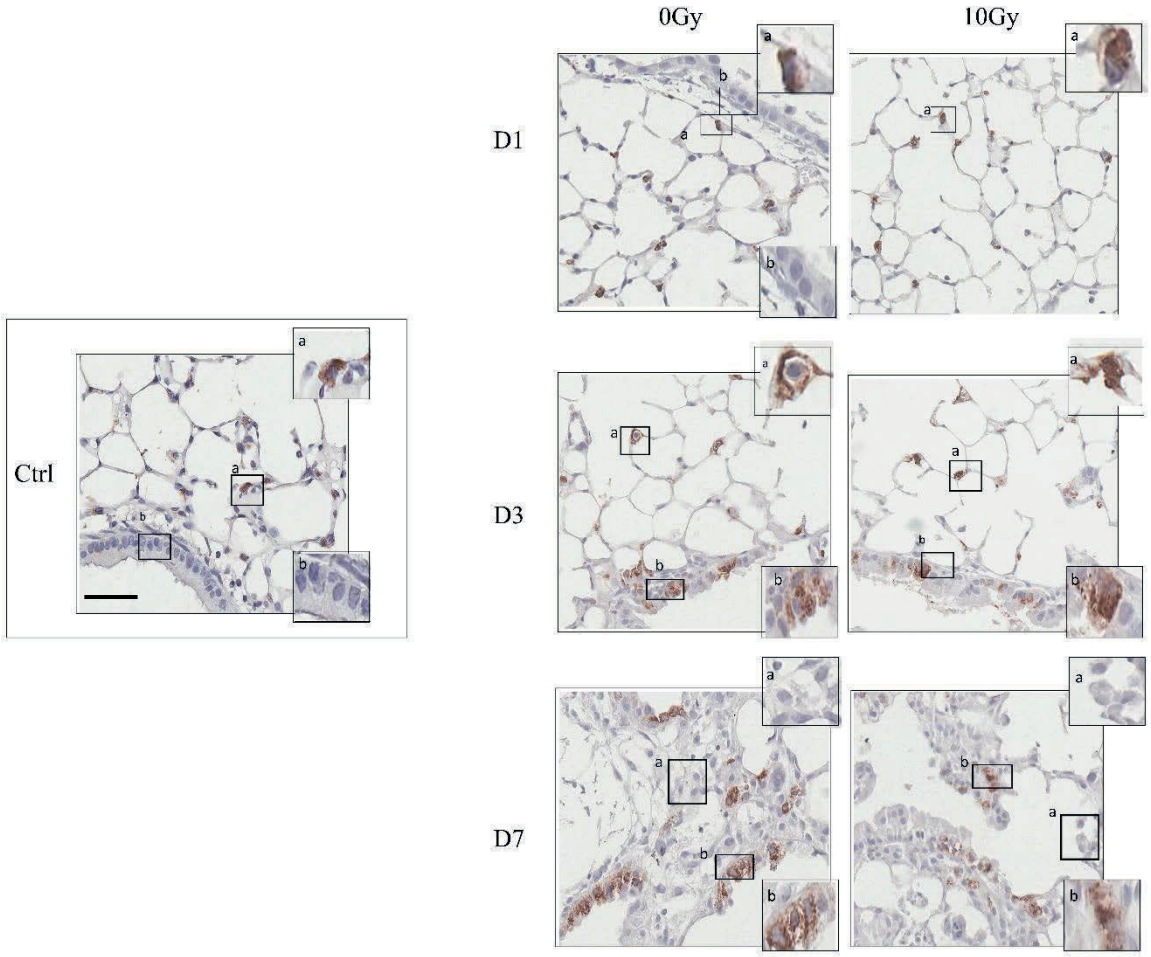


Figure 5.19. SPC expression in ex vivo precision-cut lung slices treated with (10 Gy) or without (0 Gy) irradiation.SPC staining by IHC of control freshly cut lung slices (A) or ex vivo lung slices (B) cultured for 1 (D1), 3 (D3) or 7 (D7) days after irradiation (10 Gy) or mock-irradiation (0 Gy) on D1, D3, D7 (n=3) (scale bars represent 15 µm, inserts are enlarged)

a = alveolar regions, b = bronchioepithelial regions

5.4.3 DDR in AT2 Cells in Precision-Cut Lung Slices

The ex vivo lung slice model gives the opportunity to study DDR in specific cell populations within the tissue context. A previous study (Griffin et al. 1993) showed that AT2 cells co-cultured with fibroblasts impacted collagen IV production. Therefore, we hypothesized that AT2 cells might indirectly be involved in the long-term side effect of lung fibrosis following thoracic irradiation and potentially had a distinct pattern of DNA damage response/repair.

Samples [from Figure 5.10.] were co-stained with SPC and γH2AX to indirectly compare the effect of irradiation in vivo and ex vivo (Figure 5.20). For the in vivo model, we observed AT2 cells appeared to have fewer γH2AX foci in comparison to other cells following 10 Gy at 2 and 24 h (Figure 5.20C, D). We applied a cut-off of 10 foci/cell to categorise SPC-positive cells as having high/low levels of γH2AX foci (Figure 5.20A) and showed that only 20% of SPC-positive cells expressed high levels of γH2AX foci 2 h after 10 Gy which fell to near background levels at 24 h (Figure 5.20A).

For the irradiated ex vivo tissue slices although statistically not significant, approximately 10% of the SPC-positive cells had more than 10 foci at 2 h IR that, in contrast to the in vivo lung samples, rose to approximately 25% 24 h after irradiation (Figure 5.20B).

Because of the low levels of initial DNA damage (γH2AX foci 2 h after irradiation, Figure 5.19C), we hypothesized that AT2 cells could be resistant to DNA damage induction, possess defensive mechanisms, or repair DNA damage more rapidly than other cells. Consequently, we examined AT2 cells in irradiated ex vivo lung slices from DNA repair defective SCID mice. 24 h after irradiation (10 Gy), 50% of AT2 cells had more than 10 γH2AX foci in the SCID mice ex vivo lung slices (Figure 5.21), suggesting that in DNA-PK wild-type mice (Figure 5.19), the lower levels of DNA DSBs in AT2 cells may be due to increased/rapid DNA DSB repair.

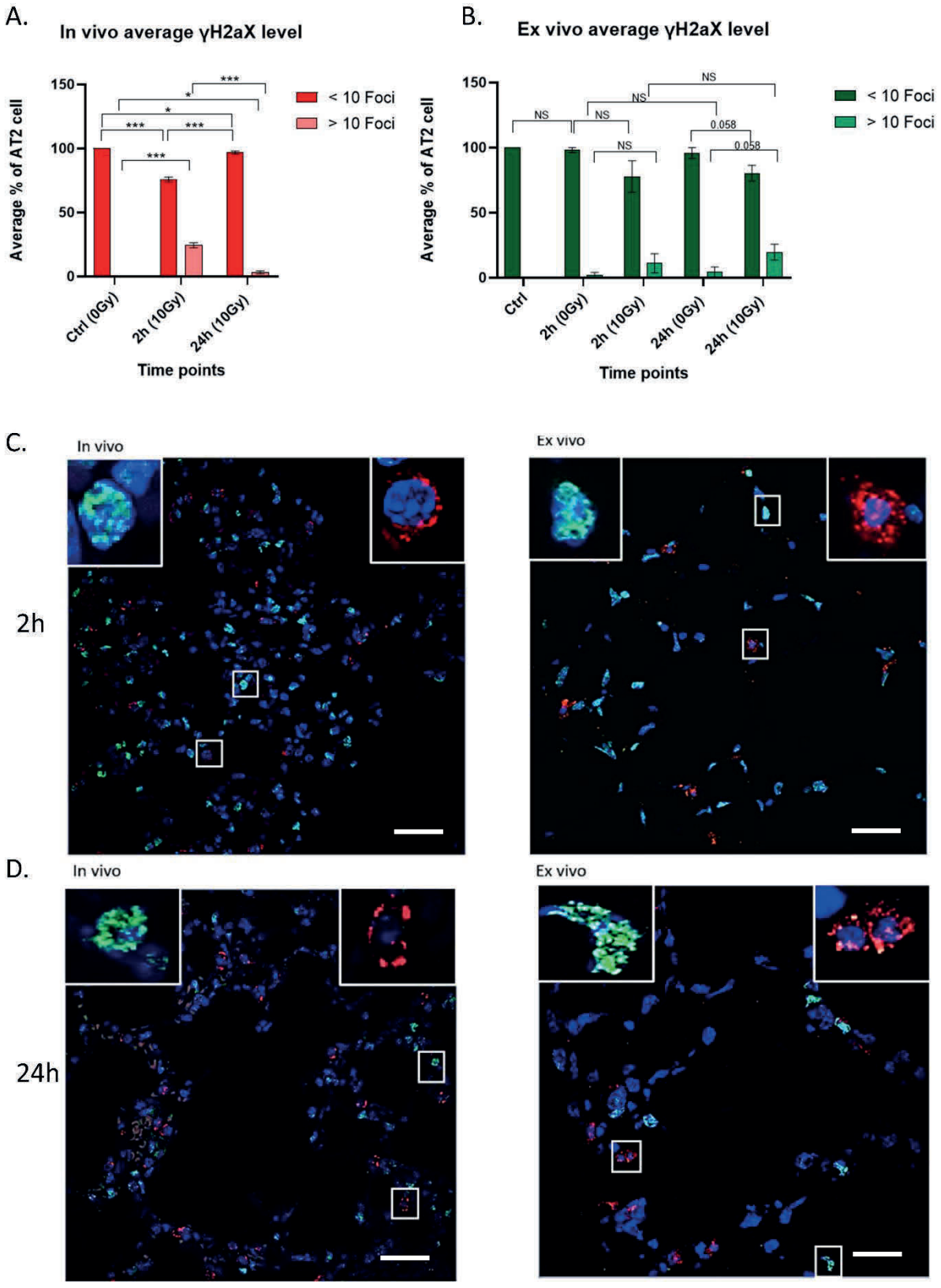


Figure 5.20. γH2AX staining by IF in SPC+ cells following irradiation (10 Gy). Samples were stained by IF for SPC (red) and γH2AX (green) and the number of γH2AX foci determined in SPC-positive cells (n=2 in vivo 120-190 AT2 cells were scored for each sample, n=2 for ex vivo 11-41 AT2 cells were scored for each sample). SPC-positive cells were

categorised as having high (≥10 foci) or low (<10 foci) levels of γH2AX staining. In comparison to other cells SPC-positive cells seem to be less sensitive to radiation.
Lung samples from control mice (0 Gy) or mice irradiated in vivo (0 or 10 Gy) and samples prepared 2 or 24 h later. Data are normalised to control mice (100%). B. Lung slices cultured ex vivo and irradiated (0 or 10 Gy) and samples prepared 2 and 24 h later. C. Representative IF staining 2 h after in vivo or ex vivo irradiation. D. Representative IF staining 24 h after in vivo or ex vivo irradiation. SPC positive cells had fewer γH2AX foci than SPC-negative cells (white boxes). Scale bars represents 10 µm, inserts are 2X enlarged) (*p<0.05, **p<0.01, ***p<0.001) (T-test)

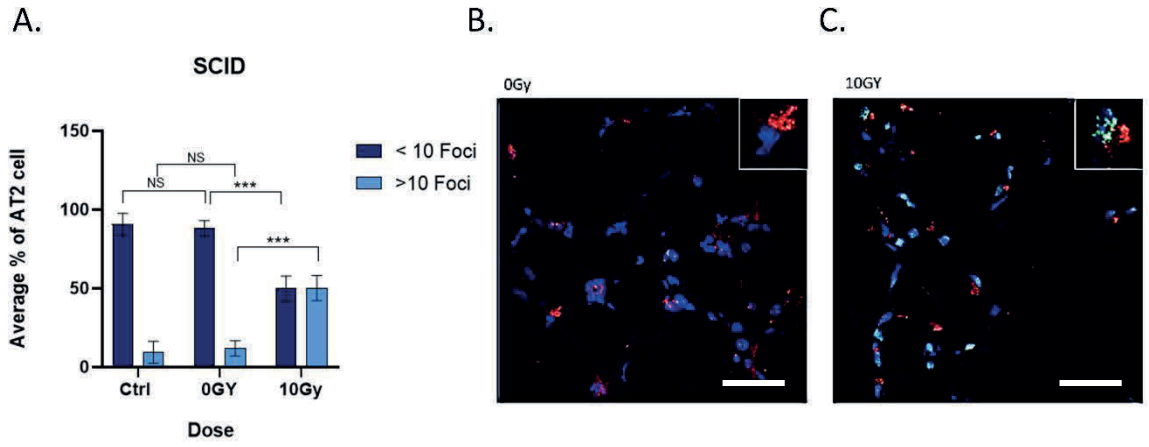


Figure 5.21. γH2AX staining by IF in SPC+ cells following irradiation (10 Gy) of ex vivo lung slices from SCID mice.
Samples were stained by IF for SPC (red) and γH2AX (green) and the number of γH2AX foci determined in SPC-positive cells (around 12-35 AT2 cells were scored). SPC-positive cells were categorised as having high (>10 foci) or low (≤10 foci) levels of γH2AX staining.
Lung slices were fixed immediately after slicing (control) or cultured ex vivo. Ex vivo slices were irradiated (10 Gy) and stained 24 h later. B. Representative IF images.
Scale bars represents 10 µm and inserts are 2X enlarged. (*p<0.05, **p<0.01, ***p<0.001) (T-test).

5.4.4 Discussion

AT2 cells (visualized by SPC staining) were detected in ex vivo precision-cut lung slices after 1 day in culture with or without radiation. SPC staining was gradually reduced in cells within alveolar sacs and emerged within cells of bronchioepithelial structures after 3 days, and particularly after 7 days in culture. We reasoned that this may be because AT2 cells are progenitor stem cells that may develop into AT1 cells – perhaps in response to the tissue injury caused by the vibratome. Additionally, the appearance of SPC staining in bronchioepithelial structures could be explained by the existence of multipotent stem cells at the broncho-alveolar duct junctions that have the capacity to differentiate into bronchioepithelial or AT2 cells (Q. Liu et al. 2019) and are responding to the deficiency of AT2 cells as they in turn develop into AT1 cells. The findings clearly show that this model is viable for examining the biological alterations and involvement of various stem/progenitor cells following injury on day 3 and beyond, as we are creating injury using the vibratome.

AT2 cells have proven to be an intriguing cell type to research and comprehend. It plays an important role in repairing alveolar damage, and according to our hypothesis, there may be a special paracrine signaling between these cells, with the disappearance of one cell due to either differentiation or due to injury, and triggering the differentiation of another. Future experiments in this area could be the use of RNA-sequencing and RNA-scope on cultured tissue slices to better understand what is happening. It would also be fascinating to use live-cell microscopy to investigate paracrine signaling and which molecules are involved.

Notably, when C57BL/6 mice were irradiated in vivo and ex vivo, the majority of AT2 cells had fewer γH2AX foci than other cells and our preliminary data indirectly comparing wild-type and DNA-PK deficient mice suggest that the reduced levels of γH2AX foci was due to increased and fast DNA DSB repair. As a result, we postulated that AT2 cells primarily rely on NHEJ controlled by the DNA-PK to repair DNA damage, which is a quick but error-prone

repair pathway. This in turn, suggests that these cells may be susceptible to mutations that could contribute to the formation of adenocarcinoma, as several articles have indicated (Sainz de Aja, Dost, and Kim 2021)(Lin et al. 2012)(Jacks and Keating 2020).

According to prior study conducted by (Griffin et al. 1993), when they co-cultured fibroblasts and AT2 cells, they showed that AT2 cells influenced fibroblasts to generate more collagen IV, whereas macrophages had no effect. In vivo, the basal membrane separates the AT2 cells from the fibroblasts anatomically and under normal conditions. However, it is known that radiation causes damage to the basal membrane, potentially exposing AT2 cells to fibroblasts, resulting in a negative influence of the AT2 cells, which in turn might lead to fibrosis in the long term. As a result, we hypothesized that AT2 cells together with other factors as the recruited immune cells may play a role in the development of fibrosis following radiation.

These hypotheses have to be examined further by evaluating the number of DSBs generated in AT2 cells post radiation. This could be accomplished by isolating these cells and irradiating them in vitro. In this study we sought to develop a methodology for single cell suspension that yielded around 70-90% viability and detected the presence of AT2 cells with a western blot (see Supplementary Figure 3.). In future a Percoll cell separation system could be optimized to obtain an enriched/purified AT2 cell population.

Furthermore, using live cell microscopy and multiple staining protocols (Akram et al. 2019), the effect of AT2 cells on fibroblasts following radiation, and whether it affects collagen IV formation could be studied. Additionally, with this method the effects of AT2 cells on other cell types as AT1, macrophages could be evaluated.

Although beyond the scope of this thesis, other cell types could be evaluated on the PCLS model to identify critically damaged cells that could contribute to radiation related side effects.

As well as utilising DDR inhibitors (ATM, ATR, PARP and DNA-PK) in addition to lung slices from mutant strains with loss of function mutations (*ATM, PARP1*).

6 General Discussion

In this work, we wanted to investigate whether ex vivo precision-cut lung slices could be useful alternatives for in vivo models, and in particular if they might be useful for studies involving radiation and drug effects.

We employed a straightforward procedure involving tissue slicing using a vibratome, and ex vivo culture conditions, with the tissue slice maintained at the air-medium interface, and with culture medium that could maintain tissue viability for at least seven days. We defined important parameters within the methodology by ensuring slicing was completed within 45 min of euthanasia/dissection, and the slices were immediately placed into the wells of pre-prepared tissue culture plates. Preparation of the culture plates and wells a day prior to use was critical since the PTFE filter employed became wetted only gradually when exposed to liquid media. To minimize discrepancies between various lung slices, the filter was put in 6-well plates with 1.65 mL medium and allowed to equilibrate overnight, when we placed the tissue on the filter more medium was added according to tissue size (up to 2 mL) (Supplementary table 1). As previously reported by others the use of filter is essential since it preserves the anatomy of the lungs (Davies et al. 2015). We chose PTFE filters from Millipore, as they matched our requirements while being transparent and allowing the potential for live cell microscopy and IF studies in the future.

A critical aspect of the methodology was medium selection since we sought to construct a basic, reproducible model with a well-defined medium to minimize the potential impact of

medium components in future studies. As a result, we chose M199 (Medium 199, originally developed as a completely defined medium for the culture of primary explants) and Advanced DMEM F12 (the standard medium used in our laboratory for growing a wide range of tumour and non-tumour human and murine cell lines, including primary cells). We aimed initially to omit serum to minimize batch differences and potential confounds and variability due to the different species of origin (bovine serum versus murine tissue), but also to give us greater control of tissue microenvironment. However, in order to reduce cell death during ex vivo culture, we found 5% FBS added to medium resulted in the least amount of apoptosis, and the DMEM F12 medium sustained a higher degree of viability than M199. Future work will be required to determine whether each of the individual components of DMEM F12 are necessary at the concentrations present. The presence of serum in the medium may cause fibroblasts to outgrow other cells, influencing the results. For future studies specific stains could be used to examination how fibroblast numbers and activation status change over the course of 7 days in culture, as well as the impact of other cell types (e.g. alveolar macrophages).

We also found that changing the medium every day was critical to compensate for evaporation that could lead to cell stress which we found to be evident under bright field microscopy when media was not changed. We also developed a fixation approach that enables us to determine which side of the lung was on the filter, allowing us to identify the potentially hypoxic side of the tissue slice and focus our studies on the non-hypoxic tissue in order to minimize any potential confounding effects of hypoxia that are known to affect responses to radiation (Davies et al. 2015).

Although the tissue slices were viable for at least seven days in culture, we focused our studies within the first three days, because at that point we saw clear histological evidence of bronchioepithelial changes that were likely a biological response to the extensive tissue damage induced by the slicing protocol. Further evidence for this was found when we stained cells for

the AT2-specific marker, SPC, which showed evidence of staining in bronchioepithelial cells after 3 days in culture, and which we hypothesized was due to bronchioalveolar duct stem cells differentiating into AT2 cells, as a response to loss of SPC-expressing AT2 cells that we observed in the alveolar ducts.

By analyzing histological markers of DNA double strand breaks, such as γH2AX and 53BP1, we were able to demonstrate that the radiation response in the ex vivo tissue slice model was generally comparable with in vivo studies. From a technical perspective, it was not possible to measure distinct γH2AX or 53BP1 foci in the most prevalent lung cell type (alveolar cells) by standard IHC with a DAB chromogen. The small size of alveolar cell nuclei, the thin section of tissue (4 μM) and the relatively large size of the foci that are produced by the DAB precipitate are all likely contributions to this issue. Therefore, in IHC studies, we were limited to categorizing alveolar cells as positive or negative for staining, which would clearly limit the sensitivity of the analysis, as we were not able to determine if positive alveolar cells have e.g. 5 foci or 25 foci. We found that it was possible to measure γH2AX and 53BP1 foci in alveolar cells by IF by confocal microscopy although the small size of the nuclei was still an issue in determining an accurate number for nuclear foci in tissue.

In contrast, in the larger nuclei of bronchioalveolar cells, we were able to discern clear foci by IHC, and therefore our analysis of the DDR response in these cells is likely to be more sensitive than in alveolar cells.

As noted above, the initial pattern of γH2AX and 53BP1 staining following radiation was similar in the ex vivo lung slice model and in lungs from mice irradiated in vivo, and the levels of residual DNA damage were also comparable, which leads us to conclude that DDR response is similar in both models. Given the technical limitations of detecting large numbers of clear foci by IHC, further work to develop IF methodology and apply it to larger sections of tissue

are warranted. In the present work, we confirmed that IF is more sensitive than IHC in detecting γH2AX and 53BP1 foci, but the manual analysis we employed is too complex and time consuming to be applied to large numbers of samples. Automated scanning and analysis/scoring methods on IF stained tissue sections should be an area of focus for future studies.

DNA double strand breaks are the most lethal lesion induced by ionising radiation, and when unrepaired they result in long-lived (≥ 24 h) or residual DNA damage. A new class of therapies, the DNA Damage Response (DDR) modulating agents is being investigated, that have the potential to increase the residual DNA damage induced by radiation by inhibiting DNA repair (e.g. PARP, DNA-PK inhibitors), or cell cycle response (e.g. ATR, WEE1), or a combination of both (e.g. ATM). Although these therapies are being developed to increase the effectiveness of radiation in treating cancer, the effects of these agents on normal tissues are rarely evaluated.

We believe ex vivo lung slices have the potential to carefully model biological responses to radiation plus accurate doses of DDR modulators to better understand what the normal tissue responses are, without the confounds of variable drug exposure found in vivo.

To this end, our data using the probe DNA-PK inhibitor are highly encouraging and lend support to our hypothesis. As expected from its mechanism of action (inhibiting DNA DSB repair) treatment with NU7441 significantly increased radiation-induced residual DNA DSBs, in a manner consistent with what others in our group have seen with the chemically related inhibitor NU5455 when used in vivo. More work is required to increase our knowledge of the potential benefits and limitations of the lung slice model for measuring drug-radiation responses. More detailed evaluation of DDR across different time points, especially in the early phases (< 6 h after irradiation) will be important to understand the biological effects of compounds on DNA repair rates. As mentioned previously, fractionated radiation schedules

(usually in 1.8 – 2 Gy per fraction) are used in the clinic, and would need more careful evaluation, although our current limitation of 3 days in culture might limit the utility of our model. Importantly, a key issue is to understand the differences in response to drug-radiation combinations in tumour and non-tumour tissue. In this study, we have not addressed this, however, in our laboratory we have established radiation-response characteristics in a model of carcinogen-induced lung cancer that reliably develops well defined adenocarcinomas. We believe that ex vivo lung tissue slices from this model, harbouring tumours that have developed within the lung architecture will have the potential to study tumour and non-tumour responses concurrently, side-by-side, in order to better understand the potential for DDR modulators to improve therapeutic index (i.e. greater toxic effects in tumour tissue than normal tissues). Alternatively, the ex vivo model could include the addition of mouse cancer cells (e,g. LLC) to investigate attachment and growth in the lungs and how they affect cell subtypes as the AT2 cells. Furthermore, other cancer types could be added to the lung tissues in culture that might aid in the understanding of metastatic growth and response in the tissue context.

The majority of the work presented has focused on IHC analysis of two major cell types in the lung, namely alveolar cells and bronchioepithelial cells. However, there are many subtypes of these cells and there are additionally other cell types that make up the lung tissue (Barkauskas et al. 2017). After irradiation, we noted that an AT2 alveolar cells expressed lower levels of γH2AX compared with alveolar cells as a whole, and this was also seen in the ex vivo tissue slice model. This is a potentially important finding, as we can hypothesize that the different cell types (or subtypes) in the lung may respond differently to ionizing radiation and may need to be studied in more detail. Cell specific markers (such as SPC) are available for several cell types in the lung (Barkauskas et al. 2017) which should allow cell-specific analysis of DDR after drug-radiation treatments. However, since these analyses will likely require multiplex

markers analysis (such as SPC, γH2AX and 53BP1) IF techniques and automated analysis methodology will likely need to be developed further before it becomes a practicable approach.

A limitation of the ex vivo lung slice model is the lack of immune cells, which form a cornerstone of current cancer treatment and also in the development of the tumour. Potentially this could be addressed by co-culturing tissue slices with immune cells isolated from the same animal. This method would require further development and assessment to see if immune cells respond similarly in the ex vivo setting and do not have any detrimental effects on the tissue.

Additionally, although radiation doses and drug concentrations administered to the ex vivo model can be comparable to those given in vivo, the ex vivo model lacks a whole-body impact. While the medication may not be harmful to lung tissue directly, it may have a distinct effect on other organs. A possible approach would be to slice and culture the mouse's other major organs as the liver, kidneys, intestines and add the medication in order to assess the effects of novel chemicals before exposing a live animal to them.

Because the model is only physiologically equivalent to mice lungs in vivo for 2 days, it is difficult to evaluate long-term adverse effects of radiation such as pneumonitis and fibrosis, which take roughly 6 months to develop in C57BL/6 mice as seen previously in our lab. However, utilizing the model to identify the cell types and populations that are harmed following radiation treatments and identifying intracellular and paracrine signaling would aid in understanding each cell's role. This data may be then utilized to conduct in-depth in vivo research. This strategy would help minimize the number of animals employed in each experiment and, when combined with live cell microscopy would allow for the real-time characterization of processes occurring within different cells as they occur. This identification and characterization of multiple cell types would lead to a better knowledge of the whole

picture and would allow researchers to investigate various approaches to avoid these adverse effects from happening.

As a conclusion, the precision-cut lung slice model performed well as a proxy for in vivo investigations of radiation and drug-radiation combinations. Rather than replacing existing models, studies in ex vivo lung slices could be utilized in conjunction with existing models to assist in addressing the issues relevant to the stage of the research at hand. The model is particularly well suited to studying biological effects in the tissue context where careful control of drug(s) concentration over time is required. This model may be used to test exploratory chemicals or chemical series that are not suitable for use on animals, and can inform the chemists in designing more effective compounds prior to in vivo testing. In addition, this model will allow the study of radiation or drug-radiation effects without the need for a complex and expensive in vivo irradiation platform, as the lung slices can be irradiated in simpler, less expensive radiation sources designed for cells. Additionally, the model may help in selecting a therapeutic window, resulting in fewer animals being tested and therefore exposed to harmful side effects.

7 Reference

Akram, Khondoker M., Laura L. Yates, Róisín Mongey, Stephen Rothery, David C.A. Gaboriau, Jeremy Sanderson, Matthew Hind, Mark Griffiths, and Charlotte H. Dean. 2019. "Live Imaging of Alveologenesis in Precision-Cut Lung Slices Reveals Dynamic Epithelial Cell Behaviour." *Nature Communications* 10 (1). https://doi.org/10.1038/s41467-019-09067-3.

Almeida, Celine, Devipriya Nagarajan, Jian Tian, Sofia Walder Leal, Kenneth Wheeler, Michael Munley, William Blackstock, and Weiling Zhao. 2013. "The Role of Alveolar Epithelium in Radiation-Induced Lung Injury." *PLoS ONE* 8 (1): 1–9. https://doi.org/10.1371/journal.pone.0053628.

Andersson-Sjöland, Annika, Jenny C. Karlsson, and Kristina Rydell-Törmänen. 2016. "ROS-Induced Endothelial Stress Contributes to Pulmonary Fibrosis through Pericytes and Wnt Signaling." *Laboratory Investigation* 96 (2): 206–17. https://doi.org/10.1038/labinvest.2015.100.

Asaithamby, Aroumougame, and David J. Chen. 2009. "Cellular Responses to DNA Double-Strand Breaks after Low-Dose γ-Irradiation." *Nucleic Acids Research* 37 (12): 3912–23. https://doi.org/10.1093/nar/gkp237.

Asmani, Mohammadnabi, Sanjana Velumani, Yan Li, Nicole Wawrzyniak, Isaac Hsia, Zhaowei Chen, Boris Hinz, and Ruogang Zhao. 2018. "Fibrotic Microtissue Array to Predict Anti-Fibrosis Drug Efficacy." *Nature Communications* 9 (1): 1–12. https://doi.org/10.1038/s41467-018-04336-z.

Baker, Sarah, and Alysa Fairchild. 2016. "Radiation-Induced Esophagitis in Lung Cancer." *Lung Cancer: Targets and Therapy* 7: 119–27. https://doi.org/10.2147/LCTT.S96443.

Barkauskas, Christina E., Mei I. Chung, Bryan Fioret, Xia Gao, Hiroaki Katsura, and Brigid L.M. Hogan. 2017. "Lung Organoids: Current Uses and Future Promise." *Development (Cambridge)* 144 (6): 986–97. https://doi.org/10.1242/dev.140103.

Barnard, Stephen, Simon Bouffler, and Kai Rothkamm. 2013. “The Shape of the Radiation Dose Response for DNA Double-Strand Break Induction and Repair.” *Genome Integrity* 4 (1): 1. https://doi.org/10.1186/2041-9414-4-1.

Barnes, Peter J. 2015. “Club Cells, Their Secretory Protein, and COPD.” *Chest* 147 (6): 1447–48. https://doi.org/10.1378/chest.14-3171.

Barré-Sinoussi, Françoise, and Xavier Montagutelli. 2015. “Animal Models Are Essential to Biological Research: Issues and Perspectives.” *Future Science OA* 1 (4): 4–6. https://doi.org/10.4155/fso.15.63.

Bentzen, Søren M. 2006. “Preventing or Reducing Late Side Effects of Radiation Therapy: Radiobiology Meets Molecular Pathology.” *Nature Reviews Cancer* 6 (9): 702–13. https://doi.org/10.1038/nrc1950.

Bolderston, Amanda, Nancy S. Lloyd, Rebecca K.S. Wong, Lori Holden, and Linda Robb-Blenderman. 2006. “The Prevention and Management of Acute Skin Reactions Related to Radiation Therapy: A Systematic Review and Practice Guideline.” *Supportive Care in Cancer* 14 (8): 802–17. https://doi.org/10.1007/s00520-006-0063-4.

Bonfield, TL. 2012. “In Vivo Models of Lung Disease.” *Lung Diseases - Selected State of the Art Reviews*. http://cdn.intechopen.com/pdfs/30259/InTech-In_vivo_models_of_lung_disease.pdf.

Brodin, O., L. Lennartsson, and S. Nilsson. 1991. “Single-Dose and Fractionated Irradiation of Four Human Lung Cancer Cell Lines in Vitro.” *Acta Oncologica* 30 (8): 967–74. https://doi.org/10.3109/02841869109088251.

Bryson, Karen Jane, Damien Garrido, Marco Esposito, Gerry McLachlan, Paul Digard, Catherine Schouler, Rodrigo Guabiraba, Sascha Trapp, and Lonneke Vervelde. 2020. “Precision Cut Lung Slices: A Novel Versatile Tool to Examine Host-Pathogen Interaction in the Chicken Lung.” *Veterinary Research* 51 (1): 1–16. https://doi.org/10.1186/s13567-019-0733-0.

Bussek, Alexandra, Erich Wettwer, Torsten Christ, Horst Lohmann, Patrizia Camelliti, and Ursula Ravens. 2009. “Tissue Slices from Adult Mammalian Hearts as a Model for Pharmacological Drug Testing.” *Cellular Physiology and Biochemistry* 24 (5–6): 527–36. https://doi.org/10.1159/000257528.

Cao, Xuefei, Jayme P. Coyle, Rui Xiong, Yiying Wang, Robert H. Heflich, Baiping Ren, William M. Gwinn, Patrick Hayden, and Liying Rojanasakul. 2021. “Invited Review: Human Air-Liquid-Interface Organotypic Airway Tissue Models Derived from Primary Tracheobronchial Epithelial Cells—Overview and Perspectives.” *In Vitro Cellular and Developmental Biology - Animal* 57 (2): 104–32. https://doi.org/10.1007/s11626-020-00517-7.

Carver, Joseph R., Charles L. Shapiro, Andrea Ng, Linda Jacobs, Cindy Schwartz, Katherine S. Virgo, Karen L. Hagerty, Mark R. Somerfield, and David J. Vaughn. 2007. “American Society of Clinical Oncology Clinical Evidence Review on the Ongoing Care of Adult Cancer Survivors: Cardiac and Pulmonary Late Effects.” *Journal of Clinical Oncology* 25 (25): 3991–4008. https://doi.org/10.1200/JCO.2007.10.9777.

Cavaliere, Fabio, and Carlos Matute. 2011. “Utility of Organotypic Slices in Parkinson’s Disease Research.” *Towards New Therapies for Parkinson’s Disease*, no. May. https://doi.org/10.5772/16902.

Chalmers, A. J., and R. D. Carruthers. 2021. “Radiobiology Summaries: DNA Damage and Repair.” *Clinical Oncology* 33 (5): 275–78. https://doi.org/10.1016/j.clon.2020.12.006.

Chaplin, Amanda K., Steven W. Hardwick, Shikang Liang, Antonia Kefala Stavridi, Ales Hnizda, Lee R. Cooper, Taiana Maia De Oliveira, Dimitri Y. Chirgadze, and Tom L. Blundell. 2021. “Dimers of DNA-PK Create a Stage for DNA Double-Strand Break Repair.” *Nature Structural and Molecular Biology* 28 (1): 13–19. https://doi.org/10.1038/s41594-020-00517-x.

Cho, Seongeun, Andrew Wood, and Mark R Bowlby. 2007. “Brain Slices as Models for Neurodegenerative Disease and Screening Platforms to Identify Novel Therapeutics.” *Current*

Neuropharmacology 5 (1): 19–33. https://doi.org/10.2174/157015907780077105.

Christodoulou, Marianna, Neil Bayman, Paula McCloskey, Carl Rowbottom, and Corinne Faivre-Finn. 2014. "New Radiotherapy Approaches in Locally Advanced Non-Small Cell Lung Cancer." *European Journal of Cancer* 50 (3): 525–34. https://doi.org/10.1016/j.ejca.2013.11.027.

Cornwell, Jocelyn. 2015. "Implementing Change." *Nursing Standard (Royal College of Nursing (Great Britain) : 1987)* 29 (26): 24–25. https://doi.org/10.7748/ns.29.26.24.s25.

Crystal, Ronald G. 2014. "Airway Basal Cells: The 'Smoking Gun' of Chronic Obstructive Pulmonary Disease." *American Journal of Respiratory and Critical Care Medicine* 190 (12): 1355–62. https://doi.org/10.1164/rccm.201408-1492PP.

Dabjan, Mohamad B., Carolyn M.S. Buck, Isabel L. Jackson, Zeljko Vujaskovic, Brian Marples, and Julian D. Down. 2016. "A Survey of Changing Trends in Modelling Radiation Lung Injury in Mice: Bringing out the Good, the Bad, and the Uncertain." *Laboratory Investigation* 96 (9): 936–49. https://doi.org/10.1038/labinvest.2016.76.

Davies, Emma J., Meng Dong, Matthias Gutekunst, Katja Närhi, Hanneke J.A.A. Van Zoggel, Sami Blom, Ashwini Nagaraj, et al. 2015. "Capturing Complex Tumour Biology in Vitro: Histological and Molecular Characterisation of Precision Cut Slices." *Scientific Reports* 5. https://doi.org/10.1038/srep17187.

Davis, Anthony J., and David J. Chen. 2013. "DNA Double Strand Break Repair via Non-Homologous End-Joining." *Translational Cancer Research* 2 (3): 130–43. https://doi.org/10.3978/j.issn.2218-676X.2013.04.02.

Davis, J. M. 1967. "The Structure of Guinea-Pig Lung Maintained in Organ Culture." *British Journal of Experimental Pathology* 48 (4): 371–78.

Davis, Jordan D., and Tomasz P. Wypych. 2021. "Cellular and Functional Heterogeneity of the

Airway Epithelium." *Mucosal Immunology* 14 (5): 978–90. https://doi.org/10.1038/s41385-020-00370-7.

Desai, Tushar J., Douglas G. Brownfield, and Mark A. Krasnow. 2014. "Alveolar Progenitor and Stem Cells in Lung Development, Renewal and Cancer." *Nature* 507 (7491): 190–94. https://doi.org/10.1038/nature12930.

Dobbs, L. G. 1990. "Isolation and Culture of Alveolar Type II Cells." *American Journal of Physiology - Lung Cellular and Molecular Physiology* 258 (3 2-2). https://doi.org/10.1152/ajplung.1990.258.4.l134.

Fang, Xiaoguang, Zhi Huang, Kui Zhai, Qian Huang, Weiwei Tao, Leo Kim, Qiulian Wu, et al. 2021. "Inhibiting DNA-PK Induces Glioma Stem Cell Differentiation and Sensitizes Glioblastoma to Radiation in Mice." *Science Translational Medicine* 13 (600). https://doi.org/10.1126/scitranslmed.abc7275.

Fehrenbach, Heinz. 2001. "FehrenbachH_RepiratoryResearch2001."

Fleming, Cathy, Daniel N. Cagney, Serena O'Keeffe, Sinead M. Brennan, John G. Armstrong, and Brendan McClean. 2016. "Normal Tissue Considerations and Dose–Volume Constraints in the Moderately Hypofractionated Treatment of Non-Small Cell Lung CancerOARs and DVCs for Hypofractionated NSCLC Tx." *Radiotherapy and Oncology* 119 (3): 423–31. https://doi.org/10.1016/j.radonc.2016.03.013.

Fok, Jacqueline H.L., Antonio Ramos-Montoya, Mercedes Vazquez-Chantada, Paul W.G. Wijnhoven, Valeria Follia, Neil James, Paul M. Farrington, et al. 2019. "AZD7648 Is a Potent and Selective DNA-PK Inhibitor That Enhances Radiation, Chemotherapy and Olaparib Activity." *Nature Communications* 10 (1): 1–15. https://doi.org/10.1038/s41467-019-12836-9.

Francisco, San, and San Francisco. 2008. "Kuo 2008 H2AX Biomarker for DNA Ds Breaks.Pdf" 310: 305–9. https://doi.org/0258-851X/2008.

Gähwiler, B. H. 1981. “Organotypic Monolayer Cultures of Nervous Tissue.” *Journal of Neuroscience Methods* 4 (4): 329–42. https://doi.org/10.1016/0165-0270(81)90003-0.

Gerweck, Leo E., Shashirekha Vijayappa, Akihiro Kurimasa, Kazuhiko Ogawa, and David J. Chen. 2006. “Tumor Cell Radiosensitivity Is a Major Determinant of Tumor Response to Radiation.” *Cancer Research* 66 (17): 8352–55. https://doi.org/10.1158/0008-5472.CAN-06-0533.

Ghita, Mihaela, Victoria Dunne, Gerard G. Hanna, Kevin M. Prise, Jaqueline P. Williams, and Karl T. Butterworth. 2019. “Preclinical Models of Radiation-Induced Lung Damage: Challenges and Opportunities for Small Animal Radiotherapy.” *British Journal of Radiology* 92 (1095). https://doi.org/10.1259/bjr.20180473.

Gonzales, Linda W., Sree Angampalli, Susan H. Guttentag, Mike F. Beers, Sheldon I. Feinstein, Anjaneyulu Matlapudi, and Philip L. Ballard. 2001. “Maintenance of Differentiated Function of the Surfactant System in Human Fetal Lung Type II Epithelial Cells Cultured on Plastic.” *Pediatric Pathology & Molecular Medicine* 20 (5): 387–412. https://doi.org/10.1080/15513810109168622.

Good, J. S., and K. J. Harrington. 2013. “The Hallmarks of Cancer and the Radiation Oncologist: Updating the 5Rs of Radiobiology.” *Clinical Oncology* 25 (10): 569–77. https://doi.org/10.1016/j.clon.2013.06.009.

Gopal, Murugaiyan, Samithamby Jey Jeyaseelan, James Harris, and Vijay Kumar. 2020. “Pulmonary Innate Immune Response Determines the Outcome of Inflammation During Pneumonia and Sepsis-Associated Acute Lung Injury.” *Frontiers in Immunology | Www.Frontiersin.Org* 1: 1722. https://doi.org/10.3389/fimmu.2020.01722.

Graves, Paul R., Farzan Siddiqui, Mitchell S. Anscher, and Benjamin Movsas. 2010. “Radiation Pulmonary Toxicity: From Mechanisms to Management.” *Seminars in Radiation Oncology* 20 (3): 201–7. https://doi.org/10.1016/j.semradonc.2010.01.010.

Griffin, M., R. Bhandari, G. Hamilton, Y. C. Chan, and J. T. Powell. 1993. “Alveolar Type II Cell-

Fibroblast Interactions, Synthesis and Secretion of Surfactant and Type I Collagen." *Journal of Cell Science* 105 (2): 423–32. https://doi.org/10.1242/jcs.105.2.423.

Gupta, Arun, Clayton R. Hunt, Sharmistha Chakraborty, Raj K. Pandita, John Yordy, Deepti B. Ramnarain, Nobuo Horikoshi, and Tej K. Pandita. 2014. "Role of 53BP1 in the Regulation." *Radiat Res.* 181 (1): 1–8. https://doi.org/10.1667/RR13572.1.Role.

Hall, Eric J., and Amato J. Giaccia. 2019. *Radiobiology for the Radiologist*. Eighth edition.; ... Philadelphia.

Hanahan, Douglas, and Robert A. Weinberg. 2011. "Hallmarks of Cancer: The next Generation." *Cell* 144 (5): 646–74. https://doi.org/10.1016/j.cell.2011.02.013.

Hartl, Dominik, Rabindra Tirouvanziam, Julie Laval, Catherine M. Greene, David Habiel, Lokesh Sharma, Ali Önder Yildirim, Charles S. Dela Cruz, and Cory M. Hogaboam. 2018. "Innate Immunity of the Lung: From Basic Mechanisms to Translational Medicine." *Journal of Innate Immunity* 10 (5–6): 487–501. https://doi.org/10.1159/000487057.

Healey, E. A., and A. Abner. 1995. "Thoracic and Cranial Radiotherapy for Limited-Stage Small Cell Lung Cancer." *Chest* 107 (6 SUPPL.): 249S-254S. https://doi.org/10.1378/chest.107.6_Supplement.249S.

Hickman, John A., Ralph Graeser, Ronald de Hoogt, Suzana Vidic, Catarina Brito, Matthias Gutekunst, Heiko van der Kuip, and Imi Predect consortium. 2014. "Three-Dimensional Models of Cancer for Pharmacology and Cancer Cell Biology: Capturing Tumor Complexity in Vitro/Ex Vivo." *Biotechnology Journal* 9 (9): 1115–28. https://doi.org/10.1002/biot.201300492.

Huh, Dongeun, Benjamin D. Matthews, Akiko Mammoto, Martin Montoya-Zavala, Hong Yuan Hsin, and Donald E. Ingber. 2010. "Reconstituting Organ-Level Lung Functions on a Chip." *Science* 328 (5986): 1662–68. https://doi.org/10.1126/science.1188302.

Irvin, Charles G, and Jason Ht Bates. 2003. "Measuring the Lung Function in the Mouse: The

Challenge of Size Airwayanimal Models of Diseaseasthmaforced Oscillationlungmechanicsmouse." *Respiratory Research* 4 (4): 1–9. http://www.respiratory-research/content/4/1/4.

Iwamoto, Kazunari, Hiroyuki Hamada, Yukihiro Eguchi, and Masahiro Okamoto. 2014. "Stochasticity of Intranuclear Biochemical Reaction Processes Controls the Final Decision of Cell Fate Associated with DNA Damage." *PLoS ONE* 9 (7): 1–12. https://doi.org/10.1371/journal.pone.0101333.

Jacks, Tyler, and Amy Keating. 2020. "An Organoid Platform to Study Alveolar Stem Cells in Lung Generation and Cancer An Organoid Platform to Study Alveolar Stem Cells in Lung Generation and Cancer," 1–135.

Kainthola, Anup, Teena Haritwal, Mrinialini Tiwari, Noopur Gupta, Suhel Parvez, Manisha Tiwari, Hrideysh Prakash, and Paban K. Agrawala. 2017. "Immunological Aspect of Radiation-Induced Pneumonitis, Current Treatment Strategies, and Future Prospects." *Frontiers in Immunology* 8 (MAY): 1–13. https://doi.org/10.3389/fimmu.2017.00506.

Kawakita, Naoya, Hiroaki Toba, Keiko Miyoshi, Shinichi Sakamoto, Daisuke Matsumoto, Mika Takashima, Mariko Aoyama, et al. 2020. "Bronchioalveolar Stem Cells Derived from Mouse-Induced Pluripotent Stem Cells Promote Airway Epithelium Regeneration." *Stem Cell Research and Therapy* 11 (1): 1–14. https://doi.org/10.1186/s13287-020-01946-7.

Kling, Melissa A. 2011. *A Review of Respiratory System Anatomy, Physiology, and Disease in the Mouse, Rat, Hamster, and Gerbil*. *Veterinary Clinics of North America - Exotic Animal Practice*. Vol. 14. https://doi.org/10.1016/j.cvex.2011.03.007.

Kong, F, T Ritter, and D Quint. 2010. "Consideration of Dose Limits for Organs at Risk of Thoracic Radiotherapy." *International Journal of Radiation Oncology* 1 (5): 1–16. https://doi.org/10.1016/j.ijrobp.2010.07.1977.CONSIDERATION.

Kumar, Vijay. 2020. "Pulmonary Innate Immune Response Determines the Outcome of Inflammation

During Pneumonia and Sepsis-Associated Acute Lung Injury." *Frontiers in Immunology* 11 (August): 1722. https://doi.org/10.3389/fimmu.2020.01722.

Li, Yu, Qi Wu, Xin Sun, Jun Shen, and Huaiyong Chen. 2020. "Organoids as a Powerful Model for Respiratory Diseases." *Stem Cells International* 2020. https://doi.org/10.1155/2020/5847876.

Lin, Chuwen, Hai Song, Cecilia Huang, Erica Yao, Rhodora Gacayan, Shan Mei Xu, and Pao Tien Chuang. 2012. "Alveolar Type II Cells Possess the Capability of Initiating Lung Tumor Development." *PLoS ONE* 7 (12). https://doi.org/10.1371/journal.pone.0053817.

Liu, Guanghui, Catherine Betts, Danen M. Cunoosamy, Per M. Åberg, Jorrit J. Hornberg, Kinga Balogh Sivars, and Taylor S. Cohen. 2019. "Use of Precision Cut Lung Slices as a Translational Model for the Study of Lung Biology." *Respiratory Research* 20 (1): 1–14. https://doi.org/10.1186/s12931-019-1131-x.

Liu, Qiaozhen, Kuo Liu, Guizhong Cui, Xiuzhen Huang, Shun Yao, Wenke Guo, Zhen Qin, et al. 2019. "Residing at the Bronchioalveolar-Duct Junction." *Nature Genetics* 51 (April). https://doi.org/10.1038/s41588-019-0346-6.

Lourenco, Luiza Helena Madia. 2017. "The Old and the New: Mouse Models for Evaluating the Therapeutic Margin of Radiation in Lung Cancer." Edited by Anderson Ryan.

Lyons-Cohen, Miranda R., Seddon Y. Thomas, Donald N. Cook, and Hideki Nakano. 2017. "Precision-Cut Mouse Lung Slices to Visualize Live Pulmonary Dendritic Cells." *Journal of Visualized Experiments* 2017 (122): 1–9. https://doi.org/10.3791/55465.

Marieb, Elaine Nicpon. 1992. *Human Anatomy and Physiology*. 2nd ed. Benjamin/Cummings Series in the Life Sciences. Redwood City, Calif. ; Wokingham: Benjamin/Cummings.

Mariotti, Luca G., Giacomo Pirovano, Kienan I. Savage, Mihaela Ghita, Andrea Ottolenghi, Kevin M. Prise, and Giuseppe Schettino. 2013. "Use of the γ-H2AX Assay to Investigate DNA Repair Dynamics Following Multiple Radiation Exposures." *PLoS ONE* 8 (11): 1–12.

https://doi.org/10.1371/journal.pone.0079541.

Martin, Jennifer. 2020. “The Impact of DNA Damage Inhibitors on the Therapeutic Window of Thoracic Radiation.”

Martin, Thomas R., and Charles W. Frevert. 2005. “Innate Immunity in the Lungs.” *Proceedings of the American Thoracic Society* 2 (5): 403–11. https://doi.org/10.1513/pats.200508-090js.

Mendoza, Arnulfo, Sung Hyeok Hong, Tanasa Osborne, Mohammed A. Khan, Kirk Campbell, Joseph Briggs, Ananth Eleswarapu, et al. 2010. “Modeling Metastasis Biology and Therapy in Real Time in the Mouse Lung.” *Journal of Clinical Investigation* 120 (8): 2979–88. https://doi.org/10.1172/JCI40252.

Mercer, R. R., and J. D. Crapo. 1993. “Lower Respiratory Tract Structure of Laboratory Animals and Humans: Dosimetry Implications.” *Aerosol Science and Technology* 18 (3): 257–71. https://doi.org/10.1080/02786829308959603.

Mohiuddin, Ismail S., and Min H. Kang. 2019. “DNA-PK as an Emerging Therapeutic Target in Cancer.” *Frontiers in Oncology* 9 (July): 1–8. https://doi.org/10.3389/fonc.2019.00635.

Ng Chee Ping. 2013. “基因的改变NIH Public Access.” *Bone* 23 (1): 1–7. https://doi.org/10.1016/j.biocel.2009.09.002.Clara.

Nickoloff, Jac A, Lynn Taylor, Neelam Sharma, and Takamitsu A Kato. 2020. “Exploiting DNA Repair Pathways for Tumor Sensitization , Mitigation of Resistance , and Normal Tissue Protection in Radiotherapy,” 244–63. https://doi.org/10.20517/cdr.2020.89.

Noda, Asao. 2018. “Radiation-Induced Unrepairable DSBs: Their Role in the Late Effects of Radiation and Possible Applications to Biodosimetry.” *Journal of Radiation Research* 59 (December 2017): ii114–20. https://doi.org/10.1093/jrr/rrx074.

Pan, Huaqin, Gail H. Deutsch, and Susan E. Wert. 2019. “Comprehensive Anatomic Ontologies for Lung Development: A Comparison of Alveolar Formation and Maturation within Mouse and

Human Lung." *Journal of Biomedical Semantics* 10 (1): 1–21. https://doi.org/10.1186/s13326-019-0209-1.

Parrish, Alan R, A Jay Gandolfi, and Klaus Brendel. 1995. "0024-3205(95)02176-O." *Liver* 57 (21): 1887–1901.

Picchio, Vittorio, Vittoria Cammisotto, Francesca Pagano, Roberto Carnevale, and Isotta Chimenti. 2021. " Innovative In Vitro Models for the Study of Lung Diseases ." In *Cell Interaction - Molecular and Immunological Basis for Disease Management*. IntechOpen. https://doi.org/10.5772/intechopen.95300.

Prise, Kevin M., and Anna Saran. 2011. "Concise Review: Stem Cell Effects in Radiation Risk." *Stem Cells* 29 (9): 1315–21. https://doi.org/10.1002/stem.690.

Qadir, Muhammad Imran, Amna Parveen, and Muhammad Ali. 2015. "Cdc42: Role in Cancer Management." *Chemical Biology and Drug Design* 86 (4): 432–39. https://doi.org/10.1111/cbdd.12556.

Rockwell, S. 1980. "IN VIVO-IN VITRO TUMOUR CELL LINES: CHARACTERISTICS AND LIMITATIONS AS MODELS FOR HUMAN CANCER." *Br. J. Cancer* 41.

Rogue, N A R Y Jane. n.d. "Human f e t a l Brain Cells i n Tissue Cultures : T h e i r Identification and Motility."

Rokicki, Wojciech, Marek Rokicki, Jacek Wojtacha, and Agata Dzeljijli. 2016. "The Role and Importance of Club Cells (Clara Cells) in the Pathogenesis of Some Respiratory Diseases." *Kardiochirurgia i Torakochirurgia Polska* 13 (1): 26–30. https://doi.org/10.5114/kitp.2016.58961.

Rothkamm, Kai, and Markus Löbrich. 2003. "Evidence for a Lack of DNA Double-Strand Break Repair in Human Cells Exposed to Very Low x-Ray Doses." *Proceedings of the National Academy of Sciences of the United States of America* 100 (9): 5057–62.

https://doi.org/10.1073/pnas.0830918100.

Rübe, Claudia E., Saskia Grudzenski, Martin Kühne, Xiaorong Dong, Nicole Rief, Markus Löbrich, and Christian Rübe. 2008. "DNA Double-Strand Break Repair of Blood Lymphocytes and Normal Tissues Analysed in a Preclinical Mouse Model: Implications for Radiosensitivity Testing." *Clinical Cancer Research* 14 (20): 6546–55. https://doi.org/10.1158/1078-0432.CCR-07-5147.

Rubin, Philip, Carl J. Johnston, Jacqueline P. Williams, Sandra McDonald, and Jacob N. Finkelstein. 1995. "A Perpetual Cascade of Cytokines Postirradiation Leads to Pulmonary Fibrosis." *International Journal of Radiation Oncology, Biology, Physics* 33 (1): 99–109. https://doi.org/10.1016/0360-3016(95)00095-G.

Sainz de Aja, J., A. F.M. Dost, and C. F. Kim. 2021. "Alveolar Progenitor Cells and the Origin of Lung Cancer." *Journal of Internal Medicine* 289 (5): 629–35. https://doi.org/10.1111/joim.13201.

Sanderson, Michael J. 2011. "Exploring Lung Physiology in Health and Disease with Lung Slices." *Pulmonary Pharmacology and Therapeutics* 24 (5): 452–65. https://doi.org/10.1016/j.pupt.2011.05.001.

Santivasi, Wil L., and Fen Xia. 2014. "Ionizing Radiation-Induced DNA Damage, Response, and Repair." *Antioxidants and Redox Signaling* 21 (2): 251–59. https://doi.org/10.1089/ars.2013.5668.

Schilders, Kim A.A., Evelien Eenjes, Sander van Riet, André A. Poot, Dimitrios Stamatialis, Roman Truckenmüller, Pieter S. Hiemstra, and Robbert J. Rottier. 2016. "Regeneration of the Lung: Lung Stem Cells and the Development of Lung Mimicking Devices." *Respiratory Research* 17 (1): 1–16. https://doi.org/10.1186/S12931-016-0358-Z.

Schultz, Linda B., Nabil H. Chehab, Asra Malikzay, and Thanos D. Halazonetis. 2000. "P53 Binding Protein 1 (53BP1) Is an Early Participant in the Cellular Response to DNA Double-Strand

Breaks." *Journal of Cell Biology* 151 (7): 1381–90. https://doi.org/10.1083/jcb.151.7.1381.

Sekine, Ikuo, Minako Sumi, Yoshinori Ito, Hiroshi Nokihara, Noboru Yamamoto, Hideo Kunitoh, Yuichiro Ohe, Tetsuro Kodama, Nagahiro Saijo, and Tomohide Tamura. 2006. "Retrospective Analysis of Steroid Therapy for Radiation-Induced Lung Injury in Lung Cancer Patients." *Radiotherapy and Oncology* 80 (1): 93–97. https://doi.org/10.1016/j.radonc.2006.06.007.

Sellgren, Katelyn L., Elizabeth J. Butala, Brian P. Gilmour, Scott H. Randell, and Sonia Grego. 2014. "A Biomimetic Multicellular Model of the Airways Using Primary Human Cells." *Lab on a Chip* 14 (17): 3349–58. https://doi.org/10.1039/c4lc00552j.

Sharma, Arishya, Kamini Singh, and Alexandru Almasan. 2012. "Histone H2AX Phosphorylation: A Marker for DNA Damage." In *Methods in Molecular Biology*, edited by Lotte Bjergbæk, 920:613–26. Totowa, NJ: Humana Press. https://doi.org/10.1007/978-1-61779-998-3_40.

Sharma, Ricky A, Ruth Plummer, Julie K Stock, Tessa A Greenhalgh, and Ozlem Ataman. 2016. "CONSENSUS Drug – Radiotherapy Combinations." *Nature Publishing Group* 13 (10): 627–42. https://doi.org/10.1038/nrclinonc.2016.79.

Sherman, Irwin W. 2008. "Chapter 5 In Vivo and In Vitro Models." *Advances in Parasitology* 67: 25–47. https://doi.org/10.1016/S0065-308X(08)00405-3.

Simian, Marina, and Mina J. Bissell. 2017. "Organoids: A Historical Perspective of Thinking in Three Dimensions." *Journal of Cell Biology* 216 (1): 31–40. https://doi.org/10.1083/jcb.201610056.

Siminski, J. T., T. J. Kavanagh, E. Chi, and G. Raghu. 1992. "Long-Term Maintenance of Mature Pulmonary Parenchyma Cultured in Serum-Free Conditions." *American Journal of Physiology - Lung Cellular and Molecular Physiology* 262 (1 6-1). https://doi.org/10.1152/ajplung.1992.262.1.l105.

Simmons, Szandor, Lasti Erfinanda, Christoph Bartz, and Wolfgang M. Kuebler. 2019. "Novel Mechanisms Regulating Endothelial Barrier Function in the Pulmonary Microcirculation."

Journal of Physiology 597 (4): 997–1021. https://doi.org/10.1113/JP276245.

Sit, Rene V, Stephen Chang, Stephanie D Conley, Yasuo Mori, and Jun Seita. 2019. "Travaglini et Al, p. 1" 7191.

Stoppini, L., P. A. Buchs, and D. Muller. 1991. "A Simple Method for Organotypic Cultures of Nervous Tissue." *Journal of Neuroscience Methods* 37 (2): 173–82. https://doi.org/10.1016/0165-0270(91)90128-M.

Stripp, B. R., K. Maxson, R. Mera, and G. Singh. 1995. "Plasticity of Airway Cell Proliferation and Gene Expression after Acute Naphthalene Injury." *American Journal of Physiology - Lung Cellular and Molecular Physiology* 269 (6 13-6). https://doi.org/10.1152/ajplung.1995.269.6.l791.

Suarez, Carlos Jose, Suzanne M. Dintzis, and Charles W. Frevert. 2012. "Respiratory." *Comparative Anatomy and Histology*, 121–34. https://doi.org/10.1016/B978-0-12-381361-9.00009-3.

Sucre, Jennifer M.S., Christopher S. Jetter, Holli Loomans, Janice Williams, Erin J. Plosa, John T. Benjamin, Lisa R. Young, et al. 2018. "Successful Establishment of Primary Type II Alveolar Epithelium with 3D Organotypic Coculture." *American Journal of Respiratory Cell and Molecular Biology* 59 (2): 158–66. https://doi.org/10.1165/rcmb.2017-0442MA.

Sveiven, Stefanie Noel, and Tara M. Nordgren. 2020. "Lung-Resident Mesenchymal Stromal Cells Are Tissue-Specific Regulators of Lung Homeostasis." *American Journal of Physiology - Lung Cellular and Molecular Physiology* 319 (2): L197–210. https://doi.org/10.1152/AJPLUNG.00049.2020.

Travis, Elizabeth L., Girish Rachakonda, Xinhui Zhou, Katrina Korhonen, Konjeti R. Sekhar, Swati Biswas, and Michael L. Freeman. 2011. "NRF2 Deficiency Reduces Life Span of Mice Administered Thoracic Irradiation." *Free Radical Biology and Medicine* 51 (6): 1175–83. https://doi.org/10.1016/j.freeradbiomed.2011.05.038.

Treuting, Piper M, and Suzanne M Dintzis. 2012. *Comparative Anatomy and Histology : A Mouse and Human Atlas*. Oxford: Academic.

Trowell, OA. 1959. "The Culture of Mature Organs." *Cell Research* 147: 118–47.

Tsoutsou, Pelagia G., and Michael I. Koukourakis. 2006. "Radiation Pneumonitis and Fibrosis: Mechanisms Underlying Its Pathogenesis and Implications for Future Research." *International Journal of Radiation Oncology Biology Physics* 66 (5): 1281–93. https://doi.org/10.1016/j.ijrobp.2006.08.058.

Valdiglesias, Vanessa, Simona Giunta, Michael Fenech, Monica Neri, and Stefano Bonassi. 2013. "ΓH2AX as a Marker of DNA Double Strand Breaks and Genomic Instability in Human Population Studies." *Mutation Research - Reviews in Mutation Research* 753 (1): 24–40. https://doi.org/10.1016/j.mrrev.2013.02.001.

WARD, H. E., and T. E. NICHOLAS. 1984. "Alveolar Type I and Type Ii Cells." *Australian and New Zealand Journal of Medicine* 14: 731–34. https://doi.org/10.1111/j.1445-5994.1984.tb04928.x.

Weiss, Daniel J. 2014. "Concise Review: Current Status of Stem Cells and Regenerative Medicine in Lung Biology and Diseases." *Stem Cells* 32 (1): 16–25. https://doi.org/10.1002/stem.1506.

Werner-Wasik, Maria, Ellen Yorke, Joseph Deasy, Jiho Nam, and Lawrence B. Marks. 2010. "Radiation Dose-Volume Effects in the Esophagus." *International Journal of Radiation Oncology Biology Physics* 76 (3 SUPPL.): 86–93. https://doi.org/10.1016/j.ijrobp.2009.05.070.

Wilding, Jennifer L., and Walter F. Bodmer. 2014. "Cancer Cell Lines for Drug Discovery and Development." *Cancer Research* 74 (9): 2377–84. https://doi.org/10.1158/0008-5472.CAN-13-2971.

Wilkinson, Dan, Jackelyn Alva-Ornelas, Jennifer Sucre, Preethi Vijayaraj, Wade Durra, Abdo, Richardson, Steven Jonas, Manash Paul, Saravanan Karumbayaram, Bruce Dunn, and Brigitte

Gomperts. 2016. “Tissue Engineering and Regenerative Medicine T ISSUE E NGINEERING AND R EGENERATIVE M EDICINE Concise Review : The Potential Use of Intestinal Stem Cells to Treat Patients With Intestinal Failure.” *Stem Cells Translational Medicine* 4: 1–11.

Willers, H., J. Dahm-Daphi, and S. N. Powell. 2004. “Repair of Radiation Damage to DNA.” *British Journal of Cancer* 90 (7): 1297–1301. https://doi.org/10.1038/sj.bjc.6601729.

Willoughby, Catherine E., Yanyan Jiang, Huw D. Thomas, Elaine Willmore, Suzanne Kyle, Anita Wittner, Nicole Phillips, et al. 2020. “Selective DNA-Pkcs Inhibition Extends the Therapeutic Index of Localized Radiotherapy and Chemotherapy.” *Journal of Clinical Investigation* 130 (1): 258–71. https://doi.org/10.1172/JCI127483.

Wu, Ailing, and Hai Song. 2021. “Regulation of Alveolar Type 2 Stem/Progenitor Cells in Lung Injury and Regeneration.” *Acta Biochimica et Biophysica Sinica* 52 (7): 716–22. https://doi.org/10.1093/ABBS/GMAA052.

Wu, Huijuan, Yuanyuan Yu, Huanwei Huang, Yucheng Hu, Siling Fu, Zheng Wang, Mengting Shi, et al. 2020. “Progressive Pulmonary Fibrosis Is Caused by Elevated Mechanical Tension on Alveolar Stem Cells.” *Cell* 180 (1): 107-121.e17. https://doi.org/10.1016/j.cell.2019.11.027.

Xu, Min, Wei Yang, Xuanchuan Wang, and Deepak Kumar Nayak. 2020. “Lung Secretoglobin Scgb1a1 Influences Alveolar Macrophage-Mediated Inflammation and Immunity.” *Frontiers in Immunology* 11 (October): 1–12. https://doi.org/10.3389/fimmu.2020.584310.

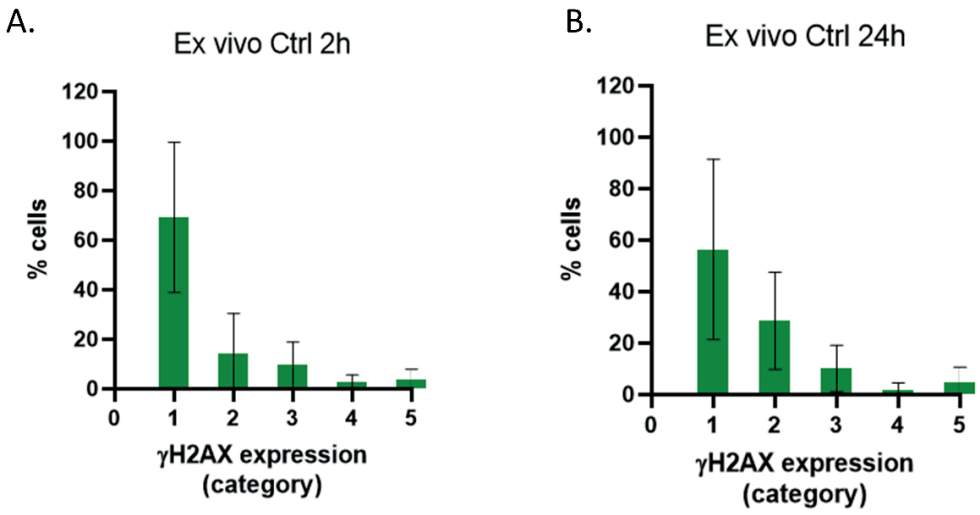
8 Appendix

8.1 Supplementary Data

Supplementary Table 1. Equilibration of the filter.

The filter was put in 6-well plates containing varying amounts of media (1 mL, 1.5 mL, 2 mL and 3 mL). The inner surface of the filter was wetted with 500 µL of medium, which was then withdrawn and reinserted into the 6-well plate. The filter was then monitored at various time intervals to determine when it equilibrates to a stable level of medium within the filter and how much medium is inside. It was critical to remember the air-liquid interface. It was determined that the filter equilibrates at 2-24 h. The volume of medium to cover a slice was determined to be between of 1.6 mL to 2 mL. (Following this experiment and according to experience with tissue slices it was concluded that 1.65 mL of medium was needed for small tissue slices and around 2 mL for larger slices)

Time (h)	**1 mL**	**1.5 mL**	**2 mL**	**3 mL**
1	-	-	-	-
2	Medium inside filter (barely visible)	Medium inside filter (too little to cover the tissue)	Medium inside filter (covered the filter -good for large slice)	Medium inside filter (soaked)
4		Nothing changed	Nothing changed	Nothing changed
24		Nothing changed	Nothing changed	Nothing changed



Supplementary Figure 1. Categories of γH2AX staining in mock irradiated (0 Gy) ex vivo lung slices. A) Ctrl samples in culture and fixed at 2h, B) Ctrl samples in culture fixed at 24h, showing a little background effect. Graph bars represent the average in the group (n=2 (2 experimental replicates where for each sample 5 random fields were imaged were possible and around 30-50 cells were scored in each field of view). Error bars represent ± SEM

Supplementary Table 2. Descriptive statistics of figure 5.11B for in vivo samples stained with γH2AX. Scored positively stained alveolar cells. fv represents the number of fields of view counted from 2 experimental replicates

Time (h)	Ctrl In vivo			In vivo (10Gy)		
	Mean	SEM	fv	Mean	SEM	fv
0	1.2225	0.569	4			
2				61.36	3.378	4
8				36.55	5.038	4
24				32.91	2.526	4

Supplementary Table 3. Descriptive statistics of figure 5.11C for ex vivo samples stained with γH2AX. Scored positively stained alveolar cells. 3 lungs were sliced one for each radiation dose. No. fv reprsensts the number of fields of view scored from 2 experimental replicates. There were technical replicates for each sample within an experiment.

Time (h)	Ctrl Ex vivo			Ex Vivo (0Gy)			Ex Vivo (2 Gy)			Ex Vivo (10Gy)		
	Mean	SEM	fv	Mean	SEM	fv	Mean	SEM	fv	Mean	SEM	fv
0	0.553	0.198	24									
2				3.944	1.139	8	48.20	2.799	8	64.28	3.39	8
8				7.828	0.644	8	31.09	2.636	8	62.70	4.89	8
24				11.42	1.328	8	17.74	2.029	8	30.75	2.41	8

Supplementary Table 4. Descriptive statistics of figure 5.12A for in vivo samples stained with 53BP1. Counting positively stained bronchioepithelial cells. fv represents the number of fields of view counted from 2 experimental replicates

Time (h)	Ctrl In vivo			In vivo (10Gy)		
	Mean	SEM	fv	Mean	SEM	fv
0	4.64	1.62	4			
2				64.11	5.85	4
8				60.05	13.83	4
24				57.69	11.89	4

Supplementary Table 5. Descriptive statistics of figure 5.12B for ex vivo samples stained with 53BP1. Counting positively stained bronchioepithelial cells. 3 lungs were sliced one for each radiation dose. Fv represents the number of fields of view scored from 2 experimental replicates. There were technical replicates for each sample within an experiment.

Time (h)	Ctrl Ex vivo			Ex Vivo (0 Gy)			Ex Vivo (2 Gy)			Ex Vivo (10 Gy)		
	Mean	SEM	fv	Mean	SEM	fv	Mean	SEM	fv	Mean	SEM	fv
0	5.014	0.72	20									
2				9.69	4.00	6	83.53	6.15	6	71.3	3.21	6
8				19.69	2.76	8	51.34	5.00	8	78.4	5.81	8
24				13.74	2.71	8	20.06	2.99	8	63.8	6.39	6

Supplementary Table 6. Descriptive statistics of figure 5.12C for in vivo samples stained with 53BP1. Scored 53BP1 foci in positively stained bronchioepithelial cells. N represents 2 experimental replicates where 20 cells were scored from each experiment were possible (10 from each field of view)

Time (h)	Ctrl In vivo			In vivo (10Gy)		
	Mean	SEM	N	Mean	SEM	N
0	2.6	0.715	2			
2				10.98	1.28	2
8				7.35	0.75	2
24				3.62	0.025	2

Supplementary Table 7. Descriptive statistics of figure 5.12D for ex vivo samples stained with 53BP1. Scored 53BP1 foci in positively stained bronchioepithelial cells. N represents 2 experimental replicates which each had technical replicates where 20 cells were scored from each experiment were possible (10 from each field of view)

Time (h)	Ctrl Ex vivo			Ex Vivo (0 Gy)			Ex Vivo (2 Gy)			Ex Vivo (10Gy)		
	Mean	SEM	N	Mean	SEM	N	Mean	SEM	N	Mean	SEM	N
0	2.89	0.41	2									
2				2.47	1.24	2	6.67	1.23	2	12.35	0.88	2
8				3.68	0.69	2	3.69	0.15	2	8.35	0.53	2
24				3.92	0.22	2	2.61	0.22	2	4.5	0.32	2

Supplementary Table 8. Descriptive statistics of figure 5.15B for ex vivo samples stained with γH2AX. Scored positively stained alveolar cells. 3 lungs were sliced one for each radiation dose. Fv represents the number of fields of view scored from 2 experimental replicates. There were technical replicates for each sample within an experiment.

	Ctrl Ex vivo	0Gy	1μM Nu7441	5μM Nu7441	10μM Nu7441	10Gy	1μM Nu7441 (10Gy)	5μM Nu7441 (10GY)	10μM Nu7441 (10Gy)
Mean	2.27	6.35	2.67	3.60	3.16	38.9	45.61	42.43	45.09
SEM	1.16	2.14	0.81	1.36	0.81	1.51	3.32	1.36	3.02
fv	16	8	8	8	8	8	8	8	8

Supplementary Table 9. Descriptive statistics of figure 5.15C for ex vivo samples stained with γH2AX. Scored positively stained bronchioepithelial cells. 3 lungs were sliced one for each radiation dose. Fv represents the number of fields of view scored from 2 experimental replicates. There were technical replicates for each sample within an experiment.

	Ctrl Ex vivo	0Gy	1μM Nu7441	5μM Nu7441	10μM Nu7441	10Gy	1μM Nu7441 (10Gy)	5μM Nu7441 (10GY)	10μM Nu7441 (10Gy)
Mean	3.04	26.6	11.51	9.42	12.77	73.1	73.08	91.38	97.54
SEM	0.73	6.16	1.78	2.61	4.11	1.63	1.88	2.08	0.85
fv	16	8	8	6	6	8	8	8	8

Supplementary Table 10. Descriptive statistics of figure 5.15D for ex vivo samples stained with γH2AX. Scored γH2AX foci positively stained bronchioepithelial cells. 3 lungs were sliced one for each radiation dose. Fv represents the number of cells counted for each sample.

	Ctrl Ex vivo	0Gy	1μM Nu7441	5μM Nu7441	10μM Nu7441	10Gy	1μM Nu7441 (10Gy)	5μM Nu7441 (10GY)	10μM Nu7441 (10Gy)
Mean	1.87	3.93	3.62	2.95	2.31	4.01	4.95	8.45	12.73
SEM	0.34	0.38	0.39	0.51	0.36	0.28	0.32	0.42	0.51
fv	23	73	60	42	39	80	80	80	80

Supplementary Table 11. Descriptive statistics of figure 5.16A for ex vivo samples stained with 53BP1. Scored positively stained bronchioepithelial cells. 3 lungs were sliced one for each radiation dose. Fv represents the number of fields of view scored from 2 experimental replicates. There were technical replicates for each sample within an experiment.

	Ctrl Ex vivo	0Gy	1µM Nu7441	5µM Nu7441	10µM Nu7441	10Gy	1µM Nu7441 (10Gy)	5µM Nu7441 (10GY)	10µM Nu7441 (10Gy)
Mean	3.01	13.3	6.95	3.78	4.85	59.6	69.83	86.2	94.61
SEM	0.54	1.74	1.64	0.98	1.03	5.11	4.88	2.76	2.63
fv	16	8	8	6	4	8	7	8	8

Supplementary Table 12. Descriptive statistics of figure 5.16B for ex vivo samples stained with 53BP1. Scored 53BP1 foci positively stained bronchioepithelial cells. 3 lungs were sliced one for each radiation dose. Fv represents the number of cells counted for each sample.

	Ctrl Ex vivo	0Gy	1µM Nu7441	5µM Nu7441	10µM Nu7441	10Gy	1µM Nu7441 (10Gy)	5µM Nu7441 (10GY)	10µM Nu7441 (10Gy)
Mean	2.54	3.82	2.19	1.77	1.91	4.18	4.24	7.9	9.4
SEM	0.27	0.31	0.23	0.33	1.43	3.61	3.62	7.09	8.64
fv	50	78	54	17	21	80	80	80	80

Supplementary Table 13. Descriptive statistics of figure 5.17B for ex vivo SCID mice samples stained with γH2AX. Scored positively stained alveolar cells. 2 lungs were sliced. Fv represents the number of fields of view scored from 1 experiment. Ctrl was 1 slice from each lung was scored with 2 fields of view. 6 technical replicates for 0 Gy and 6 for 10 Gy samples were scored.

	Ctrl	0Gy	10Gy
Mean	1.77	4.29	51.33
SEM	0.74	1.28	2.34
fv	4	12	12

Supplementary Table 14. Descriptive statistics of figure 5.17B for ex vivo SCID mice samples stained with γH2AX. Scored positively stained bronchioepithelial cells. 2 lungs were sliced. Fv represents the number of fields of view scored from 1 experiment. Ctrl was 1 slice from each lung was scored with 2 fields of view. 6 technical replicates for 0 Gy and 6 for 10 Gy samples were scored (some samples were marked not scorable due to the absence of bronchioepithelial cells).

	Ctrl	0Gy	10Gy
Mean	10.86	11.96	92.31
SEM	2.43	2.49	1.68
fv	4	12	10

Supplementary Table 15. Descriptive statistics of figure 5.17C for ex vivo SCID mice samples stained with γH2AX. Scored γH2AX foci positively stained bronchioepithelial cells. 2 lungs were sliced. N represents the number of cells counted for each sample (10 cells from each field of view).

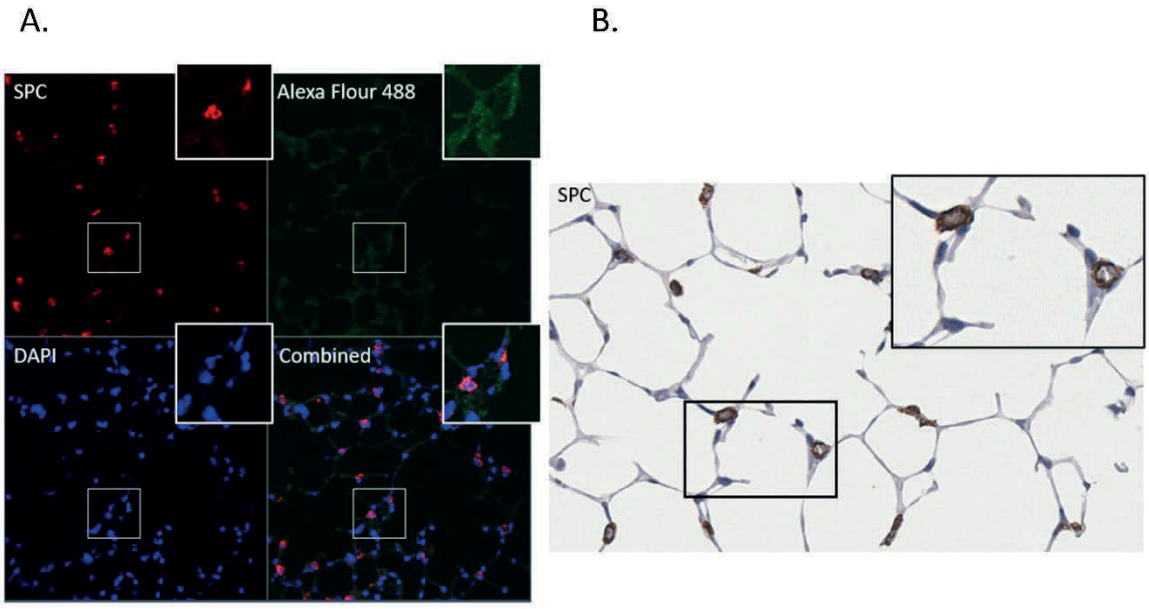
	Ctrl	0Gy	10Gy
Mean	3.88	4.21	9.63
SEM	0.47	0.41	0.35
n	40	81	100

Supplementary Table 16. Descriptive statistics of figure 5.17F for ex vivo SCID mice samples stained with 53BP1. Scored positively stained bronchioepithelial cells. 2 lungs were sliced. Fv represents the number of fields of view scored from 1 experiment. Ctrl was 1 slice from each lung was scored with 2 fields of view. 6 technical replicates for 0 Gy and 6 for 10 Gy samples were scored (some samples were marked not scorable due to the absence of bronchioepithelial cells).

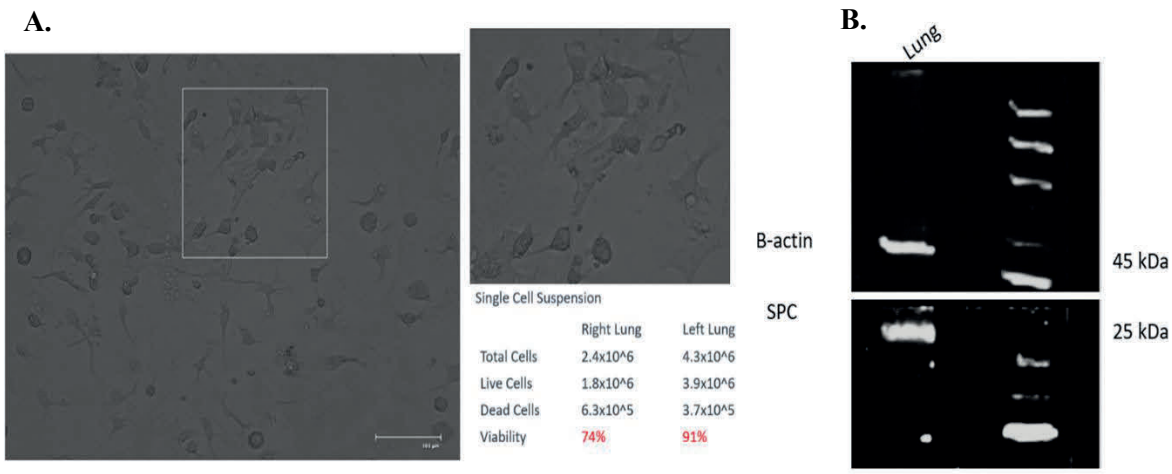
	Ctrl	0Gy	10Gy
Mean	7.61	12.32	75.62
SEM	0.82	2.21	3.26
fv	4	12	10

Supplementary Table 17. Descriptive statistics of figure 5.17C for ex vivo SCID mice samples stained with 53BP1. Scored 53BP1 foci positively stained bronchioepithelial cells. 2 lungs were sliced. N represents the number of cells counted for each sample (10 cells from each field of view).

	Ctrl	0Gy	10Gy
Mean	2.12	2.99	8.95
SEM	0.18	0.22	0.35
n	33	90	99



Supplementary Figure 2. SPC staining by IF and IHC in ex vivo tissue slices. Staining of SPC with rabbit anti-SPC primary antibody and IF using anti-rabbit Alexafluor 555. Anti-mouse Alexafluor 488 did not stain SPC. B) IHC staining of SPC.



Supplementary Figure 3. Separating SPC$^+$ cells from C57BL/6 mice lungs.

an image taken following single cell suspension of C57BL/6 showing that the protocol would yield around 70% viable cells. C) a western blot done following single cell suspension to see if SPC+ cell is still present even after the procedure.

8.2 Raw Statistical Data

Raw statistical data corresponding to figure 5.10 (B) in thesis.

		P-value	Significant or not	difference between means (±SEM)	95% confidence interval
ctrl group 1	**2h group 1**	<0.0001	yes (***)	-73.49 ± 2.283	-78.29 to -68.70
ctrl group 2	**24h group 1**	<0.0001	yes (***)	-60.50 ± 4.960	-70.92 to -50.08
ctrl group 2	**2h group 2**	<0.0001	yes (***)	10.38 ± 1.869	6.457 to 14.31
ctrl group 2	**24h group2**	<0.0001	yes (***)	24.58 ± 2.391	19.56 to 29.60
ctrl group 3	**2h group 3**	<0.0001	Yes (***)	16.32 ± 2.195	11.71 to 20.93
ctrl group 3	**24h group 3**	<0.0001	Yes (***)	20.96 ± 2.613	15.47 to 26.45
ctrl group 4	**2h group 4**	<0.0001	Yes (***)	14.10 ± 0.9272	12.20 to 16.00
ctrl group 4	**24h group 4**	<0.0001	Yes (***)	9.951 ± 1.480	6.919 to 12.98
ctrl group 5	**2h group 5**	<0.0001	Yes (***)	32.04 ± 3.036	25.66 to 38.42
ctrl group 5	**24h group 5**	<0.0001	Yes (***)	4.664 ± 0.8884	2.798 to 6.530

Raw statistical data corresponding to figure 5.10 (C) in thesis.

		P-value	Significant or not	difference between means (±SEM)	95% confidence interval
Ctrl group 1	**2h group 1**	<0.0001	Yes (***)	-55.38 ± 5.048	-65.74 to -45.02
ctrl group 2	**24h group 1**	<0.0001	Yes (***)	-35.89 ± 5.609	-47.38 to -24.40
ctrl group 2	**2h group 2**	<0.0001	Yes (***)	-21.38 ± 3.443	-28.33 to -14.43
ctrl group 2	**24h group2**	0.1102	NO	-6.217 ± 3.812	-13.90 to 1.470
ctrl group 3	**2h group 3**	0.0004	Yes (***)	6.491 ± 1.611	3.186 to 9.796
ctrl group 3	**24h group 3**	<0.0001	Yes (***)	19.43 ± 2.405	14.50 to 24.36
ctrl group 4	**2h group 4**	<0.0001	Yes (***)	18.49 ± 1.393	18.49 ± 1.393
ctrl group 4	**24h group 4**	<0.0001	Yes (***)	13.41 ± 0.9543	11.49 to 15.34
ctrl group 5	**2h group 5**	<0.0001	Yes (***)	50.59 ± 4.122	42.13 to 59.04
ctrl group 5	**24h group 5**	<0.0001	Yes (***)	8.754 ± 1.188	6.320 to 11.19

Raw statistical data corresponding to figure 5.11 (B)

		P-value	Significant or not	difference between means (±SEM)	95% confidence interval
0Gy	**2h**	<0.0001	Yes (***)	60.14 ± 3.426	51.75 to 68.52
2h	**8h**	0.0064	yes (**)	-24.81 ± 6.066	-39.65 to -9.961
2h	**24h**	0.0005	Yes (***)	-28.46 ± 4.219	-38.78 to -18.13
8h	**24h**	0.5413	No	-3.650 ± 5.637	-17.44 to 10.14

Raw statistical data corresponding to figure 5.11 (C)

		P-value	Significant or not	difference between means (±SEM)	95% confidence interval
Ctrl ex vivo	**0Gy 2h**	<0.0001	Yes (***)	3.390 ± 0.7245	1.910 to 4.870
0Gy 2h	**2Gy 2h**	<0.0001	Yes (***)	44.26 ± 3.022	37.78 to 50.75
0GY 2h	**10Gy 2h**	<0.0001	yes (***)	60.34 ± 3.577	52.67 to 68.01
0Gy 8h	**2Gy 8h**	<0.0001	Yes (***)	23.27 ± 2.714	17.45 to 29.09
0Gy 8h	**10 Gy 8h**	<0.0001	Yes (***)	54.88 ± 4.937	44.29 to 65.46
0Gy 24h	**2Gy 24h**	0.0207	Yes (*)	6.321 ± 2.426	1.119 to 11.52
0Gy 24h	**10Gy 24h**	<0.0001	Yes (***)	19.32 ± 2.753	13.42 to 25.23
2Gy 2h	**2Gy 8h**	0.0005	Yes (***)	-17.11 ± 3.845	-25.36 to -8.863
2Gy 2h	**2Gy 24h**	<0.0001	Yes (***)	-30.46 ± 3.458	-37.87 to -23.04
10Gy 2h	**10Gy 8h**	0.7944	No	-1.581 ± 5.954	-14.35 to 11.19
10Gy 2h	**10Gy 24h**	<0.0001	Yes (***)	-33.54 ± 4.160	-42.46 to -24.61

Raw statistical data corresponding to figure 5.12 (A)

		P-value	Significant or not	difference between means (±SEM)	95% confidence interval
0Gy	**2h**	<0.0001	Yes (***)	59.48 ± 5.655	46.88 to 72.07
2h	**8h**	0.7153	No	-4.057 ± 10.81	-28.15 to 20.03
2h	**24h**	0,5238	No	-6.422 ± 9.721	-28.08 to 15.24
8h	**24h**	0,9011	No	-2.365 ± 18.25	-47.01 to 42.28

Raw statistical data corresponding to figure 5.12 (C)

		P-value	Significant or not	difference between means (±SEM)	95% confidence interval
0Gy	**2h**	<0.0001	Yes (***)	8.213 ± 0.6828	6.847 to 9.579
2h	**8h**	<0.0001	Yes (***)	-3.625 ± 0.6756	-4.970 to -2.280
2h	**24h**	<0.0001	Yes (***)	-7.350 ± 0.5091	-8.364 to -6.336
8h	**24h**	<0.0001	Yes (***)	-3.725 ± 0.5398	-4.800 to -2.650

Raw statistical data corresponding to figure 5.12 (B)

		P-value	Significant or not	difference between means (±SEM)	95% confidence interval
Ctrl ex vivo	**0Gy 2h**	0.0709	No	4.674 ± 2.473	-0.4297 to 9.778
0Gy 2h	**2Gy 2h**	<0.0001	Yes (***)	73.84 ± 7.336	57.49 to 90.18
0GY 2h	**10Gy 2h**	<0.0001	Yes (***)	61.68 ± 5.128	50.25 to 73.10
0Gy 8h	**2Gy 8h**	<0.0001	yes (***)	31.65 ± 5.715	19.39 to 43.91
0Gy 8h	**10 Gy 8h**	<0.0001	yes (***)	58.71 ± 6.431	44.92 to 72.51
0Gy 24h	**2Gy 24h**	0.1398	No	6.316 ± 4.035	-2.339 to 14.97
0Gy 24h	**10Gy 24h**	<0.0001	Yes (***)	50.12 ± 6.302	36.39 to 63.85
2Gy 2h	**2Gy 8h**	0.0015	Yes (**)	-32.19 ± 7.849	-49.29 to -15.08
2Gy 2h	**2Gy 24h**	<0.0001	Yes (***)	-63.47 ± 6.306	-77.21 to -49.73
10Gy 2h	**10Gy 8h**	0.3546	No	7.036 ± 7.307	-8.885 to 22.96
10Gy 2h	**10Gy 24h**	0.3186	No	-7.502 ± 7.147	-23.43 to 8.424

Raw statistical data corresponding to figure 5.12 (D)

		P-value	Significant or not	difference between means (±SEM)	95% confidence interval
Ctrl ex vivo	**0Gy 2h**	0.2596	No	0.4853 ± 0.4288	-0.3621 to 1.333
0Gy 2h	**2Gy 2h**	<0.0001	Yes (***)	2.956 ± 0.6180	1.729 to 4.183
0GY 2h	**10Gy 2h**	<0.0001	Yes (***)	8.639 ± 0.5877	7.473 to 9.806
0Gy 8h	**2Gy 8h**	0.9701	No	0.01250 ± 0.3330	-0.6452 to 0.6702
0Gy 8h	**10 Gy 8h**	<0.0001	Yes (***)	4.663 ± 0.4008	3.871 to 5.454
0Gy 24h	**2Gy 24h**	0.0004	Yes	-1.335 ± 0.3675	-2.062 to -0.6090
0Gy 24h	**10Gy 24h**	0.1577	No	0.6123 ± 0.4310	-0.2401 to 1.465
2Gy 2h	**2Gy 8h**	<0.0001	Yes (***)	-2.979 ± 0.4035	-3.777 to -2.181
2Gy 2h	**2Gy 24h**	<0.0001	Yes (***)	-4.081 ± 0.4316	-4.935 to -3.227
10Gy 2h	**10Gy 8h**	<0.0001	Yes (***)	-4.013 ± 0.4605	-4.923 to -3.102
10Gy 2h	**10Gy 24h**	<0.0001	Yes (***)	-7.817 ± 0.4797	-8.767 to -6.867

Raw statistical data corresponding to figure 5.15 (B)

		P-value	Significant or not	difference between means (±SEM)	95% confidence interval
ctrl Ex vivo	**0GY**	0.08	No	4.074 ± 2.221	-0.5318 to 8.679
0Gy	**1µM Nu7441**	0.1303	No	-3.675 ± 2.286	-8.579 to 1.229
0Gy	**5µM Nu7441**	0.296	No	-2.751 ± 2.534	-8.187 to 2.685
0Gy	**10µM Nu7441**	0.3547	No	-2.188 ± 2.285	-7.089 to 2.714
0GY	**10Gy**	<0.0001	Yes (***)	32.55 ± 2.617	26.94 to 38.16
10Gy	**1µM Nu7441 +10Gy**	0.0873	No	6.711 ± 3.651	-1.119 to 14.54
10Gy	**5µM Nu7441+ 10Gy**	0.1033	No	3.538 ± 2.030	-0.8168 to 7.892
10Gy	**10µM Nu7441 + 10Gy**	0.0875	No	6.198 ± 3.374	-1.038 to 13.43

Raw statistical data corresponding to figure 5.15 (C)

		P-value	Significant or not	difference between means (±SEM)	95% confidence interval
ctrl Ex vivo	**0GY**	<0.0001	Yes (***)	23.57 ± 4.379	14.49 to 32.65
0Gy	**1µM Nu7441**	0.0334	Yes (*)	-15.11 ± 6.407	-28.85 to -1.370
0Gy	**5µM Nu7441**	0.0412	Yes (*)	-17.20 ± 7.519	-33.58 to -0.8132
0Gy	**10µM Nu7441**	0.1088	No	-13.85 ± 7.994	-31.26 to 3.570
0GY	**10Gy**	<0.0001	Yes (***)	46.47 ± 6.368	32.81 to 60.13
10Gy	**1µM Nu7441 +10Gy**	0.998	No	-0.006250 ± 2.491	-5.349 to 5.336
10Gy	**5µM Nu7441+ 10Gy**	<0.0001	Yes (***)	18.30 ± 2.645	12.63 to 23.97
10Gy	**10µM Nu7441 + 10Gy**	<0.0001	Yes (***)	24.46 ± 1.841	20.51 to 28.40

Raw statistical data corresponding to figure 5.15 (D)

		P-value	Significant or not	difference between means (±SEM)	95% confidence interval
ctrl Ex vivo	**0GY**	0.0042	Yes	2.062 ± 0.7033	0.6655 to 3.458
0Gy	**1µM Nu7441**	0.5668	No	-0.3148 ± 0.5483	-1.399 to 0.7698
0Gy	**5µM Nu7441**	0.1234	No	-0.9791 ± 0.6307	-2.229 to 0.2705
0Gy	**10µM Nu7441**	0.0063	Yes (**)	-1.624 ± 0.5826	-2.778 to -0.4693
0GY	**10Gy**	0.8619	No	0.08099 ± 0.4649	-0.8375 to 0.9995
10Gy	**1µM Nu7441 +10Gy**	0.0293	Yes (*)	0.9375 ± 0.4263	0.09543 to 1.780
10Gy	**5µM Nu7441+ 10Gy**	<0.0001	Yes (***)	4.438 ± 0.5004	3.449 to 5.426
10Gy	**10µM Nu7441 + 10Gy**	<0.0001	Yes (***)	8.713 ± 0.5801	7.567 to 9.858

Raw statistical data corresponding to figure 5.16 (A)

		P-value	Significant or not	difference between means (±SEM)	95% confidence interval
ctrl Ex vivo	**0GY**	<0.0001	Yes (***)	10.28 ± 1.433	7.304 to 13.25
0Gy	**1µM Nu7441**	0.0193	Yes (*)	-6.333 ± 2.396	-11.47 to -1.195
0Gy	**5µM Nu7441**	0.001	Yes (***)	-9.502 ± 2.199	-14.29 to -4.712
0Gy	**10µM Nu7441**	0.0092	Yes (**)	-8.431 ± 2.619	-14.27 to -2.596
0GY	**10Gy**	<0.0001	Yes (***)	46.29 ± 5.398	34.71 to 57.87
10Gy	**1µM Nu7441 +10Gy**	0.1734	No	10.25 ± 7.120	-5.127 to 25.64
10Gy	**5µM Nu7441+ 10Gy**	0.0004	Yes (***)	26.63 ± 5.806	14.17 to 39.08
10Gy	**10µM Nu7441 + 10Gy**	<0.0001	Yes (***)	35.04 ± 5.746	22.71 to 47.36

Raw statistical data corresponding to figure 5.16 (B)

		P-value	Significant or not	difference between means (±SEM)	95% confidence interval
ctrl Ex vivo	**0GY**	0.0043	Yes (**)	1.281 ± 0.4402	0.4094 to 2.152
0Gy	**1µM Nu7441**	0.0001	Yes (***)	-1.635 ± 0.4136	-2.454 to -0.8171
0Gy	**5µM Nu7441**	0.003	Yes (**)	-2.056 ± 0.6756	-3.397 to -0.7141
0Gy	**10µM Nu7441**	0.002	Yes (**)	-1,916 ± 0,6039	-3.114 to -0.7172
0GY	**10Gy**	0.3974	No	0.3545 ± 0.4177	-0.4706 to 1.180
10Gy	**1µM Nu7441 +10Gy**	0.8827	No	0.06250 ± 0.4229	-0.7727 to 0.8977
10Gy	**5µM Nu7441+ 10Gy**	<0.0001	Yes (***)	3.725 ± 0.4950	2.747 to 4.703
10Gy	**10µM Nu7441 + 10Gy**	<0.0001	Yes (***)	5.225 ± 0.4778	4.281 to 6.169

Raw statistical data corresponding to figure 5.17

		P-value	Significant or not	difference between means (±SEM)	95% confidence interval
ctrl Ex vivo	**0GY**	0.0053	Yes (**)	6.917 ± 2.184	2.329 to 11.50
0Gy	**1µM Nu7441**	0.5496	No	1.769 ± 2.885	-4.419 to 7.956
0Gy	**5µM Nu7441**	0.4073	No	-2.351 ± 2.752	-8.254 to 3.552
0Gy	**10µM Nu7441**	0.9484	No	0.1962 ± 2.977	-6.189 to 6.581
0GY	**10Gy**	0.9467	No	-0.1775 ± 2.609	-5.772 to 5.417
10Gy	**1µM Nu7441 +10Gy**	0.0638	No	5.421 ± 2.655	-0.3628 to 11.20
10Gy	**5µM Nu7441+ 10Gy**	0.1238	No	3.170 ± 1.936	-0.9815 to 7.322
10Gy	**10µM Nu7441 + 10Gy**	0.0416	Yes (*)	3.826 ± 1.706	0.1677 to 7.485
10µM Nu7441 + 10Gy	**0Gy**	0.2537	No	3.649 ± 3.065	-2.925 to 10.22

Raw statistical data corresponding to figure 5.18 (B)

		P-value	Significant or not	difference between means (±SEM)	95% confidence interval
ctrl Ex vivo	**0GY**	0.2928	No	2.525 ± 2.310	-2.429 to 7.479
0Gy	**10Gy**	<0.0001	Yes (***)	47.03 ± 2.665	41.50 to 52.56

Raw statistical data corresponding to figure 5.18 (C)

		P-value	Significant or not	difference between means (±SEM)	95% confidence interval
ctrl Ex vivo	**0GY**	0.808	No	1.104 ± 4.458	-8.458 to 10.67
0Gy	**10Gy**	<0.0001	Yes (***)	80.35 ± 3.132	73.82 to 86.88

Raw statistical data corresponding to figure 5.18 (D)

		P-value	Significant or not	difference between means (±SEM)	95% confidence interval
Ctrl Ex vivo 0Gy	**0GY 10Gy**	0.6207 <0.0001	No Yes (***)	0.3349 ± 0.6750 5.420 ± 0.5382	-1.002 to 1.671 4.358 to 6.482

Raw statistical data corresponding to figure 5.18 (F)

		P-value	Significant or not	difference between means (±SEM)	95% confidence interval
Ctrl Ex vivo	**0GY**	0.252	No	4.717 ± 3.948	-3.751 to 13.18
0Gy	**10Gy**	<0.0001	Yes (***)	63.30 ± 3.835	55.30 to 71.30

Raw statistical data corresponding to figure 5.18 (G)

		P-value	Significant or not	difference between means (±SEM)	95% confidence interval
Ctrl Ex vivo	**0GY**	0.0269	Yes (*)	0.8677 ± 0.3874	0.1007 to 1.635
0Gy	**10Gy**	<0.0001	Yes (***)	5.961 ± 0.4257	5.121 to 6.800

Raw statistical data corresponding to figure 5.20 (A)

		P-value	Significant or not	difference between means (±SEM)	95% confidence interval
0Gy <10	**2h (10Gy) <10**	<0.0001	Yes (***)	-24.35 ± 2.084	-28.73 to -19.97
2h (10Gy) <10	**24h (10Gy) <10**	<0.0001	Yes (***)	21.07 ± 2.415	16.00 to 26.15
0Gy <10	**24h (10Gy <10**	0.0153	Yes (*)	-3.274 ± 1.222	-5.842 to -0.7072
0Gy >10	**2h (10Gy) >10**	<0.0001	Yes (***)	24.35 ± 2.084	19.97 to 28.73
0 Gy >10	**24h (10Gy) >10**	0.0153	Yes (*)	3.274 ± 1.222	0.7072 to 5.842
2h (10Gy) >10	**24 (10Gy) >10**	<0.0001	Yes (***)	-21.07 ± 2.415	-26.15 to -16.00

Raw statistical data corresponding to figure 5.20 (B)

		P-value	Significant or not	difference between means (±SEM)	95% confidence interval
Ctrl <10	**0Gy <10**	0.7788	No	-2.537 ± 8.905	-21.17 to 16.10
0Gy <10	**10Gy <10**	0.0005	Yes (***)	-38.27 ± 9.845	-58.35 to -18.19
Ctrl >10	**0Gy >10**	0.7788	No	2.537 ± 8.905	-16.10 to 21.17
0Gy >10	**10Gy >10**	0.0005	Yea (***)	38.27 ± 9.845	18.19 to 58.35

Raw Statistical data corresponding to figure 5.21 (B)

		P-value	Significant or not	difference between means (±SEM)	95% confidence interval
Ctrl Ex vivo <10	**0Gy 2h <10**	<0.0001	Yes (***)	-2.000 ±2.000	-6.202 to 2.202
0Gy 2h <10	**10Gy 2h <10**	<0.0001	Yes (***)	-20.22 ± 11.64	-44.79 to 4.342
0Gy 24h <10	**10gy 24 <10**	0.2571	No	-15.57 ± 7.613	-31.80 to 0.6571
0GY 2h >10	**10GY 2h >10**	0.0011	Yes (**)	9.111 ± 7.264	-6.214 to 24.44
0Gy 24h >10	**10Gy 24h >10**	0.2571	No	15.57 ± 7.613	-0.6571 to 31.80
0GY 2h >10	**0Gy 24h >10**	0.0865	No	2.166 ± 4,328	-7.009 to 11.34
10GY 2h >10	**10Gy 24h >10**	0.6214	No	8.624 ± 9.573	-11.67 to 28.92